University of
Stavanger

Faculty of Science and Technology

MASTER'S THESIS

Study program/Specialization: Petroleum Geosciences Engineering	Semester 4, 2013/2014 Closed
Writer: Raisya Noor Pertiwi	(Writer's signature)
Faculty supervisor: Arild Buland External supervisor(s):	
Title of thesis: Geophysical Analysis in the Grane Area	
Credits (ECTS): 30	
Keywords: AVO, Colored inversion, Extended Elastic impedance, Lithology and fluid prediction, Multivariate statistical classificiation, Grane field, Petroleum system, Reservoir characterization, Rock physics, Seismic inversion,	Pages: 126 +enclosure: 12 Stavanger, 15 June 2014

Geophysical Analysis in the Grane Area

by

Raisya Noor Pertiwi, BSc

Thesis
Presented to the Faculty of Science and Technology
The University of Stavanger

The University of Stavanger
2013/2014
June 2014

Acknowledgement

This thesis is part of my completion of my greatest journey in life. A life that I have been dreaming of… And it had been amazing. To live in picturesque islands and surrounded by kind people, Stavanger city has given me unlimited opportunities to explore many parts of life. Through this completion, there are numerous people including my family, my friends, colleagues and various institutions that always support me. At the end of my thesis, I would like to express my thanks to all those who contributed in many ways to the success of this study.

First and foremost, I wish to thank my advisor, **Arild Buland**. He has been supportive since the days I began working on this thesis, and been always welcomed for every time I knocked his office doors. The good advices, the constructive criticism, extensive discussions and moral supports have been invaluable on both an academic and personal level.

I take this opportunity to sincerely acknowledge the **Statoil ASA** for providing the facilities and the data for this study. I would also thank the **Petroleum Geosciences Engineering Department of University of Stavanger**, to the academic and technical supports, and its staff.

My special acknowledgements for all those people who are there helping me to find the light, whenever everything seems impossible. To my Mom **Anik Djuraidah**, dad **Sjaiful Bachri**, sister **Anisa**, and brother **Mirza**, thank you for everything.

Stavanger, June 2014
Raisya Noor Pertiwi

Abstract

Geophysical Analysis in the Grane Area

Raisya Noor Pertiwi, MSc
The University of Stavanger, 2013/2014

Supervisor: Arild Buland

Conventional seismic stack are not very efficient to delineate the hydrocarbon bearing interval within the Lower Heimdal sandstones in the Grane area, as the reflectivity of top Lower Heimdal are subtle. This becomes more difficult as the wells are sparse and the sandstones have a complex distribution. This study suggests an improved structural mapping of top reservoir and an improved knowledge of the communication and distributions of hydrocarbon bearing interval. As an approach, this study develops a strategy of interpretation by using different seismic attributes. The seismic attributes are generated with and without involving the seismic inversion process by using near and far partial seismic stack. A cross-disciplinary analysis is also performed to justify the impact of lithology, pore-fluid saturation level, and petrophysical properties of the target interest, in the interpretation of seismic amplitudes with function of offset. This analysis includes well-log analysis, rock physics, AVO forward modeling, and multivariate statistical classification.

The analysis is also extended to quantify the level of sensitivity towards pore-fluid and lithology of different seismic data attributes. Using a right strategy for interpretation, by means of using a right seismic data attribute, one can obtain the information of pore-fluid, or lithology, or both of them; and reduce the probability of false misinterpretation. From all generated seismic reflectivity attributes, the gradient and the EEI reflectivity, provide the most reliable interpretation strategies for highlighting the top of Lower Heimdal sands. In terms of delineating hydrocarbon bearing sandstones, these attribute are also effective as well as the AVO Strength and the resulting impedance attributes given by seismic inversion. Together with the reflectivity attributes, the impedance attributes can provide a competent foundation to discriminate the oil-sandstones signature and to estimate the distribution of oil-sandstones bodies in 3D extent.

Table of Contents

List of Figures

List of Tables

CHAPTER 1.

INTRODUCTION

STUDY FOCUS

The main exploration target in Grane area is the Lower Heimdal sands. With the mounded shaped architecture, the continuity of the unit is hard to predict. The reflectivity of top Lower Heimdal is also subtle in the ordinary seismic. As seismic attribute provides sophisticated process to enhance the sensitivity of the ordinary seismic data towards pore-fluid and lithology, seismic attributes are generated with and without involving the seismic inversion process. In terms of reflectivity domain, the tested seismic attributes include the intercept-gradient, AVO Class-AVO Strength, and EEI reflectivity. While in terms of impedance domain, attribute are generated by using three type inversions, trace integration band-limited, colored inversion, and combination of colored inversion with EEI inversion. Using a right strategy means using the right tools, or using a right seismic data attributes. Using a right attribute will reduce the chance of false misinterpretation. Besides, information that can be achieved from eac attribute is varied. One attributes may help to identify the top of Lower Heimdal, others can help to identify the pore-fluid type, and some can do both. The variation of seismic attributes reliability is accessed carefully to provide readers some good strategic points in interpreting hydrocarbon-bearing unit of Lower Heimdal sandstones.

Well log data provide information about rock properties with function of depth. The rock properties such as lithology, pore-fluid saturation level and petrophysical parameters, has strong impact to diversify the elastic parameters values. As the seismic are correlated to these parameter, it is possible to generate a bridge between them by using well log information. Rock physics will be the first bridge. Rock physics analysis, correlates the elastic parameter including velocity, impedance, and velocity ratio, with geological and petrophysical parameters such as density, porosity, gamma-ray, mineralogical composition, depositional environment, post-depositional process, fluid properties, oil-saturation level, and temperature. In the next step, the level of sensitivity of log data, towards pore-fluid and lithology are accessed by performing the multivariate statistical classification. This analysis is also extended to predict the amplitude variations with offset on seismic data, particularly for the reservoir unit. These integrated understanding will benefit readers to understand of what the real seismics are speaking, what are the limitations, why it has more sensitivity to pore-fluid variation rather than lithology, and so on.

SUBJECTS

CHAPTER 2: GEOLOGICAL BACKGROUND

This chapter mainly provides geological information of the study area, the Grane field. The information covers the geological setting, geological history, structural and stratigraphic information which are useful to understand its petroleum system.

CHAPTER 3: THEORITICAL BACKGROUND

Provide compilation of some important studies that had been carried out by researchers. The studies include the correlation between lithologies and its physical properties, geological condition and elastic parameters. Some good insight of reservoir characterization methodologies that are implemented on this study, Amplitude versus Angle (AVO or AVA), Coloured Inversion (CI), Extended Elastic Impedance (EEI), and Bayesian Seismic AVA Inversion are also covered within this chapter.

CHAPTER 4: ROCK PHYSICS DIAGNOSTICS

1. How do the geological processes correlate to parameters such as velocity, gamma-ray, density and porosity?
2. How the lithological changes were affected by such geological processes?
3. By correlating (1) and (2), what kind of physical properties that best describe the reservoir?

For answering these questions, it is essential to link between rock physics to geological processes such as depositional and compactional trends, also the microstructure properties of rock itself. To support this study, analysis of thin sections, lithology classification as function of elastic parameter and other reservoir properties, such as porosity and density, had been implemented.

CHAPTER 5: SENSITIVITY ANALYSIS AND AVO/AVA FORWARD MODELING

1. Using well data information, what seismic signature that may represent the top reservoir? How it was affected by the pore-fluid content?
2. How reliable is the log-property from a certain well to predict lithology and fluid properties in other well?

Fluid substitution is attained in separate ways from rock physics modeling, and has been accomplished by previous work of Gassmann substitution modeling. The result from

Gassmann fluid substitution is then carried out to perform seismic signature prediction and AVO/AVA analysis. The result given by the AVO/AVA of Gassmann synthetic seismics are then compared with the AVO/AVA results of Monte-Carlo analysis. The Monte-Carlo AVO/AVA analysis is achieved by extracting the probability density functions (pdfs) from log-data, each well respectively. This simulation estimates the character of lithology interfaces within AVO/AVA domain. By using the same pdfs information, discussion is also extended to understand the degree of similarity between wells within the investigated area, and to understand the degree of log-data sensitivity towards lithology and pore-fluid changes.

CHAPTER 6: POST-STACK SEISMIC ANALYSIS

1. With function of interface contrast, where is the location of top reservoir? How thick is the reservoir that contains the hydrocarbons?
2. With function of rock physical property, using the classical AVO/AVA inversion, how thick is the reservoir that contains the hydrocarbons?

Knowledge related to lithology and fluid components over the target area is a key input for better quality in building reservoir models and performing volumetric calculations. AVO/AVA and seismic inversion are proven to be able to predict the lithology and fluid in the reservoir target worldwide. The degree of each attribute's accuracy will later assessed and confirmed with previous geological observations.

CHAPTER 2.

GEOLOGICAL BACKGROUND

2.1 GEOLOGICAL SETTINGS

The Grane oil field is situated in Block 25/11 in the Utsira High, Norwegian sector of the North Sea (Figure 2.1). The field is located at the eastern margin of the Viking Graben on the western flank of Utsira High (Figure 2.2). It contains heavy (190 API), high viscosity, biodegraded and under saturated oil with no initial gas cap. (Mangerud et al., 1999; Iske and Randen, 2005; Roy et al., 2011). The main interest reservoir is Heimdal Formation, turbidite sandstones of Paleocene age. The main exploration play on this geological setting is mainly stratigraphic traps, where the Heimdal Formation is prograding eastwards from the East Shetland Platform, and also appears as an assymetric mounded shaped (Figure 2.3).

The Utsira High is a wide basement high, flanked by Viking Graben to the west and the Stord Basin to the east (Figure 2.1). The present structural configuration was formed under two major phases of extension, the Permo-Triassic and the Middle-Late Jurassic (Justwan and Dahl, 2005). The first extensional intracratonic basin was formed during Rotliegende, from Republic of Poland and northern Germany to the middle parts of Viking Graben (Isaken and Ledje, 2001). Later, marine water invaded the basin forming Zechestein Sea, resulting organic-rich shales of Kupferschiefer Formation. This formation found to be deposited far north in Viking Graben but generally too thin to generate significant amount of hydrocarbon in Utsira High (Isaken and Ledje, 2001).

In Triassic, crustal extension was forming large rotated fault blocks (Isaken and Ledje, 2001). It followed with subsequent rifting and subsidence during the Jurassic Kimmerian tectonic phase, which then resulting the present structure (Isaken and Ledje, 2001; Martinsen, 2005). Erosion of the uplifted rift flank formed during Middle Jurassic were resulting deposition of non-marine sandstones in western flank of Utsira High, such as deltaic complexes of Brent Delta (Isaken and Ledje, 2001; Justwan et al., 2006).

Another following phase of extension occurred during Bajocian to Volgian times (Middle to Upper Jurassic) where mainly affecting the development of Viking Graben (Justwan et al., 2006). As the result, the sea level rise, resulting wide-spread transgression, and Kimmeridgian to Ryazanian organic shales of Draupne Formation were deposited. The organic shales are interfingering with syntectonics sedimentation simultaneously as result of graben scarps in the western margin of South Viking Graben. During Cretaceous, late Kimmerian rifting phase affecting the area (Isaken and Ledje, 2001). The Late Cretaceous is characterized by low subsidences rates with very little sediment being deposited. Onset of rapid subsidence occurred in the Late Cretaceous mostly in Greater Balder Area, while the Utsira High area to the east only received little or no sediment (Justwan et al., 2006).

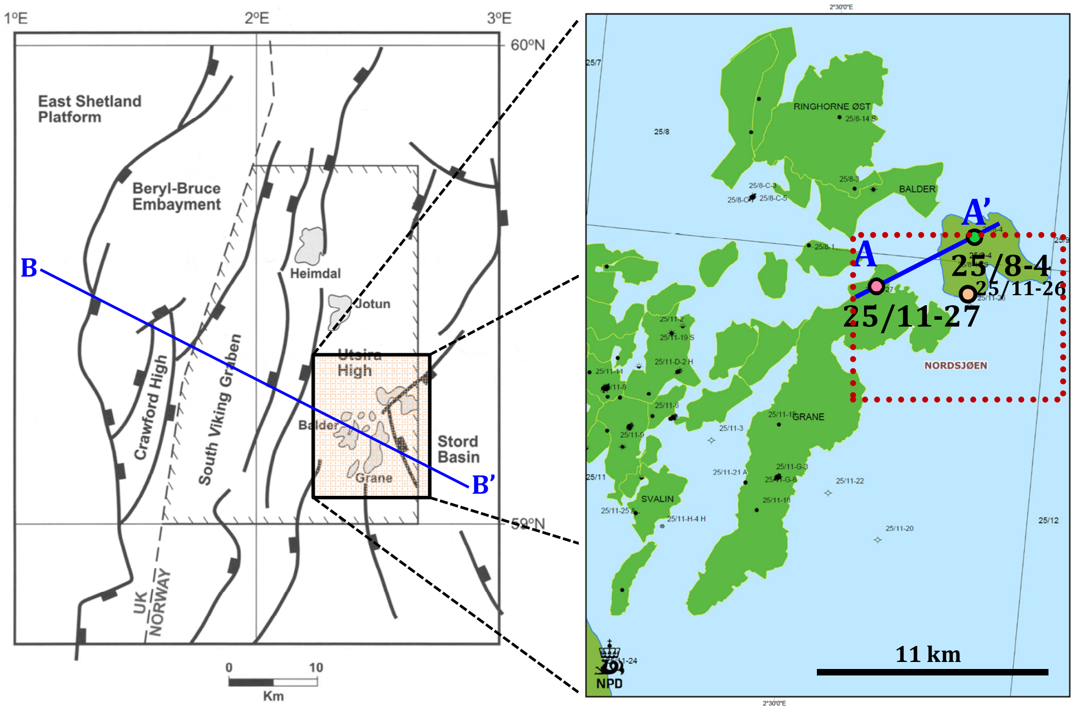

Figure 2.1 (Left) The general structural settings in Utsira High (Mangerud et al., 1999). (Right) The main study area covers the zone within red dotted rectangle.

The Paleocene turbidite systems were controlled by an inherited structural template from Late Jurassic rifting, and by source area size (Figure 2.2). The Grane Field is located above the structural low to the west, but during the deposition, the area lay on a relatively flat basin floor east of the slope to the shallow marine staging area of East Shetland Platform, on which the sand rich system were sourced (Martinsen et al., 2005; Mangerud et al., 1999). In Early Paleogene, association of uplift of the hinterland to the west in the British Volcanic Province and the opening of the North Atlantic were resulting huge quantities of siliclastic sediment to be transported from hinterland source area to the central and northern North Sea. The Paleogene sediment unit provides an excellent reservoir and sealing rocks for hydrocarbon accumulation, and distributed with approximate thickness 70 meters at present and 40 km^2 wide (Martinsen et al., 2005; Avseth, 2000). The uplift of East Shetland Platform during this period was resulting high subsidence rates. Later, during Miocene the subsidence start to reduce and renewal subsidence occurred during Quaternary as it related to the glaciations (Justwan et al., 2006).

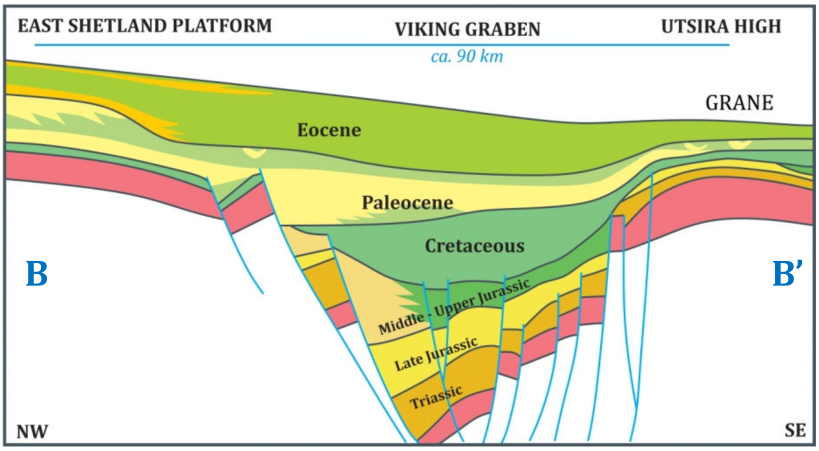

Figure 2.2 Cross section of line section of B-B' in Figure 2.1 (modified from Wild, J., and Briedis, N., 2010).

2.2 STRATIGRAPHY AND FACIES ASSOCIATIONS

Reservoir characterization relies on the information gained from the seismic data. To improve the consistencies of interpretation of the subsurface mode, the petrophysical data, well markers and formation features has to be immersed within the interpretation process. For proper identification of the reservoir, a 3D seismic and three-wells data are given. The 3D seismic covers the area within the red-dotted rectangle (Figure 2.1). The well comprises of F-Well (25-11/27), D-Well (25-8/4), and Nanna-Well (25/11-26). The first two wells, the F-Well and the D-Well are considered to be the main wells that provide petrophysical information of the reservoir, as they both penetrates the targeted reservoir sands. The Nana-Well, in contrary, does not emerge any reservoir sands. The usage of Nana-Well is to measure the reliability of interpretation by using the extracted seismic attributes.

The F-Well and the D-Well were set to test the hydrocabon potential of Palaeocene sands corresponds to findings of seismic mounded structure within the prospect area (Figure 2.3). The interval of target unit comprises of Paleogene sediment, Balder Formation, Sele Formation, Lista Formation, Våle Formation and Shetland Group, where the main target is the Heimdal Formation (Figure 2.5). The Paleogene sediment characterizes as a high degree of soft sediment deformation, which may explain as high sedimentation, but also rapid sedimentation of sands onto unstable, highly watercharged, smectite-rich muds. The source of smectite is thought to be result of ash deposition from volcanism in the British Volcanic Province throughout Late Paleocene and Early Eocene (Martinsen et al., 2005).

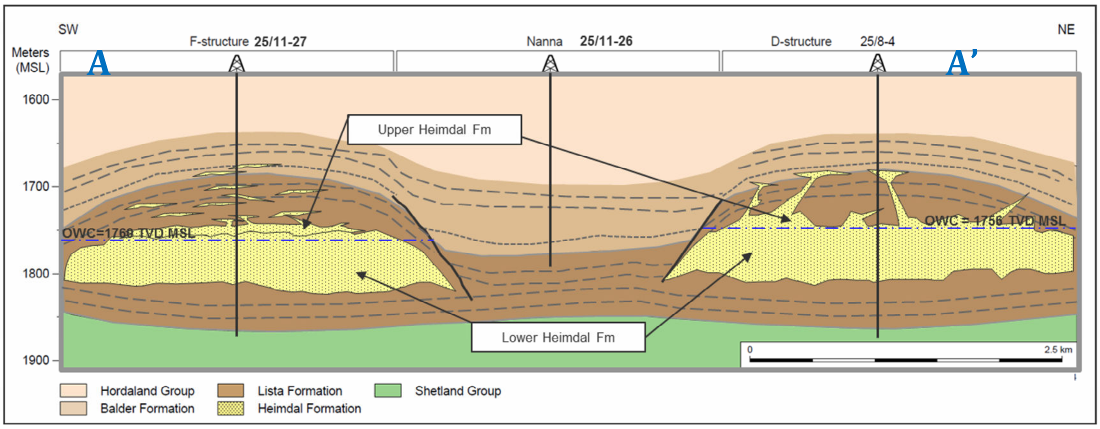

Figure 2.3 Cross section of line section of A-A' in Figure 2.1 (Statoil Internal, 2013).

Hordaland Formation

Within this group, there are no sands found in the D-Well and F-Well. This group mainly consists of claystone with limestone stringers (Statoil Internal, 2013). The deposition occurred under bathyal marine conditions with partially restricted circulation (Statoil Internal, 1993).

Balder Formation

The Balder Formation found in the F- and D-Well is predominantly claystones with minor sandstones interbedded, and a local tuff-rich unit. The sediments are interpreted to be deposited under sublitoral marine environment of restricted circulation with contemporaneous volcanic activity during Early Eocene to Late Paleocene (Statoil Internal, 1993). The thickness of this formation is 20 meters thicker (TVD) in the D-well (Figure 2.4, Table 1). At the F-well, the Balder formation encountered at 30 meters deeper than at the D-Well. In both wells, the tuff-rich unit appears as low gamma-ray. There are no obvious changes in velocity and density in the top of tuff unit; however in the base one can observe that the velocity and density drop as the lithology changes towards shale unit.

Sele Formation

A very clay-rich shale and intercalation of tuffaceous with carbonate units can be present. Turbidite sands can also occur within the Sele Formation, and these are referred to as the Hermod Formation sands (Mangerud et al., 1999; Avseth, 2000). However, this formation is not encountered at both wells (Figure 2.4).

Lista and Heimdal Formation

The Lista formation is mainly shaly. The main reservoir, the Heimdal formation is encased in the smectite-rich Lista formation claystones. The Lista and Heimdal formation are interpreted to be deposited under bathyal marine environment with high energy of clastic input resulted from gravity flow during Late Paleocene, possibly as channel fill sands for Heimdal formation (Statoil Internal, 1993). The top of reservoir, the Heimdal Formation, is marked with the value drop of Vsh (Figure 2.4). This drop is considered to be the transition of clay-rich unit to the clay-free unit. The Heimdal Formation in the D-Well has a total gross thickness of 50 meters is mainly water wet, with only 1.5 meters oil column up to 1781.5 meter (MD). The Heimdal Formation in the F-Well is divided into two different sub-formations, Upper and Lower Heimdal formation. The Upper Heimdal formation is consisted of four sand layers with varying thickness between 2-5 meters, and intercalated within claystones. The Lower Heimdal formation unit appears to be a massive unit with net thickness of 38 meters and 17 meters main oil-bearing up to 1785 meter (MD). With an average porosity of 35% and permeability around 5-10 Darcy (Statoil Internal, 1993; Statoil Internal, 2013), the Lower Heimdal unit favors to be an excellent reservoir.

Våle Formation

The Våle formation consists of claystones which correspond to sublitoral to upper bathyal environment deposition during Early Paleocene, Early Thanetian (Statoil Internal, 1993). This formation is distinguished from the formation above and below as drop in velocity and high gamma-ray values (Figure 2.4). The unit is relatively thin and argillaceous in the Grane area, due to the pinchout of the deep-sea fan sandstones further west (Mangerud et al., 1999; Avseth, 2000).

Shetland Group

The Shetland Group consists of the Ekofisk Formation, Tor Formation, and Hod Formation from the youngest to oldest. This group is represented as Early Paleocene (Danian) to Early Santonian deposits that consist of limestones under open marine to outer sublittoral shelf environment (Statoil Internal, 1993). The base of Shetland formation represents the base of the target of inspected interval within this study.

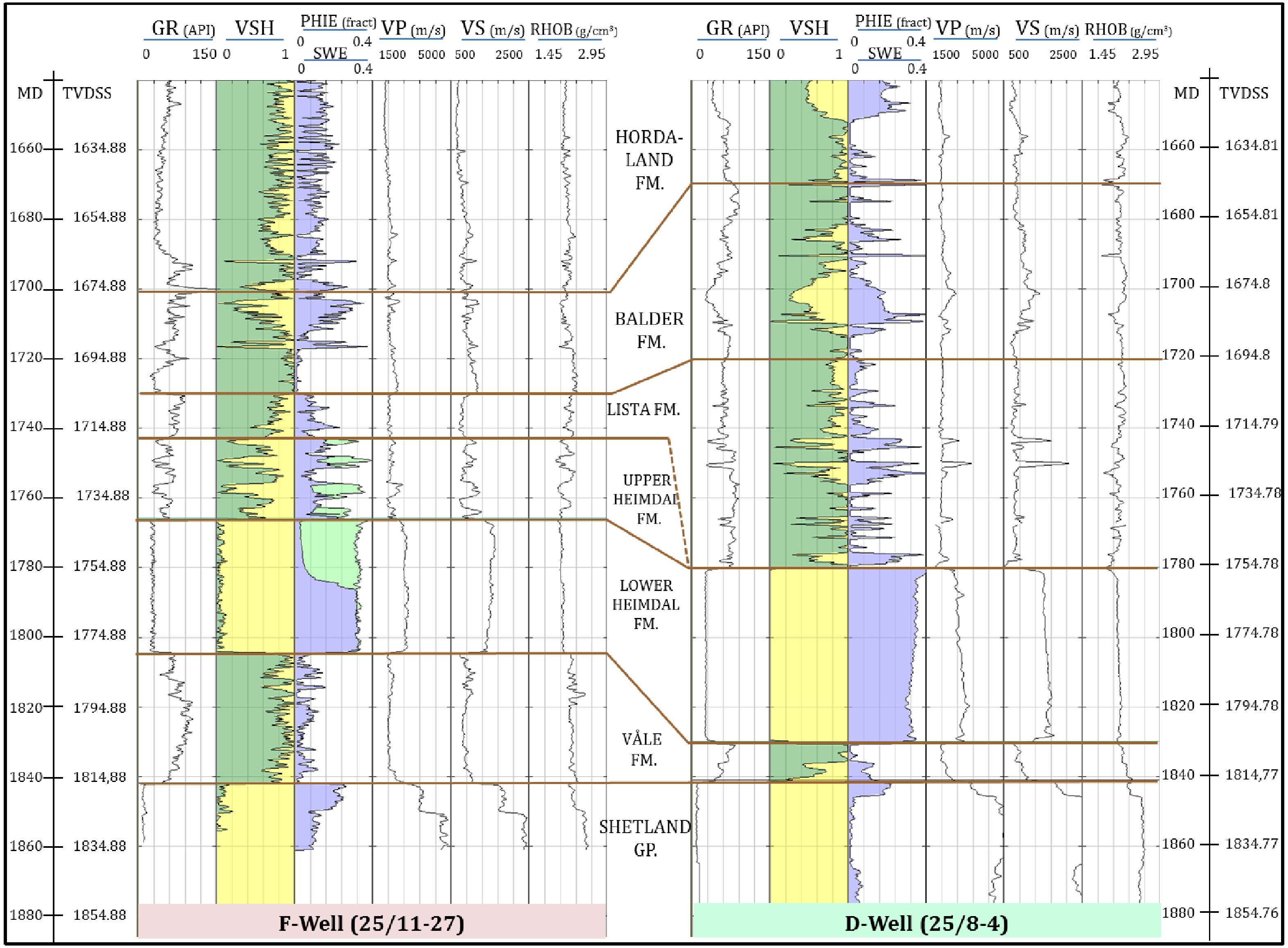

Figure 2.4 Main well log information for the F-Well and D-Well.

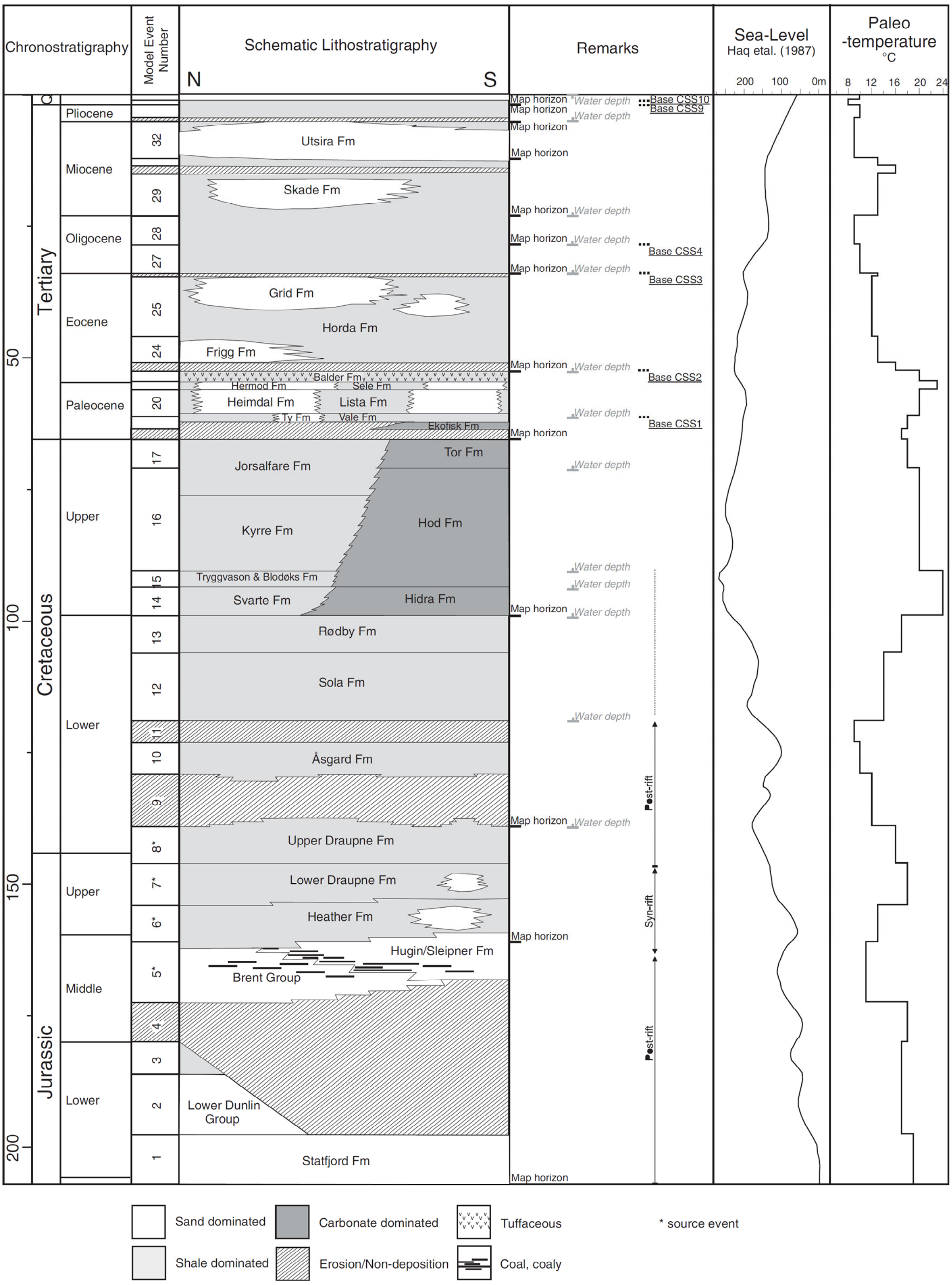

Figure 2.5 Generalized lithostratigraphy of Grane area. The interval target unit comprises of Palaegene sediments (Justwan et al., 2006)

Formation	25/11-27		25/8-4	
	Z (TVDSS m)	Thickness (m)	Z (TVDSS m)	Thickness (m)
Hordaland Gp	-957.96	-717.91	-859.97	-784.84
Balder Fm	-1675.87	-29	-1644.81	-49.99
Lista Fm	-1704.87	-13	-1694.8	-59.98
Upper Heimdal Fm	-1717.87	-23		
Lower Heimdal Fm	-1740.87	-38.5	-1754.78	-49.99
Våle Fm	-1779.37	-37.5	-1804.77	-11
Shetland Gp	-1816.87		-1815.77	

Table 1. Formations top and thickness based on log information of F- and D-Well in Figure 2.4.

2.3 PETROLEUM SYSTEMS

The primary source rocks in this area are Jurassic organic-rich shales, oil prone Kimmeridgian to Volgian–Ryazanian Draupne Formation (Isaken and Ledje, 2001; Justwan and Dahl, 2005; Pedersen et al., 2006). The Oxfordian Heather Formation forms a secondary source which has poor to fair potential for oil. Organic facies in the Draupne Formation are varied, but this variation provide as secondary reasons for oil and gas prone condition. Thermal maturity of source is seen as the primary control in determining oil or gas prone (Isaken and Ledje, 2001). The marine transgressive marine shales of the Draupne formation are interpreted to have accumulated under anoxic bottom-water conditions that preserve the oil-prone condition, kerogen type III (Isaken and Ledje, 2001, Justwan et al., 2006). The Draupne Formation was subdivided into a lower and upper part. The Lower Draupne Formation deposited during rifting while the Upper Draupne formation was deposited after (Justwan and Dahl, 2005). As the increasing marine influence, the contribution of terrestrial influence decreases from the Lower to Upper Draupne formation. Thermal maturity and depth relation analysis suggest that peak oil generation of the Draupne shales occurs within depths of 3400-4400 meters below sea-floor (Isaken and Ledje, 2001; Justwan et al., 2006).

The main clastic reservoir is the Palaeocene sandstones, Heimdal Formation. It has been proven that this unit contains hydrocarbon in some areas. The migration from the Jurassic source rocks into the Palaeocene reservoir includes margin pathway within Jurassic carriers and vertical leakage into the Palaeocene at fault zones of the western margins of the Utsira High (Figure 2.2), followed with the migration within the Tertiary system (Isaken and Ledje, 2001; Justwan et al., 2006). The main top seal of the

Palaeocene reservoir system is the overlying the Eocene shales. The depositional geometry, the reservoir architectures, the deformation and the sand remobilization process favor the Grane area to be a good prospect for hydrocarbon exploration.

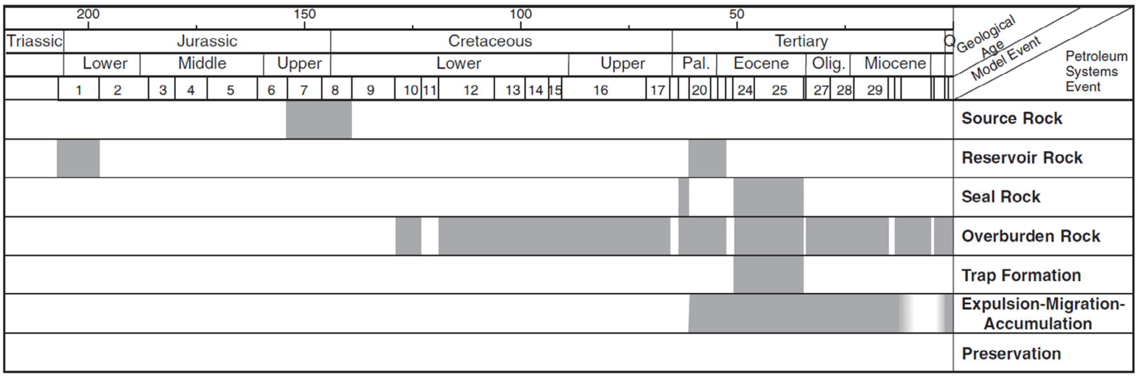

Table 2. Petroleum system event's chart (Justwan et al., 2006).

Justwan et al. (2006) confirmed that the source rock located in the main graben is the only location that enters the hydrocarbon generation window, while the source rock on Utsira High remains immature. The onset of hydrocarbon generation for Lower Draupne formation commenced in Late Cretaceous in the deepest source rock location such as South Viking Graben, while predominantly the hydrocarbon generation was mostly in Palaeocene to Oligocene. Hydrocarbon generation for the Upper Draupne formation was started in the early Palaeocene while the major part mostly Eocene to Middle Miocene. The commencement of hydrocarbon generation is related to the rapid subsidence rate during Paleogene. The Grane area is considered to be within the most oil prone area where oil expelled with the major contribution from the Lower Draupne Formation. This source also charges the big oil fields nearby, such as Balder and Ringhorne. The petroleum system for the Grane area is summarized within Table 2.

CHAPTER 3.

THEORITICAL BACKGROUND

3.1 ROCK PHYSICS TRENDS

In siliclastic sedimentary basin, sandstones and claystones, respond differently in compaction trend as they controlled by different process. The compaction of both sandstones and claystones undergone mechanically as function of effective stress or burial depth until chemical compaction takes over with the function of temperature and time (Bjørlykke, 2010b). The initial mineralogical and textural composition (provenance), the depositional environment, and diagenetic process near the surface also during burial, play as important roles to determine the properties of sandstones and claystone (Bjørlykke, 2010b; Bjørlykke and Jahren 2010).

Increasing effective stress from overburden in mechanical compaction process are resulting the different degree of compressibility as the reduction of bulk volume is equal to porosity loss (Bjørlykke, 2010b). Compaction is a function resulted by increasing effective stresses during burial and mechanical stability. In chemical compaction, the reactions involved include the cementation, dissolution of unstable mineral, precipitation of mineral that are more stable with respect to the composition of pore-water and temperature (Bjorlykke, 2010b). The different physical properties of rocks affected by compaction processes determine porosity, density, and permeability of sediments, and physical and elastic properties (Bjørlykke et al., 2010).

3.1.1 COMPACTIONAL TRENDS

Clay and Claystones

Under mechanical compaction, fine-grain sediments like claystone will have overburden stress to be distributed over a large number grain contacts, therefore the stress per grain contact will be lower than sandstones (Bjørlykke et al., 2010). The most common clay minerals are smectite, illite, chlorite and kaolinite. Smectite is very sensitive to the chemical composition of pore-water. Increasing salt saturation will increase their compressive and shear strength (Bjorlykke, 2010b).

Kaolinite is derived from humid climate weathering, while chlorite mostly derived from slow weathering of metamorphic rock in cold climates (Bjorlykke, 2010a). Volcanic ash that is consisting unstable volcanic mineral assemblages may alter to smectite (Bjorlykke, 2010a; Avseth et al., 2008). Since smectite is subjected to be finer than kaolinite, kaolinite as the coarsest clay mineral is deposited in the most proximal areas while smectite is deposited further out into distal area (Bjorlykke, 2010a).

At 70-80^{o}C, smectite becomes unstable and dissolved, followed with precipitation of illite. In this process, silica will also form and precipitates as quartz cement (Avseth et al., 2008; Bjorlykke, 2010b). Smectite is only stable when the concentration of silica is high. Therefore, the process of illitization will proceed in balance with quartz cementation, with function of temperature. Chlorite however, is also produced within the illitization process if the smectite has iron- and magnesium-rich content (Dowey, 2012; Bjorlykke, 2010b).

$$Smectite + K^{+} = Illite + Quartz$$

Biogenic debris such as carbonate and silica are critical to diagenesis. In volcanic sediment, biogenic debris such as amorphous silica can be also the source for precipitation of quartz cement (Bjørlykke and Jahren, 2010; Avseth et al., 2008). The precipitation of this type of silica, can be conducted even at low temperature, 60-80^{o}C, and form microcrystalline quartz cement.

In the study area, claystone are mainly associated with volcanic activity present as abundant smectite layers meaning authigenic clays, and other biogenic silica produced by organism such as radiolarians and diatoms act as the source of quartz cementation (Bjørlykke and Jahren, 2010). These two clay minerals will leads to poor porosity preservation during mechanical compaction. However, the precipitation of amorphous silica will coat the clastic grains in counter way, prevent the precipitation of later quartz cement, and preserve the high porosity (Bjørlykke and Jahren, 2010).

Clay minerals are platy shaped, with large surface area (Bjørlykke, 2010a). Relatively small amounts of mineral precipitation and quartz cementation formation cause a significant increase in stiffness and velocity. As quartz cement, a relative moderate amount of carbonate cement also resulting high velocity at shallow depth as the increase of stiffness. Carbonate cements are mostly formed as product of dissolution and reprecipitation of biogenic carbonate, and leaching of plagioclase may yield Ca^{2+} (Bjørlykke and Jahren, 2010).

Such variation of clay mineral, and parameters like anisotropy related to the grain orientation will affect the velocity. Higher degree of burial correspond to higher degree of parallel orientation of silicate mineral sheet, ie. mica, illite and chlorite (Bjørlykke, 2010b; Ruud et al., 2003). Compare to sandstones, the platy clay fabric will more prone to compaction than the assemblage of spherical grain in sands, resulting higher porosity loss than sands (Avseth et al., 2003).

Sand and Sandstones

The sandstone is mechanically compacted as function of effective stress or burial depth by grain reorientation. Sand grains of quartz and feldspar tend to be blocky and irregular than spherical (Bjørlykke et al., 2010). Contact area thus very small, resulting higher contact stress than smaller grain (Figure 3.1). When the grain sand is coarser, the effective stresses may cause high grain-to-grain contact stresses which lead the grains to be fractured (Bjørlykke et al., 2010). Given by Bjørlykke et al. (2010), in a finer sand, the contact of more spherical grain will compact much less at the same stress level, preserving the porosity at 30-35% at ~2 km depth; while in coarser grain, the porosity reduction occurred in higher rate (Figure 3.2). The less porous and the more the rock become stiffen; the number and area of grain contact will increase, as well as velocity.

Quartz cementation mostly occurs at 70-80^{0}C (Bjørlykke and Jahren, 2010; Avseth 2010; Avseth et al., 2008; Dræge, 2011). If the temperature is higher than this interval, the cementation process will proceed but at a slower rate (Bjørlykke and Jahren, 2010). It stabilizes the grain framework; strengthen the rock faster than the burial stress. With only 2-4% quartz cement by-product will prevent further mechanical compaction or rearrangement of grains (Bjørlykke and Jahren, 2010). The amount of quartz cement is function of grain surfaces available for quartz precipitation, presence of grain coatings, subsidence rate and the time-temperature function (Bjørlykke and Jahren, 2010). As the temperature play as major role, the effective stress is far less dominant due to the over-consolidation. Within this interval, the increasing velocity coincides with the loss of porosity is due to cementation process (Bjørlykke, 2010b).

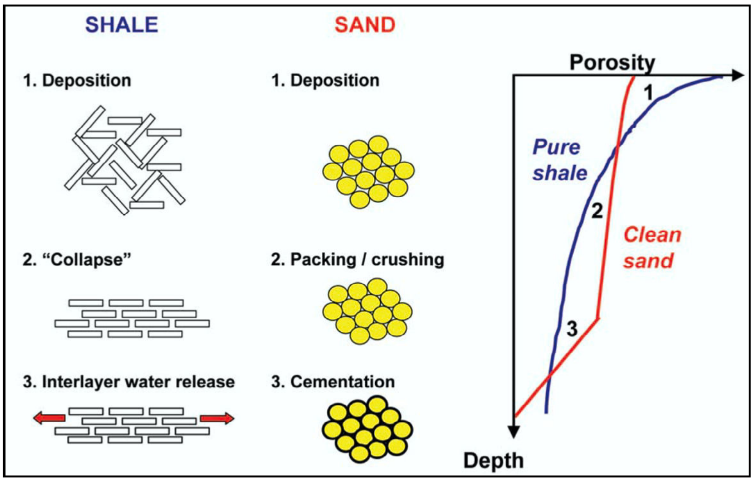

Figure 3.1 Schematic illustration of porosity-depth trends for sands and shales as function of composition, texture, pore fluids, temperature, and pressure gradients (Avseth et al., 2003).

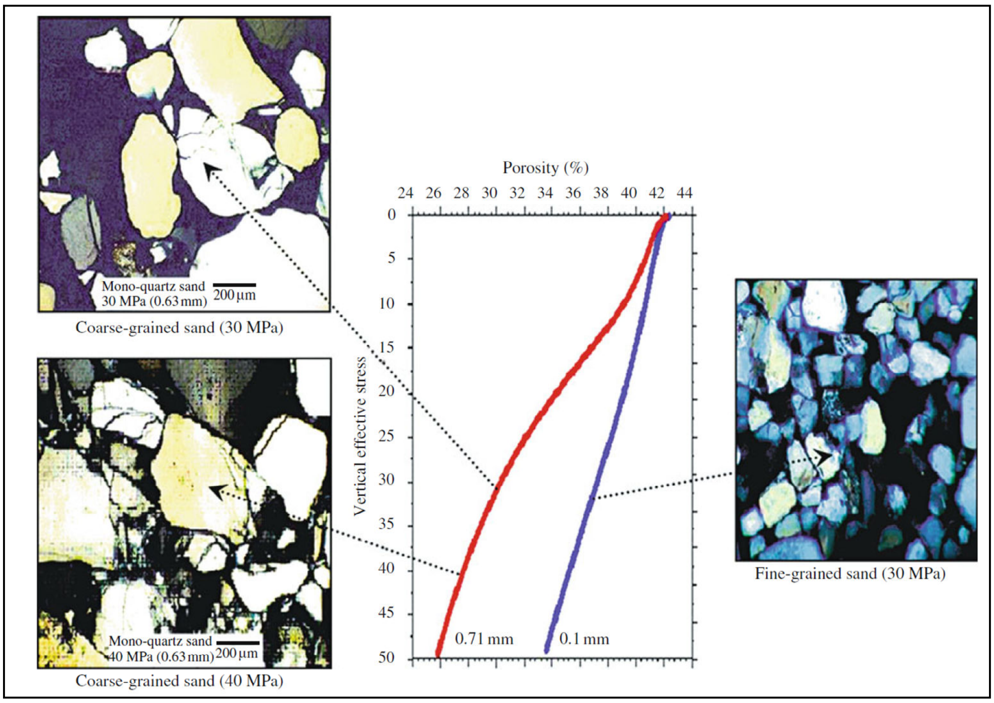

Figure 3.2 Bjørlykke et al. (2010). Experimental compaction of fine-grained and coarse-grained sand.Well sorted fine-grained sand (blue) is less compressible than coarse-grained sand (red).

Porosity preservation may introduced by chlorite and amorphous silica coating. As mentioned, chlorites origin varies from detrital chlorite as a product of metamorphic weathering to diagenic chlorite of iron- and magnesium-rich content smectite (Dowey, 2012; Bjorlykke, 2010b). When chemical compaction starts, illite and chlorite formed, the porosity will be preserved as chlorite prevents the quartz overgrowth and cementation (Bjørlykke and Jahren, 2010). If the grain is oil-wet, quartz cannot precipitate on the grain surfaces since oil act as very effective coatings (Bjørlykke and Jahren 2010; Avseth, 2008).

3.1.2 DEPOSITIONAL TRENDS

The stiffness of sand-shale mixture is determined by the load bearing grains (Figure 3.3). If clay content is less than the sand porosity, clay particles assumed to be located within the pore space of load-bearing sands. The presence of the clay thus stiffens the pore-filling material without affecting the frame properties of sand (Avseth, 2010). In grain supported sediments, the increasing clay will decrease the porosity, increase the stiffness, and increase velocity as the increasing bulk modulus of pore-filling mineral (fluid and clay). The pore-filling clay would not significantly affect the shear modulus of rock, as in fluid case. As seen in Figure 3.4, the clay content increase up to a point called critical clay content (Marion, 1990; Yin, 1992; Dvorkin and Nur, 2002; Avseth, 2010). After this point, additional clay will exceeds the sand porosity, causing the grain to become separated, called clay-supported sediments (Marion, 1990; Yin, 1992; Dvorkin and Nur, 2002; Avseth, 2010). In this system, porosity increases with increasing clay content, and velocity decreases.

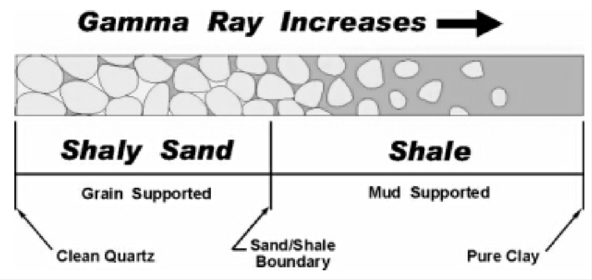

Figure 3.3 Classification of shaly-sands and shale with function of gamma ray (Heslop and Heslop, 2003).

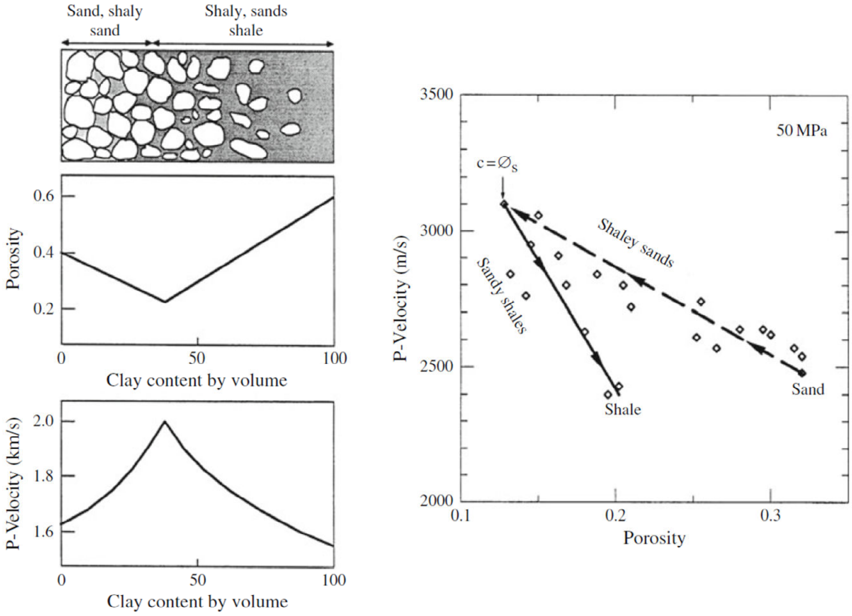

Figure 3.4 Left: The Yin-Marion topological model of porosity and P-wave velocity versus clay content for shaly sands and sandy shales. Right: Model of P-wave velocity versus porosity for unconsolidated sands and shales (Marion, 1990; Yin, 1992; Avseth, 2010).

Shale volume indicator is mostly inherited from gamma ray log. However, in shaly sands, the level of gamma radiation is generally a function of clay volume only (Heslop and Heslop, 2003). The log does not account the volume of silts or other inclusion within the shales except clay. Given by this condition, therefore it is assumed that clay fraction will be linear to the value of gamma ray log, ie. Gamma ray value of 100 is equal to 20-30% of clay. This condition is assumed based on the experiment results within this project by collaborating results in Dvorkin and Nur (2002), Marion (1990) and Yin (1992).

There are two forms of shales exist in shaly sands, laminated and structural shales (Heslop and Heslop, 2003). In structural shales, shales are grain within the sand matrix, and act to support matrix. Laminated shale-shale appears to be shaly-sand on logs while the structural shales will appear much like sand except on the gamma ray log.

3.2 ROCK PHYSICS MODELS

In most of rock physics model, it is important to understand the concept of critical porosity. Critical porosity separates the consolidated-rock domain, stages where porosities are less than critical porosity, from the suspension domain, stages where porosities are greater than porosity (Nur et al., 1998; Dvorkin and Nur, 2002). At suspension domain, the grains are not in contact anymore and grains are supported by fluid (Figure 3.5). Therefore, at this stage, the stiffness of sediment is determined by pore fluid (Dvorkin and Nur, 2002). In consolidated domain, framework is supported by quartz grain contact, and function of stiffness is determined mainly by framework. Later on, diagenetic process let the grains to be compacted and cemented, and porosity will decrease towards zero. Critical porosity of sands is about 36-40% (Nur et al., 1998). In shales, due to the inherent porosity clay minerals will let shale to have higher critical porosity than sand.

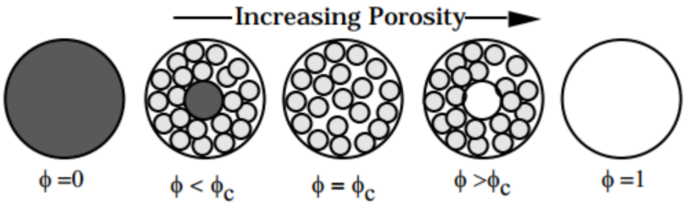

Figure 3.5 The arrangements of sphere pack, solid, and void. (Dvorkin and Nur, 2002).

The weak suspension state at critical porosity refer to the initial condition of packing or initial depositional of sediments and onset of diagenesis (Japsen et al., 2007). Sediment type, grain sorting and the angularity at deposition control the critical porosity (Japsen et al., 2007).

Rock physics analysis is important to calibrate the observation between geological processes to parameters such as velocity and porosity. Geological process such as depositional and compactional trends, also the microstructure properties of rock will infer a different characteristic in these domains. Through rock physics models, one can diagnose the degree of sorting and cement volume as function of porosity and corresponding elastic modulus (Avseth, 2010). Without a proper understanding of rock microstructure may lead to seismic misinterpretation, such as indication pore-fluid changes. For high porosity sands, there are three common theoretical models of rock models representing rock microstructures (Figure 3.6):

1. Uncemented or Friable Model

   The uncemented sand assumes that porosity reduces from the critical porosity or initial sand-pack value due to the deposition of the solid matter or cement away from the grain contacts or non-contact (Avseth et al., 2000). This model is appropriate for describing sands where contact cement deposition was inhibited by organic matter deposited on the grain surface (Dvorkin and Nur, 2002). The model may correspond to depositional trend where the process of porosity reduction would refer to deteriorating grain sorting (Avseth et al., 2000; Dvorkin and Nur, 2002).

2. Contact Cements Model

   The contact cement model assumes that porosity reduce from the initial porosity of a sand pack due to the uniform deposition of cement layers on the surface of the grains (Dvorkin and Nur, 1996; Dvorkin and Nur, 2002; Avseth, 2000). The model corresponds to diagenetic trend, where decreasing porosity means increasing burial intensity. During the burial of sandstones, cementation by diagenetic quartz, calcite or clay results in sitffenning the sands by reinforcing the grain contacts (Dvorkin and Nur, 2002). With reducing porosity from initial sand pack thus the sand stiffens and resulting the effective moduli to increase.

3. Constant Cement Model

   The constant cement assumes that sands of varying porosity all have the same amount of contact cement (Avseth et al., 2000; Avseth, 2000). The model also assumes that physical variation of non-contact pore-filling material within sands relates to porosity value, for example deteriorating sorting. The initial sand porosity reduces from critical porosity due to the contact cement deposition. The situation is followed with the diagenetic process to stop at some high porosity then the porosity reduces by following the constant cement model (Avseth et al., 2000; Avseth, 2000). This porosity is where the porosity reduces due to the deposition of solid matter away from grains contact, as in the friable sand model. Mathematically, the high-porosity end number or critical porosity that is given by φ_c in friable sand model is analogue, but not identical, with the φ_b that is the high-porosity end number at a certain point where the cementation starts (Avseth et al., 2000; Avseth, 2000).

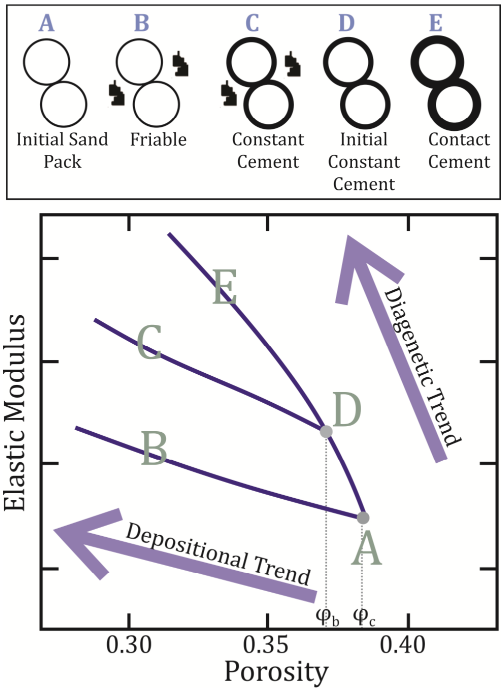

Figure 3.6 Rock physics models link rock microstructure to elastic properties (modified Avseth, 2010).

Rock physics models called Rock Physics Template (RPT) introduced by Ødegaard and Avseth (2003) to explain the relationship between elastic properties and reservoir properties such as lithology, mineralogy, water depth, burial depth, pressure and temperature gradients, diagenesis, and fluid properties (Figure 3.7). The different microstructure of sands, such as the initial cement that lead into decreasing porosity will reduce the fluid sensitivity of sandstones, (Avseth, 2010). The common form of this template is represented as cross-plot between P-impedance and Vp/Vs ratio (Ødegaard and Avseth, 2003).

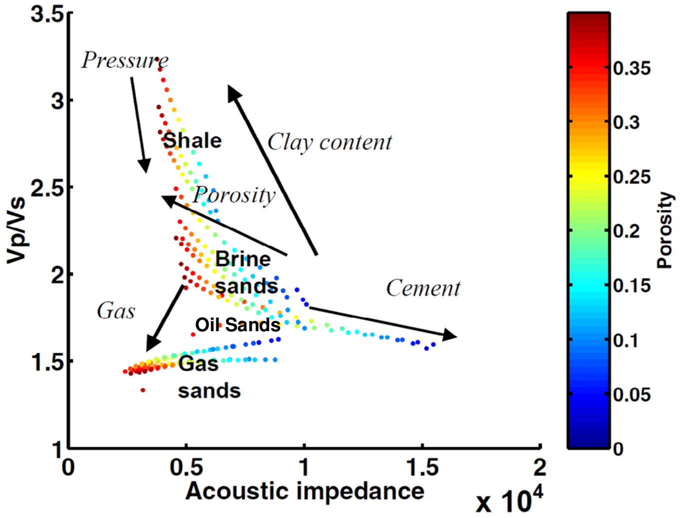

Figure 3.7 Geological trends in the cross-plot domain of Vp/Vs ratio vs. acoustic impedance. Arrows indicate increase in different geological parameters (modified Ødegaard and Avseth, 2003)

3.3 AVO/AVA

The seismic amplitudes represent contrast of the elastic properties of layers. AVO can be used to derive direct hydrocarbon indicators with function of impedance contrast. Classification of AVO responses is based on position of the reflection of interest on an Intercept (A) and Gradient (B) cross-plot. Intercept is a normal incidence reflection coefficient. Gradient value characterizes the change of the reflection up to intermediate angles. As a function of the angle of incidences, the reflection coefficient may changes relative to the normal interface (Ostrander, 1984). A decrease in Poisson's ratio or equivalently velocity (ratio) for the underlying medium causes a decrease in reflection coefficient at the larger angle angles of incidences. In this terms gradient will be negative (Ostrander, 1984, Castagna et al., 1998).

To maintain the offset dependent amplitude changes with offset, instead of full stack, one can produce partial stacks such as near and far stacks (Buland, 2013). Using these attributes, intercept and gradient of seismic cubes can be yielded by simple calculations. Intercept cubes will be similar to the near stack data, while the gradient is the product of subtraction between far angle stack and near angle stack.

Using the AVO cross-plot, the top of hydrocarbon sand reflection will plot below the background trend and the bottom of the hydrocarbon sand reflections will be plot above the trend (Castagna and Swan, 1997; Buland 2013). The top of hydrocarbon-bearing sandstones can be represented as five different classes, Class I, Class IIp, Class II, Class III and Class IV (Figure 3.8 and Figure 3.9). Deviation from the background trend may be indicative for hydrocarbon-bearing zones.

The AVO Class I belongs to the zones of A>0 and B<0, while AVO Class IIp and Class II belongs to zones of A~0 and B<0 (Figure 3.8). The AVO Class I refers to the high impedance contrast of sandstones with overlying unit, while Class II and Class IIp refer to the low impedance contrast of sandstones with overlying unit. In Class I and Class II, the amplitude decrease with increasing angle without changing the polarity of reflection. Strong gradient values of Class II are possible, and the reflection will change in polarity at small or moderate offsets. This AVO type is referred to Class IIp.

The AVO Class III and Class IV belong to sandstones with lower impedances value than overlying unit. The AVO Class III, belongs to zones of A<0 and B<0. The reflections are negative for all offset, and often shows as strong negative on full stack data. The AVO Class IV belongs to zones of A<0 and B>0. This anomalous behavior represents porous sand materials overlain by a high-velocity unit, such as hard shale (Castagna et al., 1998).

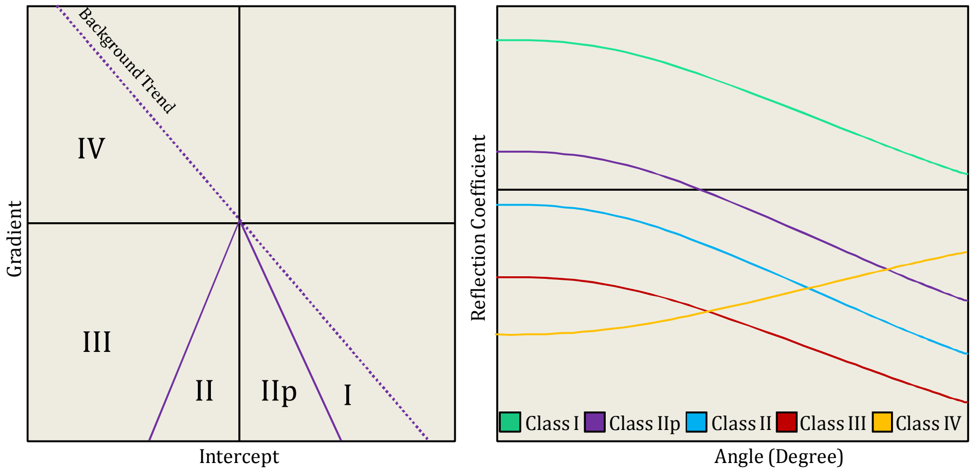

Figure 3.8 (Left)AVO Classess in intercept-gradient crossplots. (Right) Reflection coefficients as a function of reflection angle or different AVO Classes.

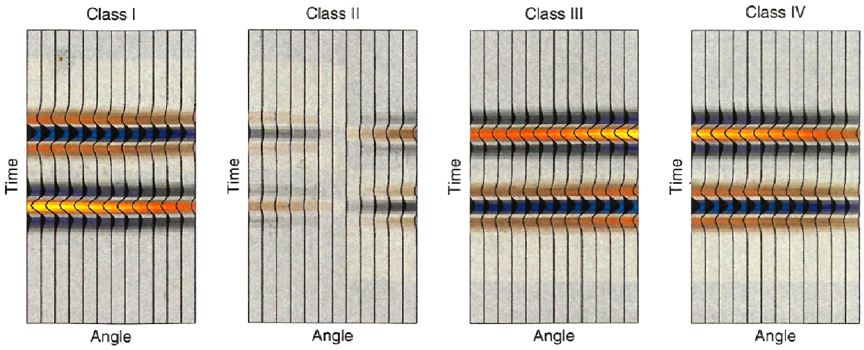

Figure 3.9 Simulated seismic signatures for each AVO Class (Buland, 2013)

3.4 SEISMIC INVERSION FOR LITHOLOGY AND FLUID PREDICTION

Seismic data is an interface property that reflects the contrast of acoustic impedances (Brown, 2011).It is a close approximation to the convolution of a wavelet with reflection-coefficient series. Seismic inversion is a sophisticated process to transform the reflectivity of seismic data to acoustic impedance variations. The impedance provides an ease of interpretation as it is directly correlated to geological or petrophysical terms, ie. the density and velocity of rocks. Inversion will attempt to remove the effect of wavelet in order to derive the layer impedance. Therefore, it has to be assumed in prior to inversion process that seismic data are free from coherent noise (Bacon et al., 2003). There are several practical inversion workflows. In this study, two different deterministic inversions are introduced, the trace integration or band-limited inversion, coloured inversion, and combination of coloured inversion with EEI inversion. In achieving the final estimated impedance volumes, interpretive low frequency is not immersed within the inversion workflow.

Coloured inversion and EEI are efficient to investigate relationship between elastic impedance and target reservoir parameter which play important role in defining lithology and fluid class (LFC). Colored inversion converts the seismic data to relative acoustic impedance (RAI) and gradient impedance (GI) data set, which then combined within EEI process thus optimum correlation for reservoir characterization is achieved. Implementation of EEI can be extended to generate an attributes by using near and far angle stacks. The resulting attributes could help delineating hydrocarbons as function of reflectivity, not impedance.

Band-Limited Trace Integration

The trace integration inversion is limited to the seismic bandwith as it is only using seismic trace as the sole input (Bacon et al., 2003; Brown, 2011). This inversion assumes that the seismic wavelet is zero-phase (Waters, 1978; Bacon et al., 2003). The inversion process can be analogue to reflectivity trace in the Fourier domain which is resulted from the summation of a number of sine waves from different frequencies and phase (Bacon et al., 2003).

$$\int A(\omega)\,\exp\ [i\omega t] = \frac{A(\omega)}{i\omega}\,\exp\ [i\omega t] \tag{1}$$

The integration of an individual sine waves component of frequency ω is resulting sine waves with phase shifted by -90 degree and amplitude multiplied by $1/\omega$. In inversion case, the trace integration shifts each seismic trace by phase of -90 degree, and high-cut filter the entire seismic bandwith as the case of amplitude multiplication of 1/ ω (Bacon et al., 2003). The filtering process usually involves Butterworth filter at 6 dB/octave. Such dependent scaling process is resulting low frequency enhancement within the derived band-limited impedances (Buland, 2013).

Colored inversion and extended elastic impedance (CI and EEI)

Seismic colored inversion is designed to generate two basic attribute volume, relative acoustic-impedance (RAI) and gradient impedance (GI). As function of impedances, both of attributes is further combined within EEI process to derive the best parameter to represent the lithology and fluid changes, respectively.

Seismic colored inversion is designed to transform a migrated seismic volume into a band-limited acoustic impedance volume by shaping the seismic spectrum to roughly match the average spectrum observed in impedance logs. Walden and Hosken (1984) shows by empirical observation that all earth reflection series have spectra that exhibit a similar trend that can be simplified as f^{β}, where β is a positive constant and f is a frequency. The exponent of β may vary from one field to another but tends to remain reasonably constant within any one field (Velzeboer, 1981). The spectrum of impedance logs have been observed to behave similarly to reflectivity spectra, but the exponent is negative. This constant is referred as α (Lancaster and Whitcombe, 2000).

The actual colored-inversion is conducted by performing band-pass filtering of the amplitude spectrum of real impedance to the seismic band-width, which then resulting band-limited version of the impedance of the Earth.

In practice, the first step will be determining the colored inversion operator. By using amplitude spectrum of impedance logs plots against frequency on a log-log scale, the average impedance spectrum of the selected wells is determined by fitting a curve to the impedance logs spectrum.

$$AI\,(f) = c * f^{\alpha} \tag{2}$$

where AI is impedance spectrum, c is intercept, f is frequency, and α is the gradient (Lancaster and Whitcombe, 2000).

The seismic spectrum is also extracted by using seismic traces around well-bore. Using both spectrums, the operator spectrum is then calculated to shape the seismic spectrum (Lancaster and Whitcombe, 2000). If α is found for a field by curve-fitting to impedance logs, then the amplitude spectrum of the inversion operator is designed by shaping the mean seismic spectrum to the impedance log in the form of f^{α} (Lancaster and Whitcombe, 2000). The operator is then rotated by phase of -90 degrees, resulting colored-inversion operator. The colored-inversion operator is convolved with each seismic trace to create a relative acoustic impedance volume (Lancaster and Whitcombe, 2000).

Elastic-impedance generalizes the acoustic impedance for variable incidence angle. It provides an efficient way to calibrate and invert nonzero-offset seismic data just as AI does for zero-offset data (Connolly, 1999). Whitcombe et al. (2002) modified definition of previous inversion, thus elastic impedance could be correlated directly to bulk modulus, Lame's parameter, α/β ratio, shear impedance, and shear modulus and can be optimized as fluid or lithology discriminator, by adjusting a single parameter, rotation angle χ. Different χ corresponds to different rock properties (Figure 3.10).

By substitution of $\sin^2\theta$ by $\tan\theta$ to the two-terms of linearized Zoeppritz

$$R = A + B\ \sin^2\theta \tag{3}$$

$$R = A + B\ \tan\chi, \tag{4}$$

the EEI are correspond to expression of

$$EEI(\chi) = \alpha_0\beta_0\left[\left(\frac{\alpha}{\alpha_0}\right)^p\left(\frac{\beta}{\beta_0}\right)^q\left(\frac{\rho}{\rho_0}\right)^r\right] \tag{5}$$

where

$$\begin{aligned} p &= (\cos\chi + \sin\chi) \\ q &= -8K sin\ \chi \\ r &= (co\,s\,\chi - 4K si\,n\,\chi) \end{aligned} \tag{6}$$

Vp, Vs and density are represented by α, β and ρ, respectively. α_0, β_0 and ρ_0 are reference constants. A is the intercept and B is the gradient.

The expressions of equation (3), (4), (5) and (6) define that the rotation in the impedance domain is similar to rotation of intercept and gradient in the reflectivity domain. The inversion of intercept gives RAI, as the intercept correspond to zero incidence reflection, $\chi = 0$, and the inversion of gradient data gives GI. The EEI rotation can be defined as:

$$EEI(\chi) = AI_0\left[\left(\frac{AI}{AI_0}\right)^{cos\ \chi}\left(\frac{GI}{GI_0}\right)^{sin\ \chi}\right] \tag{7}$$

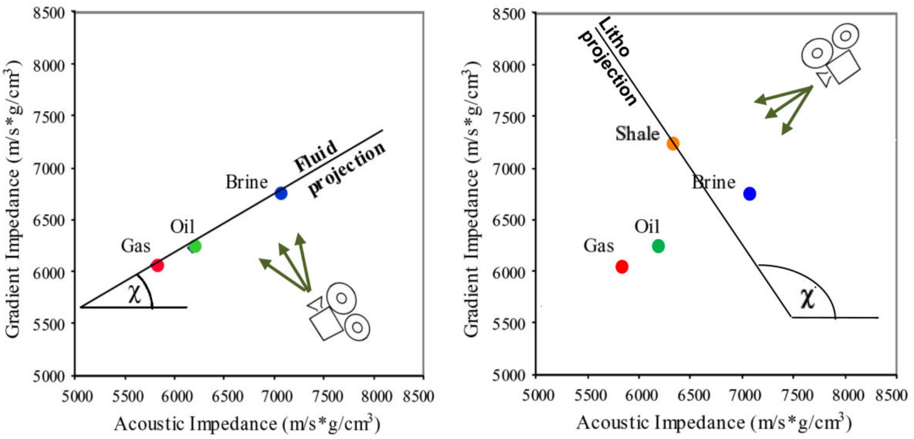

Figure 3.10 Fluid and lithology factors are defined as rotation of χ in intercept (AI or A) and gradient (GI or B) domain (Kemper and Huntbatch, 2012).

CHAPTER 4.

ROCK PHYSICS DIAGNOSTICS

The variation of elastic parameters and some physical parameters such as density and porosity in siliceous sediments may vary significantly depending on the mineralogical composition, pore-fluid properties, depositional environment and post depositional process. In order to extract the information about hydrocarbons presence from seismic, it is important to understand the rock properties in prior as seismic is directly correlated with elastic parameters and density. The implications of various rock properties are proven to affect the seismic data.

4.1 LITHOLOGY CLASSIFICATION

The architecture of the Paleocene turbidite system in Grane area suggests that the depositional system is similar to Lobe-Channel-Levee-Complexes (Statoil Internal, 2013). On this system, channel-like features cutting down the pre-existing lobe features laterally. Although only one channel-levee system was apparently active at any given time, repeated channel avulsion developed groups of overlapping across the upper to middle fan surface (Kneller et al., 2009). This condition suggests heterogeneity in context of channel distribution extent. The clean channel sands of Lower Heimdal formation spreads in the inter-leevee area. The levee or the overbank composition may vary, range from proximal (sand-dominated) to distal (mud-dominated) varieties (Nilsen et al., 2008). The levee, such as Paleogene shales are deposited under bathyal to subtlitoral marine (proximal) environment. This suggests that sands will be dominant over shales. For this reason, it is more convenient to classify the Paleogene shales as shaly-sands than shales. This argument will be confirmed in rock-physics analysis.

In summary, there are four lithologies that are introduced within this study. The turbidite system comprises of shaly-sands and sands, the tuff unit of Balder Formation as the result of volcanic activity, and the limestone unit of Shetland Formation. The shaly-sands unit is divided based on its formation's name to give a better understanding of how the depositional environment relates to rock-physics. The sandstone unit is also divided as two groups, oil-saturated sandstones, and brine-saturated sandstones, as the pore-fluid has a unique relationship within sandstone interval. Classification of lithofacies as function of depths is based upon core-description given by Statoil Internal's report.

4.2 COMPREHENSIVE DIAGNOSTIC

As diagenetic process advances with time, the increasing effective stress from overburden resulting the different degree of compressibility for different lithology. Normally after sediments reach at a certain depth, mechanical compaction ceased and chemical compaction starts to be more predominant.

With function of depth, porosity for each lithology shows a unique trend that corresponds to increasing burial stress. Compare to sands, porosity loss given by shaly sands comes with greater loss (Figure 4.1). Shales tend to compact more easily than sands. Higher platy shaped clay fabric in shaly-sands allows them to be more prone to compaction than the assemblage of spherical grain in sands (Avseth et al., 2003).

Chemical compaction onset

Substantial changes in the P-wave velocity, porosity and density usually indicate the onset of quartz cementation. The P-wave velocity will normally higher than overlying unit as the rock become stiffen due the increasing grain contact as product of quartz cementation. This event is normally followed with decreasing porosity. Adopting these rules of thumb on Figure 4.1 and Figure 4.2a, the sharp velocity increment and density decrement on orange-points suggest the onset of chemical compaction. The onset lies on shaly-sands interval of Hordaland formation at depth of 1640mTVDSS for the F-well and 1620mTVDSS for the D-well.

The cross-plots given by Figure 4.1 and Figure 4.2a show that the degree of sensitivity corresponds to the onset of chemical compaction is different for porosity and P-wave velocity. The chemical compaction onset is most apparent in P-wave velocity changes (Figure 4.2a) because the small amount of mineral precipitation and quartz cementation formation in shaly-sands will increase the stiffness significantly.

Under the influence of chemical compation, quartz-cementation usually appears with higher percentages in clean sandstones rather than in shaly-sandstones. However, with abundant of clay coating, precipitation of these minerals will coat the grain, and prevent the precipitation of quartz cement (Bjørlykke and Jahren, 2010). The porosity of clean sandstones within Lower Heimdal and Upper Heimdal formation appears with high porosity features – inferring slower rate of quartz cementation. Chemical compaction is a continuous process, but with the grain coating such as amorphous silica and chlorite in sandstones, particularly in the Lower Heimdal formation, will inhibit further chemical compaction and preserves the porosity. This will be explained on next sub-chapter.

The transition from mechanical to chemical compaction in the D-well lies at 20 meter shallower than in the F-well (Figure 4.1). In the F-well, the depth of 1640 mTVDSS corresponds to 76^{0}C, while in D-well depth 1620 mTVDSS corresponds to 65^{0}C (Figure 4.2b). It is interesting that only the F-well conforms the theoretical study where chemical compaction mostly starts around 70-80^{0}C. Using this evidence, it is assumed that the D-well once have been subsided deeper than its current position. Based on information in Table 1, the thickness of Lower Heimdal formation to Hordaland Group sediment were greater at the D-well compare to the F-well. This corresponds to the condition that the D-Well was once subsided deeper than the the current position, probably during Late Paleocene to Early Oligocene.

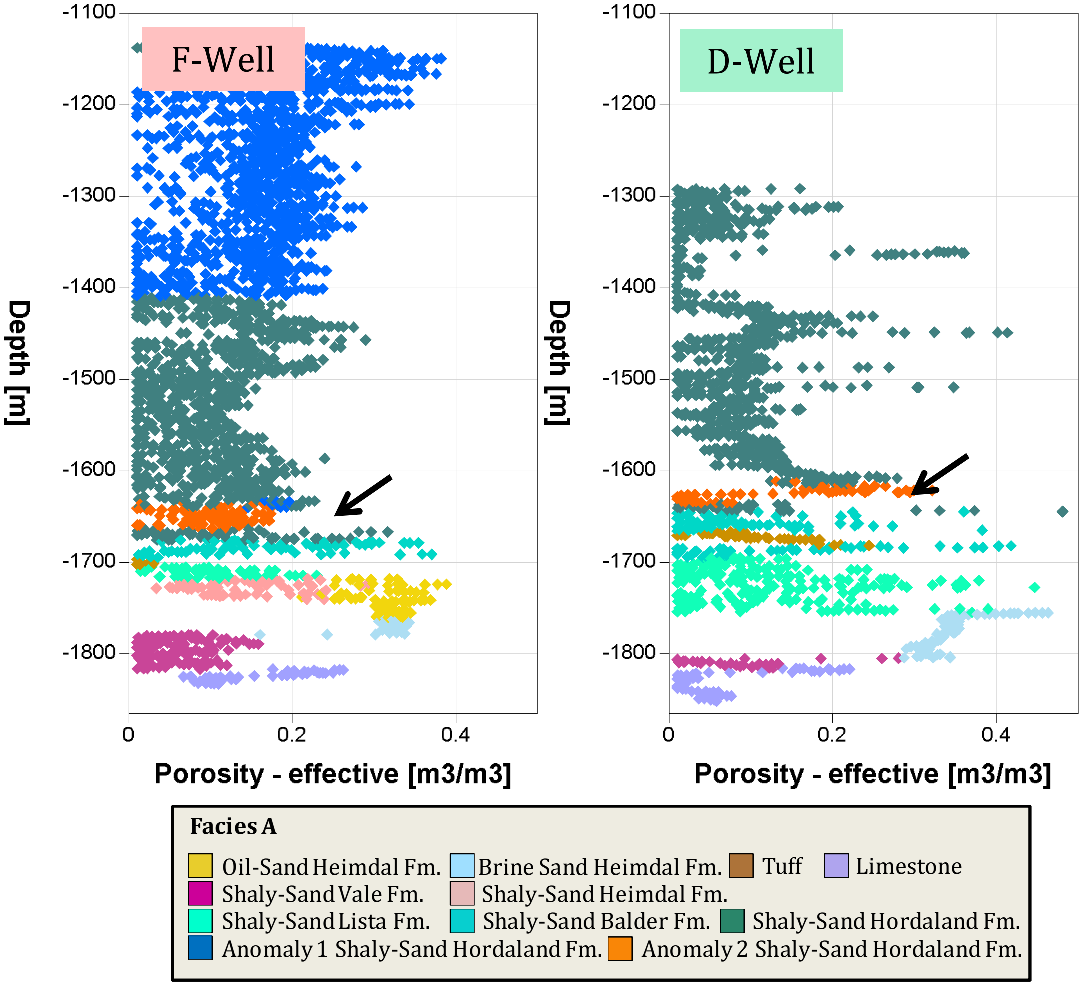

Figure 4.1 Porosity versus depth (mTVDSS). Shaly-sand showing onset of chemical compaction shown as orange color.

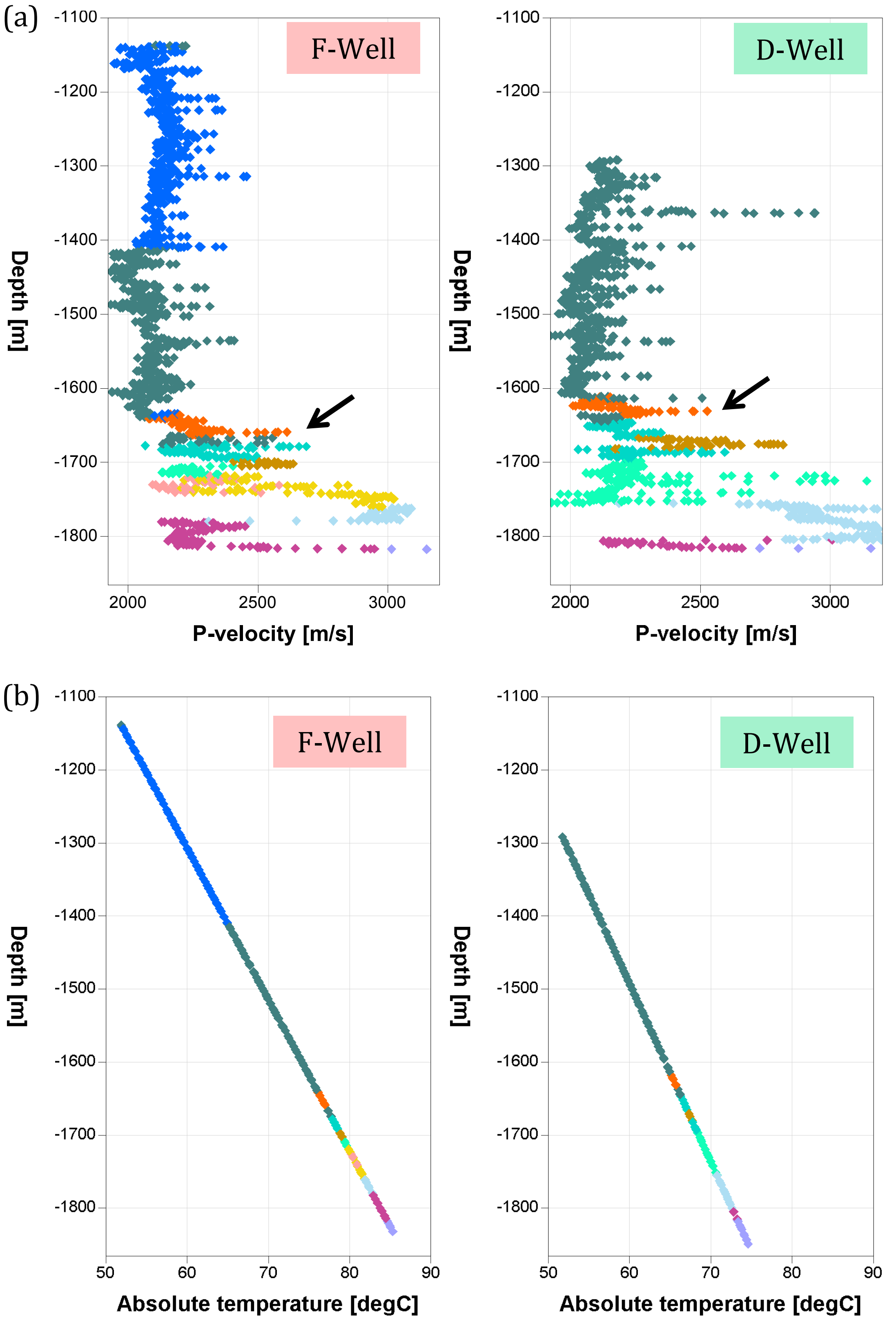

Figure 4.2 (a) Porosity versus depth (mTVDSS), (b) Absolute temperature versus depth (TVDSSm). Shaly-sand showing onset of chemical compaction shown as orange color. Lithology description refers to Figure 4.1.

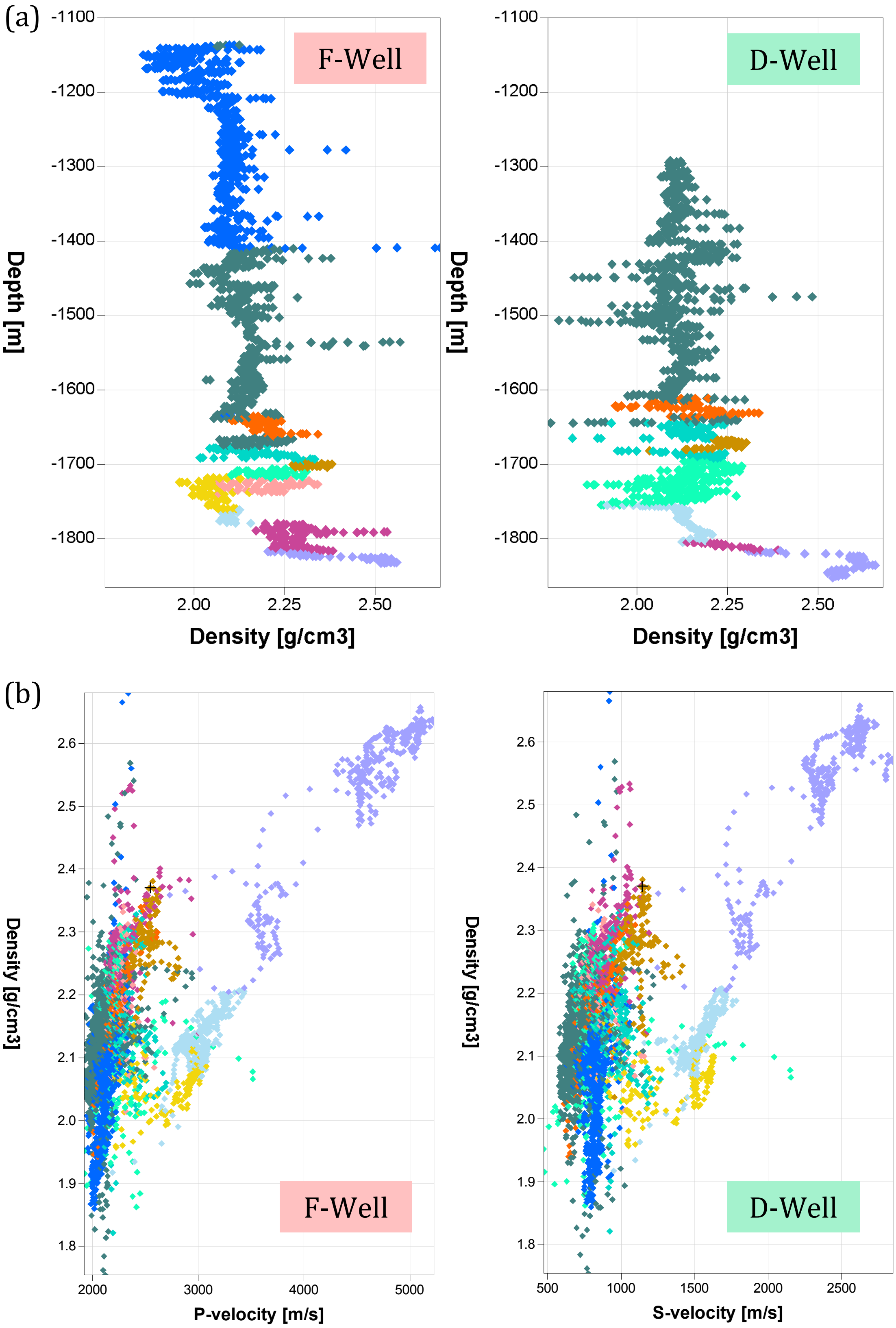

Figure 4.3 (a) Density versus depth (mTVDSS), (b) Density versus P-wave velocity. Shaly-sand showing onset of chemical compaction shown as orange color. Lithology description refers to Figure 4.1.

Elastic Parameter Sensitivity to Lithology Changes

V-turned shape is observed in both velocity density plots, where velocity has more sensitivity in distinguishing sandstones, shaly-sandstones and limestones (Figure 4.3b). Sandstones lithology has higher velocity compare to tuff and shaly-sands, and less deviation in density compare to shaly-sands. Limestone is the easiest lithology to be defined.

Clean sandstones are only around 55 meter thick, or 5-6% from total lithology thickness, while shaly-sands are the most predominant lithology for both well. Sandstones intervals sit below the onset of cementation, means that sandstones features are predominantly affected by chemical compaction rather than mechanical compaction. Shaly-sand in contrary, affected with both events – increasing effective stress during mechanical compaction and quartz cementation effect during chemical compaction. Such events may explain the reason of why density of sandstones has less deviation than shaly-sand (Figure 4.3b). Another possible explanation of higher deviation in density is due to the anisotropy. The increasing effective stress in grain supported clay will cause the platy clay fabric to assemblage into a more parallel orientation. Such event will increase the anisotropy, causing more deviation in density as depth function (Figure 4.3a).

Combination of P-wave and S-wave velocity introduces a cross-plot with a linear trend that corresponds to the increasing shaliness downward (Figure 4.4a). Comparing to previous plot (Figure 4.3b), the transition of shaly-sand to tuff and shaly-sand to oil-saturated sandstones appears overlapping even more. Combination of gamma ray and P-wave velocity, able to distinguish shaly-sandstone from clean sandstones with gamma-ray cut off around 32 API, and P-wave velocity around 2700 m/s (Figure 4.4b). Tuff lithology appears as transition between these two lithologies. As agreed with previous cross-plots, limestone is the easiest lithology to define.

(a)

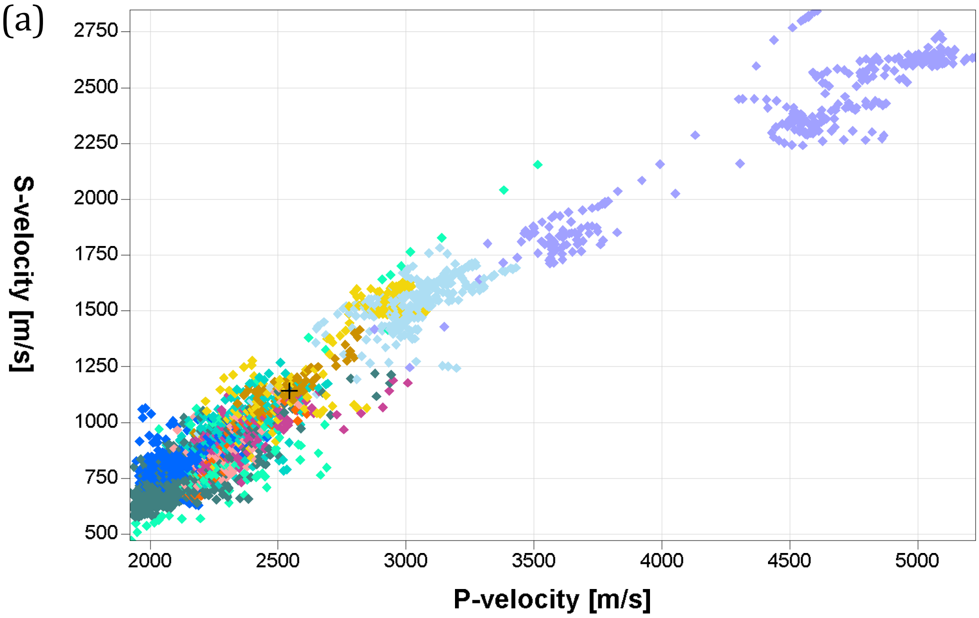

P-Wave Velocity versus S-Wave Velocity *Facies A*

(b)

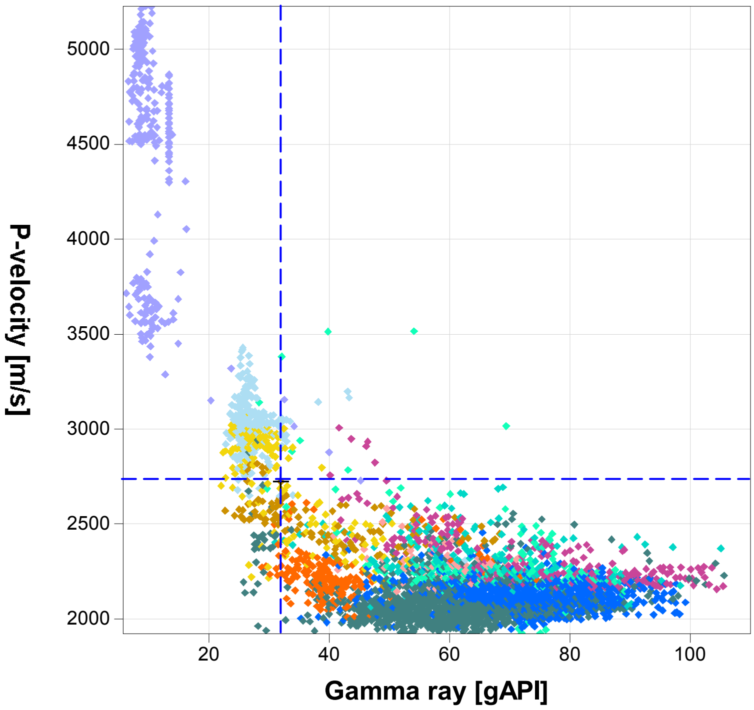

Facies A

■ Oil-Sand Heimdal Fm. ■ Brine Sand Heimdal Fm. ■ Tuff ■ Limestone
■ Shaly-Sand Vale Fm. ■ Shaly-Sand Heimdal Fm.
■ Shaly-Sand Lista Fm. ■ Shaly-Sand Balder Fm. ■ Shaly-Sand Hordaland Fm.
■ Anomaly 1 Shaly-Sand Hordaland Fm. ■ Anomaly 2 Shaly-Sand Hordaland Fm.

Figure 4.4 (a) S-wave versus P-wave velocity, (b) P-wave velocity versus Gamma Ray

4.3 SHALEY SAND LITHOLOGIES

Compactional trends

It is interesting to denote that there are two different trends in Figure 4.5. As one go to shallower depth along the black line, the gamma ray is increasing followed by increasing P-wave velocity. Meanwhile by following the blue line, the gamma ray is decreasing as advancing depth, and followed by increasing P-wave velocity.

Avseth et al. (2003) shows that the increasing depth is normally followed with increasing P-wave velocity, as function of porosity loss. However, Figure 4.5 confirms that increasing depth is not followed with increasing velocity. For this condition, it is thought that the increasing P-wave is highly dependent to depositional system, rather than the effect of mechanical compaction. The depositional environment and the provenance of the clastic sediments determine the composition for diagenetic process (Bjørlykke and Jahren, 2010). Marrion (1990) shows that increasing clay content corresponds to increasing P-wave value, as the clay stiffens the rock. The black-colored trend shows that gamma ray values in depth range around 1400 to 1640 mTVDSS are increasing as it proceeds to shallower depth. As the depth increase, the lithology of shale is changing from clay rich to less clay – from bathyal to outer sublitoral marine environment, allowing the decrement of gamma-ray.

The blue-colored trend, with depth onset around 1640 mTVDSS at F-well and 1620mTVDSS at D-well, shows that by increasing depth will increase the velocity (Figure 4.5). This trend also followed by the trend of lowering fraction of clay. Such event is interpreted as onset of chemical compaction. The lowering fraction of clay usually occurs as the chemical compaction predominantly affects the shaly-sand system. On this condition, clay mineral such as smectite becomes unstable and dissolved and replaced by minerals such as illite and quartz. The increasing amount of quartz cementation will reduce the amount of clay.

Depositional trends

In topological model for sand-shale models, when the clay content is less than the sand porosity, clay particles are assumed to be located within pore-spaces of load-bearing sand (Marion, 1990; Avseth, 2010). The presence of the clay will stiffen the pore-filling material without affecting the frame properties of sand (Avseth, 2010).

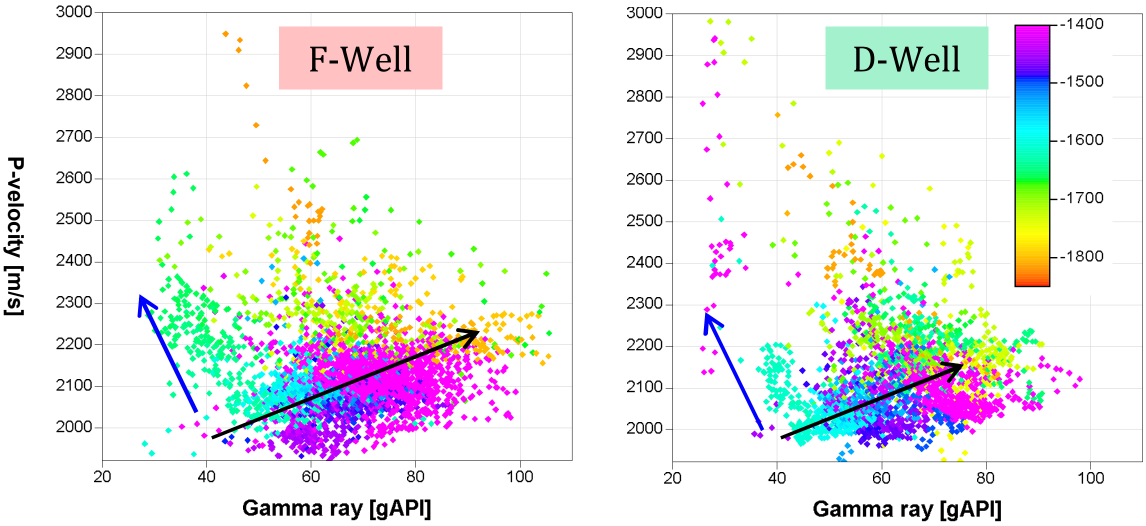

Figure 4.5 Cross-plots of gamma-ray versus P-wave velocity. Black-colored trend showing the depositional trend with function of depths, and blue-colored trend showing the chemical compaction effect.

With increasing clay fraction, or gamma ray, the amount of porosity-effective is decreasing (black-colored arrow at Figure 4.6a), followed with increasing velocity (Figure 4.6b). P-wave velocity is increasing with increasing clay fraction as the bulk modulus of pore-filling materials is higher, ie. fluid and clay. However, unlikely it affects the P-wave velocity, the pore-filling clay and fluid would not significantly affect the shear modulus of the rock (Figure 4.7b).

Previous paragraph summarizes that the increasing clay content in shaly-sand mixture will be followed with decreasing the porosity-effective and increasing the velocity. This condition is only applied when the clay content increases up to a given point called critical clay content that is a point of transition from shaly-sands to sandy-shales. The transition point usually appears at 40% clay fraction (Marion, 1990). After this point, refer as Marion (1990) second term, the trend of increasing clay content will be conformed to decreasing velocity and increasing porosity (Figure 4.6a and Figure 4.6b). The second terms of Marion appear not to be applicable for any case in both wells, since no such trend observed to be coherent with this theory. In both cases inferred that sand-shale mixture lithology are predominantly shaly-sands than sandy-shales or even pure shales. Gamma-ray value up to 120 API is reasonably coherent with fraction of clay that is less than critical clay content, ie. less than 40% of clay content.

Han et al. (1986) observed that as the bulk modulus increases, the deviations of porosity also increase up to 10%. This agreement is shown as an abnormal behavior in the F-Well, where the sharp deflection occurred at porosities greater than 18% (blue-colored points at Figure 4.6b and Figure 4.7b). With the same porosity and clay content, the anomaly's velocity is higher than other samples. Han et al., (1986) explains that the interactions between the pore fluid, ie. water and clay mineral, cause the bulk modulus of water-saturated clay to increase. The effect of water-saturation in clay mineral caused the micropores being structurally more rigid than dry ones, ie. interaction between smectite and water (Bjorlykke, 2010b).

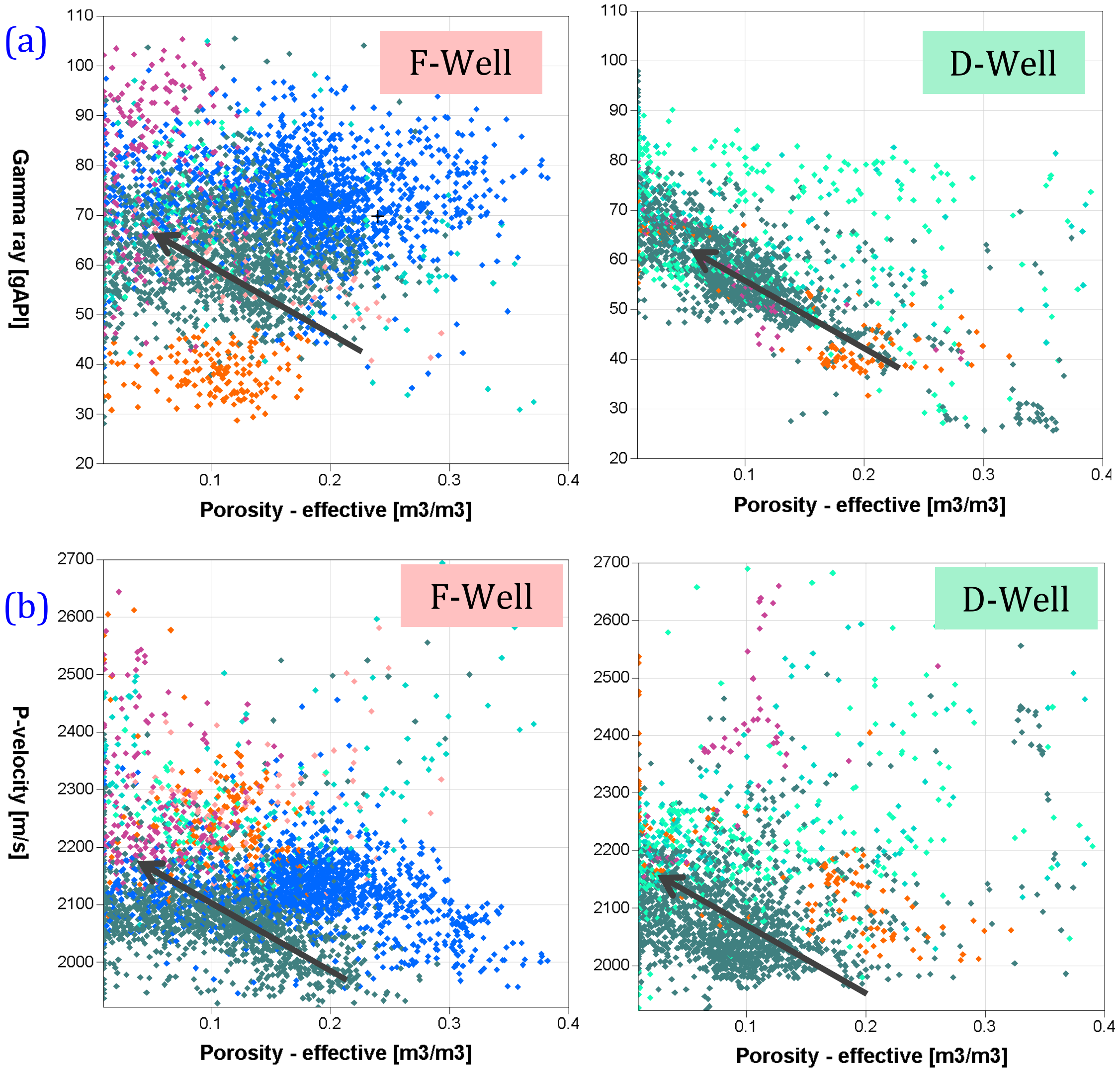

Figure 4.6 Cross-plots of (a) Gamma-ray versus porosity, (b) P-wave velocity versus porosity. Black-colored trend showing the depositional trend with function of depths. Blue colored points correspond to anomaly related to high water saturation in clay mineral. Orange colored points correspond to anomaly related to the chemical compaction effect.

Another anomaly trend is observed at gamma ray less than 50, at depth around 1640 mTVDSS at F-well and 1620mTVDSS at D-well (orange-colored points at Figure 4.6a and Figure 4.7a). Anomaly is represented by the trend of velocity increment followed with decrement clay amount. Normally, according to Marrion (1990) with increasing clay content, velocity also increases. Therefore, rather than interpreted as lithology changes, the presence of anomaly is reflecting the starting point of chemical compaction. This argument is coherent with the previous argument in Chapter 4.2.

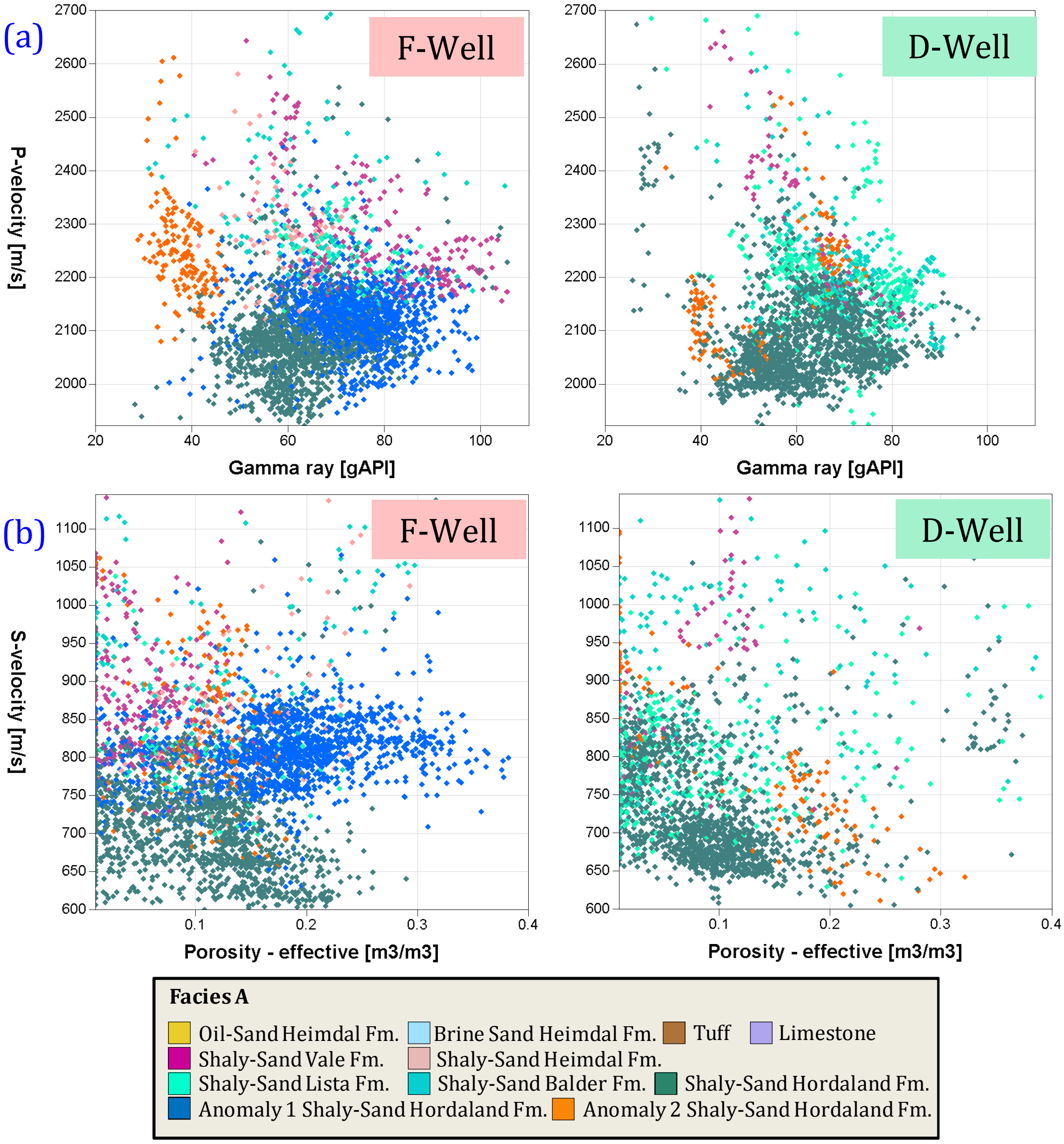

Figure 4.7 Cross-plots of (a) Gamma-ray versus P-wave velocity (b) S-wave velocity versus porosity. Black-colored trend showing the depositional trend with function of depths. Blue colored points correspond to anomaly related to high water saturation in clay mineral. Orange colored points correspond to anomaly related to the chemical compaction effect.

4.4 SAND LITHOLOGIES

4.4.1 THIN SECTION ANALYSIS TO ROCK PHYSICS MODEL (RPM)

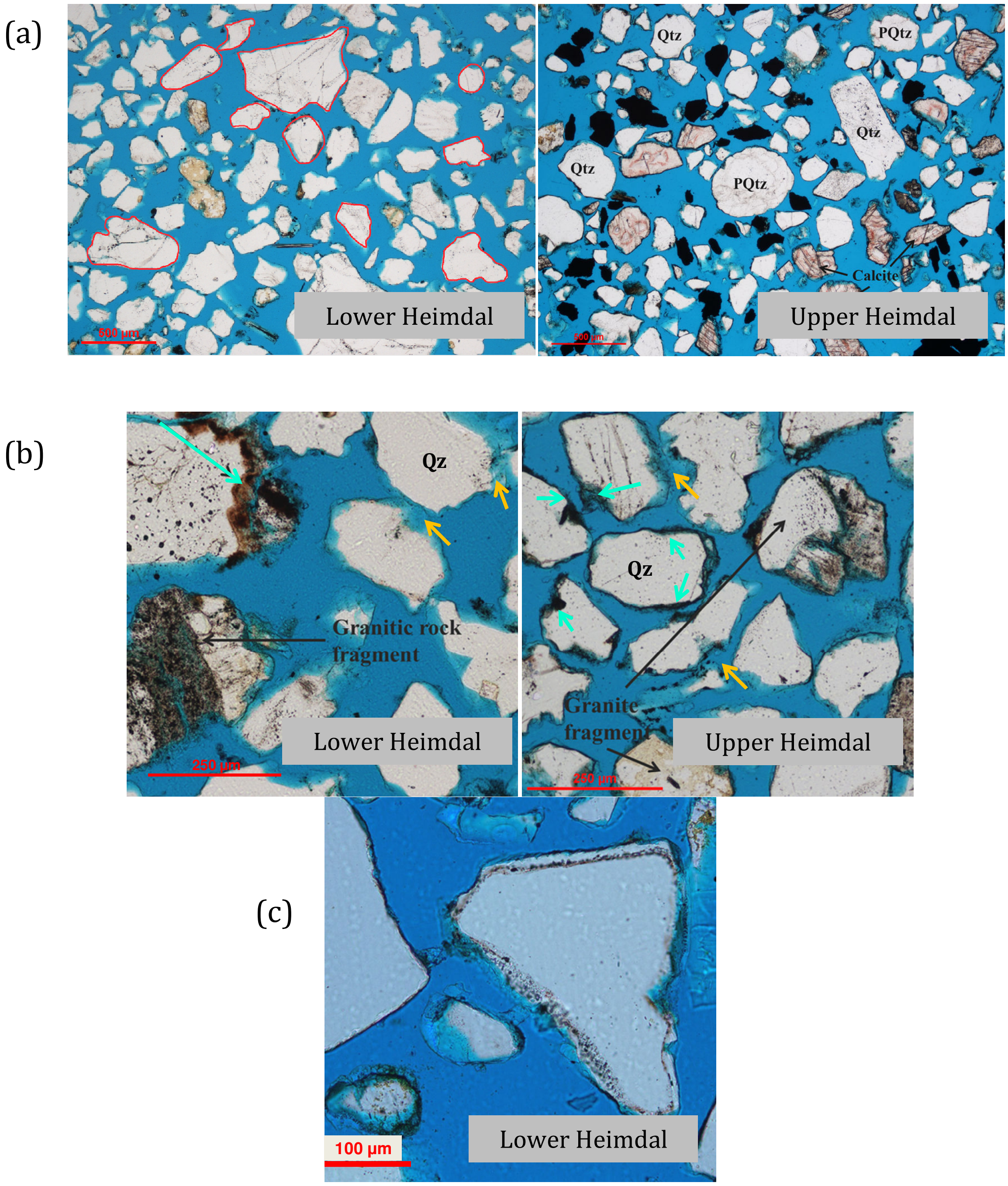

Figure 4.8. Thin section samples from F-well. (a) The Upper Heimdal presents with finer grain sizes than the Lower Heimdal. Cyan arrow at (b) showing chlorite coating. It is denoted by brown-dark rim in quartz grain. More abundant chlorite coating found in the Upper Heimdal sample (b) than in the Lower Heimdal. (c) Quartz overgrowth in Lower Heimdal. Grain is coarser at Lower Heimdal. Yellow arrow at (b) showing cementation.

Unit	Well	Depth (MD)	Grain Size	Grain Sorting	Porosity
Claystone	25/8-4	1720-1780			1-22%
		1830-1836			18-21%
	25/11-27	1730-1743			2-23%
		1743-1766			4-18%
		1803-1804.5			8-20%
Sandstone	25/8-4	1720-1780	Fine to Med Sands	Mod Sorted	26-45%
		1780-1830	Fine to Med Sands	Mod Sorted	30-44%
	25/11-27	1743-1766	Fine to Med Sands	Well Sorted	23-40%
		1766-1804.5	Fine to Med Sands	Mod Sorted	30-37%

Unit	Well	Depth (MD)	Grain shape	Microstructure	Cement
Claystone	25/8-4	1720-1780			
		1830-1836			
	25/11-27	1730-1743			
		1743-1766			
		1803-1804.5			
Sandstone	25/8-4	1720-1780	Subangular-subrounded	Cemented	
		1780-1830	Subangular-subrounded	Cemented	Siliceous Cement
	25/11-27	1743-1766	Subrounded	Friable	
		1766-1804.5	Subangular-subrounded	Cemented	Calcite Cement

Table 3. Sample description of Upper Heimdal and Lower Heimdal formation given by the F-Well. Description includes grain sizes, grain sorting, grain shape, microstructure, cement mineralogy, porosity.

Six thin sections were prepared for Upper Heimdal formation and nine thin sections for Lower Heimdal formation (Figure 4.8). All samples were taken from sandstones interval of the F-well. Quartz is the dominant mineral with range of 44-52% for the Lower Heimdal, and 34-44% for the Upper Heimdal of total sample volumes. There are also pyrite-cements observed within two formations. This trace may indicate chlorite presence as chlorites are mostly observed within pyritic sediments (Van Breemen, 1980). It explains that in anoxic sea bottom, smectite within sediments will transform into pyrite.

Analyzing the samples and comparing to the observations of Mørk and Moen (2007) and Avseth (2000), the brown-dark rim in quartz may represent the chlorite-grain coating around the quartz (Figure 4.8). The intensity of chlorite coating in the Upper Heimdal is relatively more intense compare to the Lower Heimdal formation.

The amount of cementation seems coherent with the amount of chlorite coating. The more abundant the chlorite coating, the more absence is the cementation. With less cementation, the Upper Heimdal sandstones presents with higher porosity compare to the Lower Heimdal sandstones. This event also supported with log-data, PHIE (Table 3). However, the porosity variations may also affected by the grain textures and sizes. In more fined and rounded-shaped grain like the Upper Heimdal formation, at the same stress level the contact of more spherical grain will compact much less compare to coarser sand, preserving the porosity in higher rate.

Avseth et al., 2000, Avseth, 2010 and Dvorkin and Nur, 2002 discovered that velocity increases as the porosity reduces. This condition corresponds to depositional trend where the porosity reduction refers to deteriorating grain sorting. Due to the lower sorting quality of Lower Heimdal formation, P-and S-wave of the formation will be higher than the Upper Heimdal formation. Moreover, the intensity of cementation may also contribute in velocity variation. With reducing porosity due to cementation, grains are stiffened, increasing the bulk modulus and velocity of sandstones.

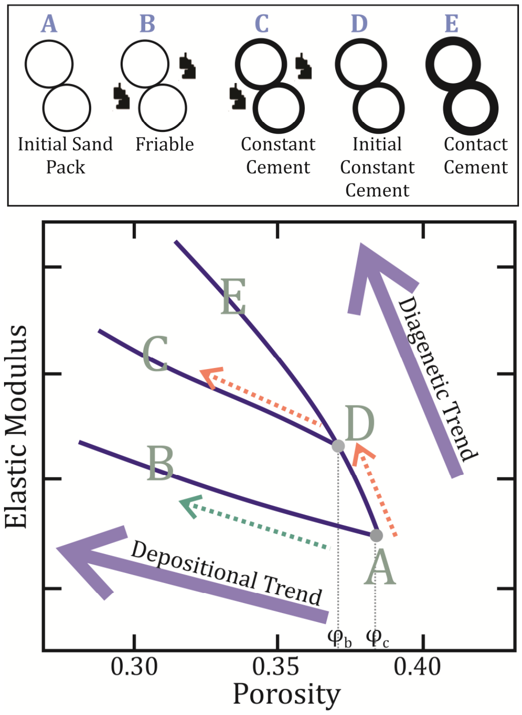

Figure 4.9 As function of porosity and elastic modulus, Lower Heimdal Formation is denoted by orange-colored arrow while the Upper Heimdal is by green-colored arrow.

In RPM domain, the Upper Heimdal sandstones fit the friable model or uncemented sandstones model (Figure 4.9 and Figure 4.10). Contrary, the Lower Heimdal formation sandstones have little initial contact cementation (Figure 4.9 and Figure 4.10 point A-D), followed with constant cement model (point D-C). At contact cementation trends (point A-D), cementation produced a stiffening effect, and porosity reduces from initial porosity of sand pack due the uniform deposition of cement around the grain (Avseth, 2010). At certain point, diagenetic process deceased, and depositional process become more dominant (point D-C). Sands with varying porosity have the same amount of cement. Porosity varies as the organization of non-contact pore-filling material or deteriorating sorting (Avseth, 2010). Porosity reduces from point called φ_c to φ_b and followed with more porosity reduction as function of deposition, on which the solid phase away from the grain contacts (Avseth, 2010). This observation is supported by the presence of quartz overgrowth between quartz grain and quartz cement in thin section analysis. It indicates that these grains were derived from older quartz-cemented sandstones, or the grains had lost their original position from the previous sandstone structure (Statoil Internal, 2013).

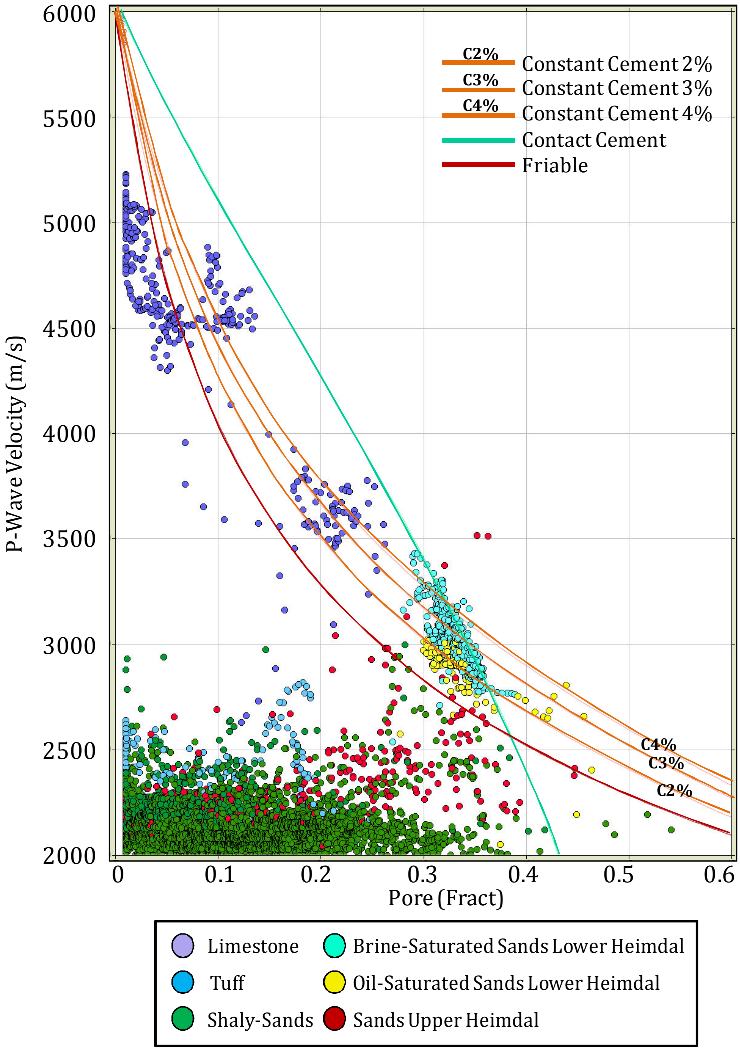

Figure 4.10 P-wave and S-wave velocity relatives to porosity. Log observations suggest the Upper Heimdal formation is fitted to friable sand model, while the Lower Heimdal formation is fitted to contact- and constant cement.

4.4.2 LOWER HEIMDAL

Influence of Cementation

The temperature in Lower Heimdal formation in average is 72^0C at the D-well and 82^0C at the F-well. From previous observations, it is known that within this range, chemical compaction become more dominant. The amount of quartz cement is function of grain surfaces available for quartz precipitation, presence of grain coatings, subsidence rate and the time-temperature function (Bjørlykke and Jahren, 2010). From thin section analysis, it has been concluded that such presence of chlorite coating around quartz-grain will preserve the porosity of sandstones.

Analyzing the velocity-ratio versus P-impedance cross-plot (Figure 4.11a), for the same formation, the character of reservoir for each well is represented on a distinct character. The lower P-impedance value in the D-well may correspond to higher degree of cementation compare to the F-well. Based on detail lithostratigraphy information, it is known that mineral cement type is different for each well. The D-well is predominantly siliceous cemented while the F-well is predominantly calcite cemented (Statoil Internal, 2013; Statoil Internal 1993). It is therefore summarized that in the sand cemented model, the fraction of cement and the different property of cement minerals will have strong influence in the value of elastic parameter.

Using this information, RPM for each well is modelled using different degree of cementation and different cement mineral (Figure 4.11b). Brine-saturated sands sit on the upper section of the trends, while oil-saturated sands sit below the trends. The sand on both wells probably contains some clay, since the brine-saturated sand points fall slightly above the 0% oil trend, not exactly on the trend. The effective porosity deviates 5% more in the F-well compare to the D-well.

The thickness of Lower Heimdal in the D-well is 11.5 meter thicker than in the F-well, which leads to assumption that the D-well had been subsided deeper during the Upper Paleocene deposition. This condition introduces a possibility for the Lower Heimdal to have higher cementation on the D-well as the increasing fraction of cement is coherent with increasing burial depth. For this case, RPM predicts that the D-well has 1% more cement than the F-well. From Figure 4.11b, it is shown that within the same porosity interval, the increasing cement fraction leads to decreasing velocity ratio and P-impedance.

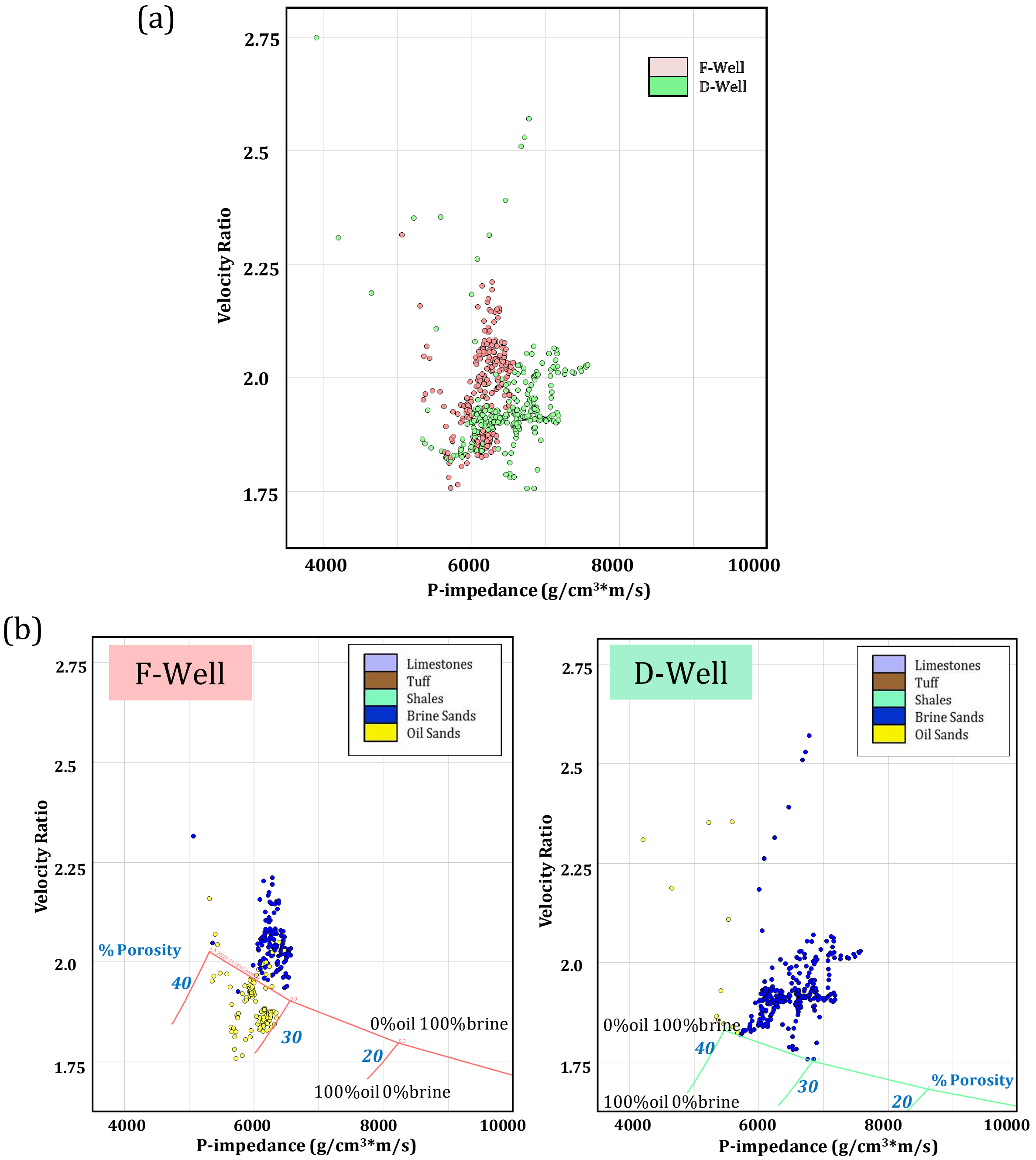

Figure 4.11 (a) The F-well values is shifted towards higher velocity ratio and lower P-impedance. (b) Using constant cement model, Lower Heimdal sandstones is defined by 4% calcite cement at F-well and 5% siliclastic cement at D-well.

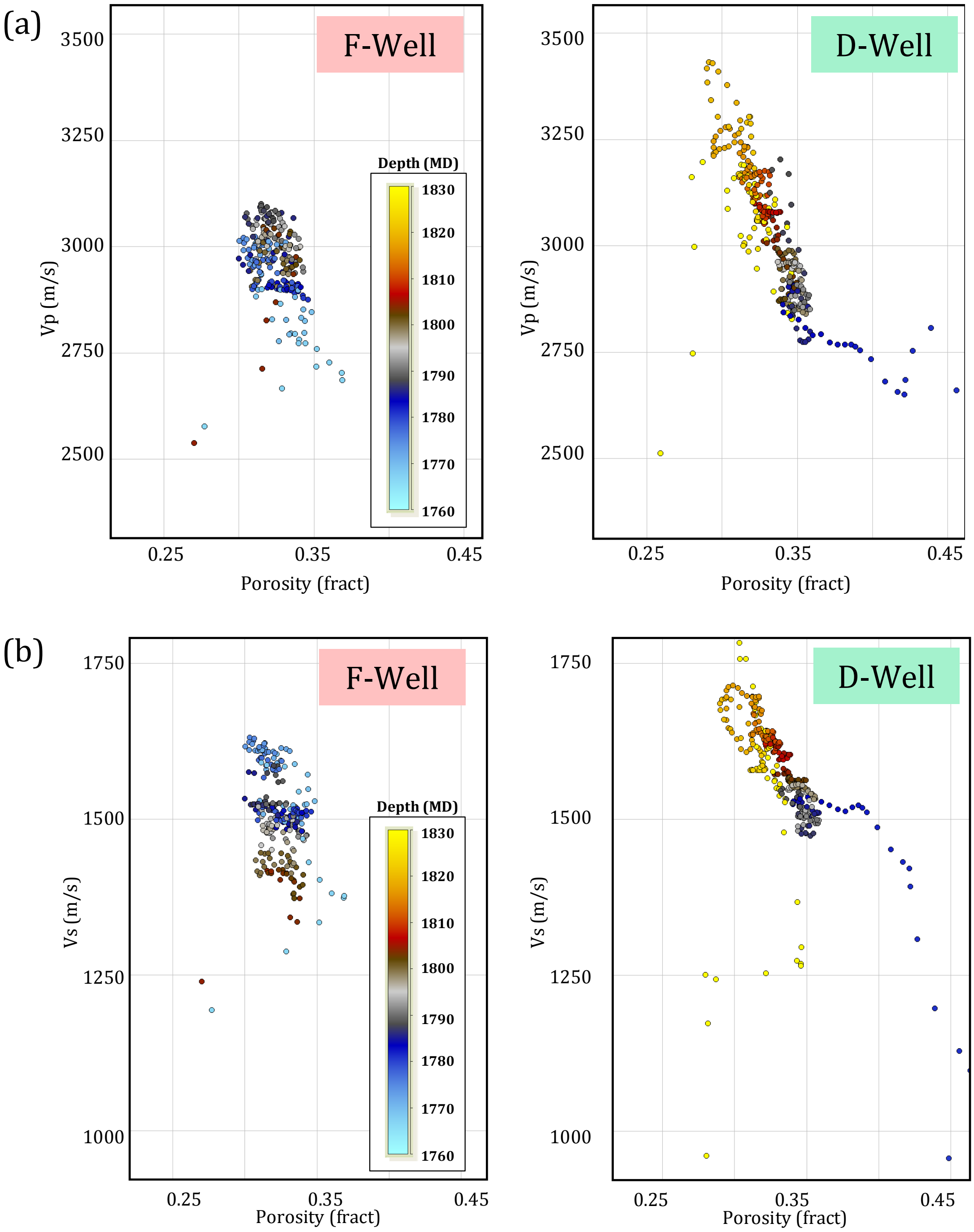

Figure 4.12 Given by each well, (a) P-wave velocity versus porosity, and (b) S-wave velocity versus porosity as function of depth.

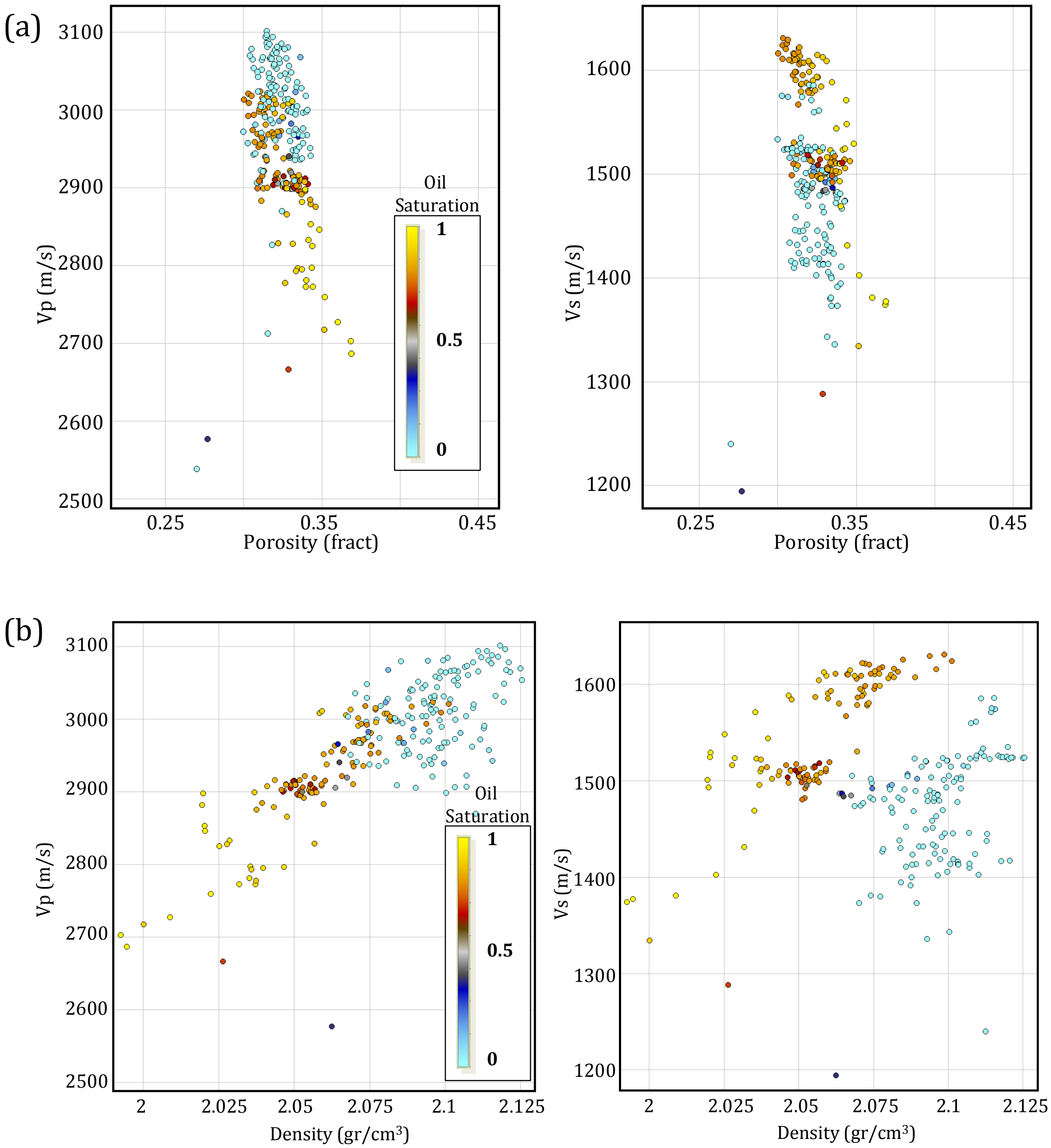

Figure 4.13 Given by F-well log-data (a) Velocity versus porosity, and (b) Velocity versus density as function of oil saturation.

Influence of Pore-Filling Fluid

Increasing burial depth in chemical compaction system will stiffen the rock by introducing higher degree of cementation. Such mechanism leads to decreasing porosity and increasing effective moduli as well as velocity.

Figure 4.12a and Figure 4.12b shows the velocity plot versus porosity with respect of depth (MD) value. The cross-plot shows that porosity is preserved around 32% with changing of depth on the F-well, while on the D-Well porosity changes with function of depth. In other words, the porosity on the F-Well is given with less deviation than the D-well. Some experiments show that the presence of oil may inhibit quartz cementation, preserving the porosity, and “removing” the effect of increasing degree of cementation as function of depth (Bjørlykke and Jahren, 2010; Avseth, 2008). This situation is therefore explaining the porosity preservation in F-well. Moreover, such preservation is also expected in sandstones with abundant calcite cement. Large amount of calcite may contribute to quartz cementation inhibition in fine-grained sediments where dissolution of grain and calcite cements will increase porosity as acid fluids are accumulated (Ji, 2013; Net, 2013).

It is also noted that pore fluid content, ie. brine filled sandstones or oil filled sandstones, affects the trend of velocity changes, and therefore the changes of velocity is not always followed with the increasing burial depth or degree of cementation. With increasing saturation of oil will also mean decreasing P-wave velocity and increasing S-velocity (Figure 4.13a and Figure 4.13b, respectively). This observation aligns with observation of Han et al. (2007), where lowering P-wave velocity at oil-filled sands is consistent with the fact that bulk modulus of oil at depth around 80^0C is lower than brine.

4.4.3 UPPER HEIMDAL

The Upper Heimdal formation mainly consists of laminated sand and shaly-sands, where sandstones are mainly oil-wet. The P-wave and S-wave velocity for Upper Heimdal sandstones are lower than the Lower Heimdal sandstones (Figure 4.15a). Such events may be caused by the different type of microstructure of sandstones that relates to the cementation effect and quality of sorting. Thin section analysis has previously confirmed that higher cement content and more poorly-sorted grain will correspond to higher velocity. Moreover, it is observed that for the same density range, the gamma ray value of the Upper Heimdal sandstone is higher than the Lower Heimdal sandstones (Figure 4.14a and Figure 4.14b). This observation illustrates that the small amount of claystone within Heimdal sandstones will cause the velocity to decrease.

Sand Injectites, Hydrocarbon Pore-Filling and Degree of Calcite Cementation

The Upper Heimdal formation is interpreted as injected sands (Statoil Internal 1993. Its sandstones character that appear as thin unit overlying a massive depositional sand body and separated by some meters of shales, provide good reason to confirm this interpretation (Briedis et al., 2007).

Sand injecites formed as shallow crustal process by release of overpressure fluids and continued with forming fluid conduit as an act for fluid to escape throughout burial (Jonk et al., 2005; Schwab et al., 2014). Sand injection occurred when the minimum estimate of burial depth 400 -500m. The Tertiary injectite of the North Sea, consisting of unconsolidated sandstones from Paleocene and Eocene parent rock is assumed to occur with response to earthquake activity (Jonk et al., 2005). This tectonic activity appears as relation to the North Atlantic breakup and Alpine collision which cause basin inversion throughout north-west Europe during Late Eocene, and this condition is relevant to the injectite formation where injectite sands are shallowly buried (Jonk et al., 2005; Huuse et al., 2004). It is important to have overpressure condition in unconsolidated parent-sand to occur prior to hydraulic fracturing of the sealing-mudstone, and fluidized transport grains into these fractures as sand injection (Jonk et al., 2005). During this time, surrounding mudstones were suggested to be consolidated with the effect of burial stress (Hamberg et al., 2007).

The presence of carbonate cementation rate in injectite and parent-sand bodies, also oil in diagenetic carbonate helps in understanding the relative timing of sand injection and petroleum migration (Jonk et al., 2005). There are two possible scenarios that are suitable to explain the distinct cementation rate founded in parent sand and injectite sand:

- *First Scenario:*

  It is where the injectite contains more calcite cementation than parent-sand body. This scenario has been explained by Jonk et al. (2005). With the availability of oil in the parents sands, sands was injected and causing upward migrating oil and basinal brines to be mixed with downward-invading mixed meteoric-marine pore fluids in the injectites. This even causes biodegradation of oil which promote the early carbonate cementation in sandstones, particularly in injecites. Carbonate cementation almost immediately commenced after sand injection occurred.

- *Second Scenario:*

  It is where no calcite cementation in injectite sands. With abundant of chemical characteristics such as smectite in claystone, smectite percipitation will be the main precursor to diagenetic chlorite formation (Humphreys et al., 1989; Dowey, 2012). The effect of clay mineral coatings in sandstones has great importance, because clay minerals in sandstone reservoirs tend to reduce porosity and permeability, and such as chlorite coating will inhibit the formation of later mineral cements such as quartz and calcite (Moraes and De Ros, 1990; Dowey, 2012). If the oil in parents' sands has not been available yet during the sand injection and injectite has formed, the intense contact between mudstones and injectite will lead into chlorite cementation. Diagenic chlorite of iron- and magnesium rich content smectite in nearby mudstones will pervasive within the injectites, and preserves the porosity of sandstone reservoir and inhibit the formation of calcite cement. As the sand injection and chloritic cement established, hydrocarbon migrates. The biodegradation of oil started and generate carbonate cementation. Carbonate cementation occurred significantly within the parent-sands compare to the injectite sands due the effect of chlorite coating within the injectite.

As confirmed in thin section analysis and RPM model (Figure 4.10), cementation rate in injectite sand, Upper Heimdal formation, is relatively absent compare to the parent-sand bodies. Adapting this condition, the formation of injectite sands is more reasonable to be explained by the second scenario. One need to note that the second argument raised base on comprehensive understanding from literatures, and no publication has confirmed the validity. However, first argument may also valid for this study by knowing that calcite cementation as the product of oil biodegradation is locally pervasive as barrier formation between injectites and also parent-sand may occur (Jonk et al., 2005).

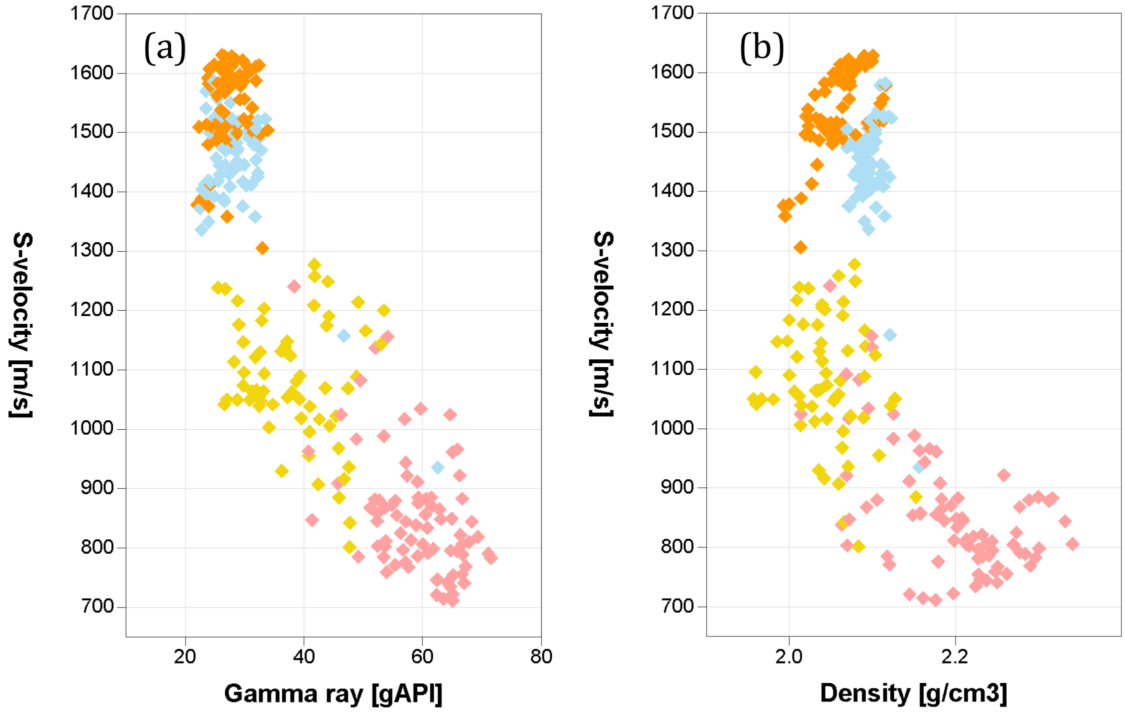

Figure 4.14 Using samples from F-well (a) S-wave velocity versus gamma-ray, (b)S-wave velocity versus density. Lithology description refers to Figure 4.15

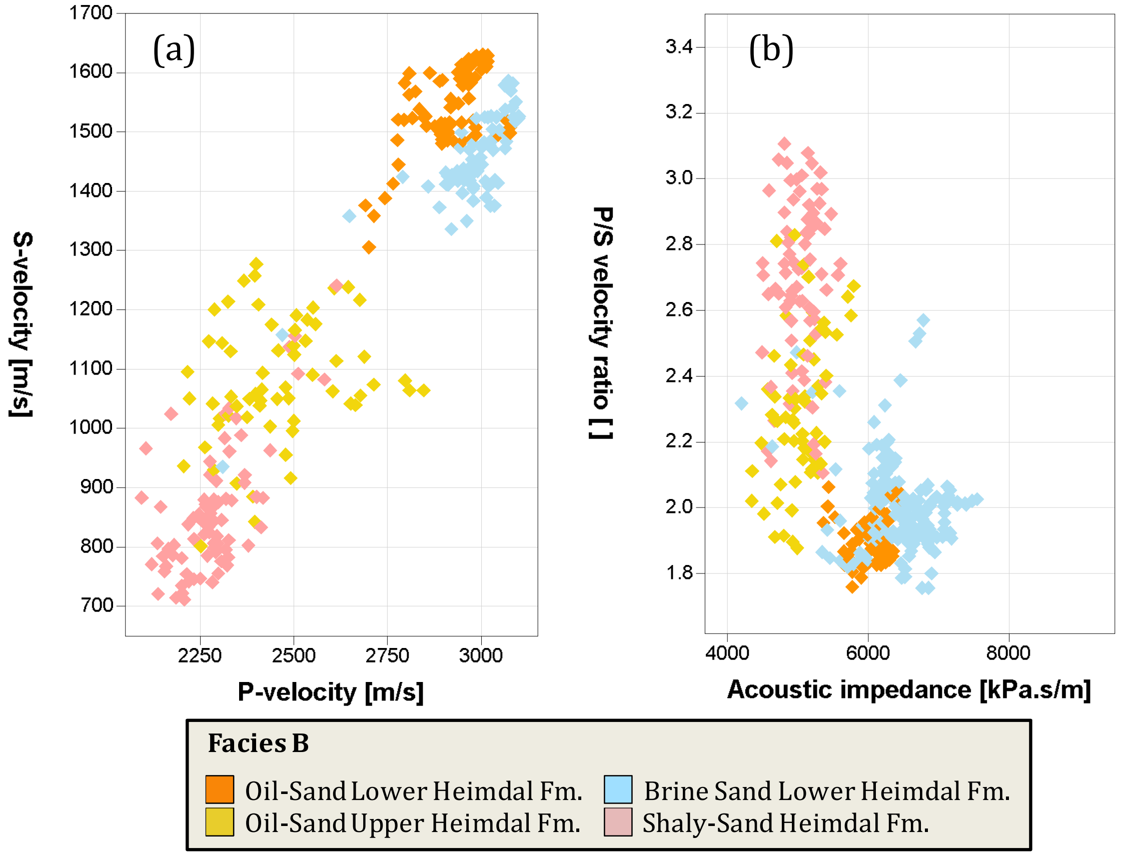

Figure 4.15 Using samples from F-well (a) S-wave velocity versus P-wave velocity, and (b) Velocity-ratio versus density.

CHAPTER 5.

SENSITIVITY ANALYSIS AND AVO/AVA FORWARD MODELING

Oil-saturated sandstone has strong relation with certain AVO behavior. This behavior is reflected by specific value of intercept or reflection coefficient at zero offset or R(0) and contrast in velocity-ratio (Vp/Vs or equivalent to Poisson's ratio). AVO and inversion techniques were proven to be successful in some reservoir characterization over the world, but in many case they were not. The technique suffered from ambiguities caused by lithology effects, tuning effects and overburden effects (Avseth et al., 2005). The best way to start an AVO and inversion analysis is by performing feasibility studies such as forward modeling of AVO response as well as well-to-well lithology prediction. These modeling are carried out as a "what if" scenarios, by using derived P- and S-wave, the density data by Gassmann calculation, and the probability density data given by each well.

5.1 GASSMANN SUBSTITUTION

Rock physics substitution equation introduced by Gassmann (1951) is commonly used to predict the response from a reservoir by proposing a "what if" scenario of pore-filling fluid from the measured well. The Gassmann substitution has been performed by Statoil's internal for calculating P-and S-wave velocity, and density for the F-well and the D-well (Figure 5.1). The present challenge is to deliver seismic synthetics with function of angle whilst accounting the different pore fluid properties, 100% brine-saturated case and 100% oil-saturated case. The AVO model is built based on Zoeppritz calculation using elastic parameters derived from Gassmann substitution, ie. P-wave velocity for oil or brine case. Using this formula, synthetic seismic can be constructed by convolving the derived Gassmann log value with modeled wavelets (Figure 5.2). Wavelets are extracted from near seismic data, using the closest seismic traces relative to the position of the borehole trajectory for each well. Each wavelet has property of zero phase. The target for Gassmann substitution modeling focuses on the top section of Lower Heimdal Formation.

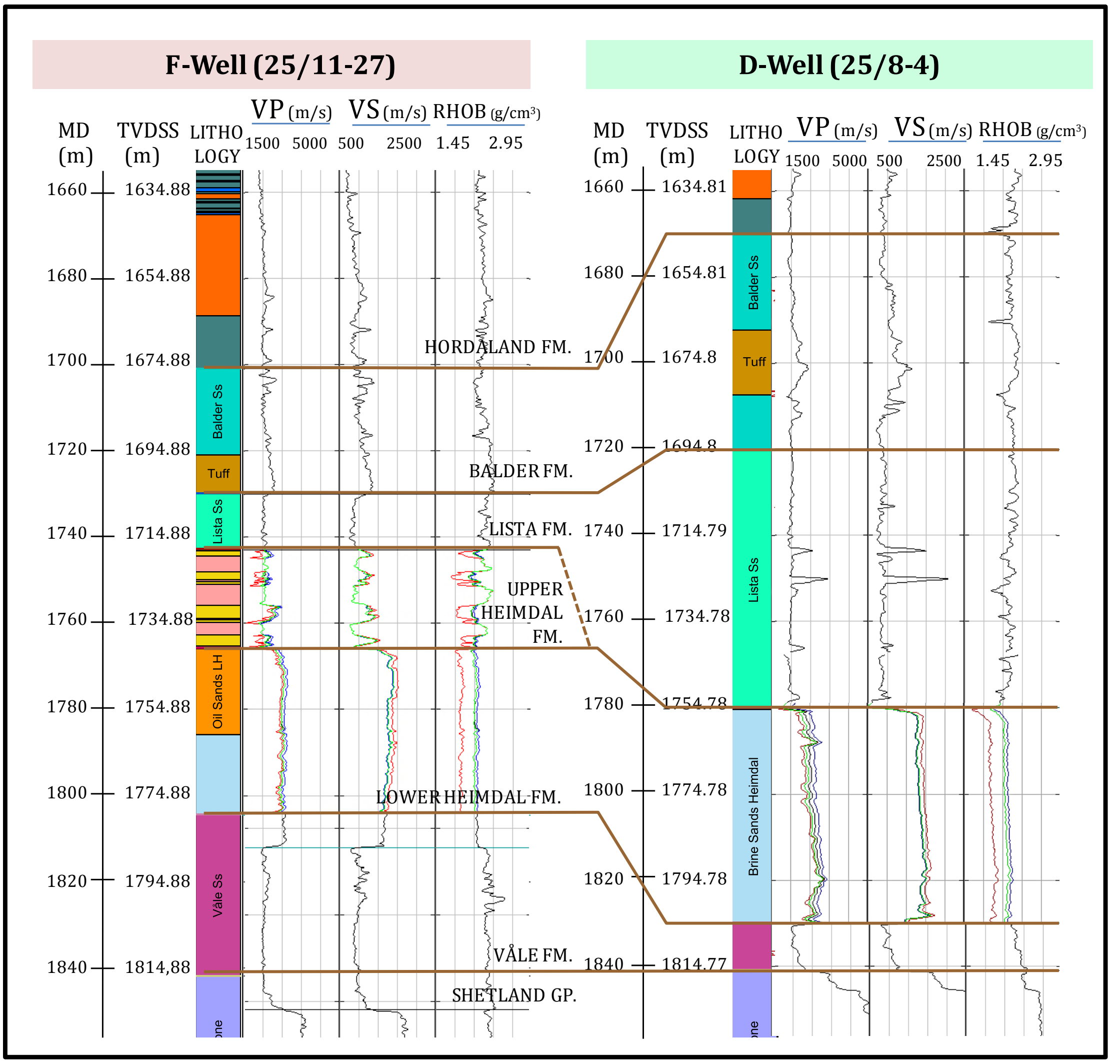

Figure 5.1 P-wave velocity, S-wave velocity and density log estimation using Gassmann substitution. Three cases are introduced, brine saturated (blue colored), oil saturated (green colored), and gas saturated (red colored). Study focus is constrained to the first two cases, brine and oil scenarios.

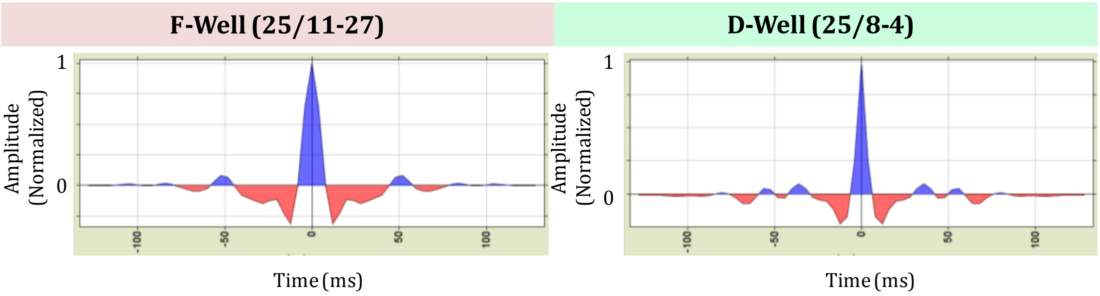

Figure 5.2 Extracted wavelet from near seismic trace for each well. Together with the derived Gassmann log value, the extracted wavelets are used to develop AVO model.

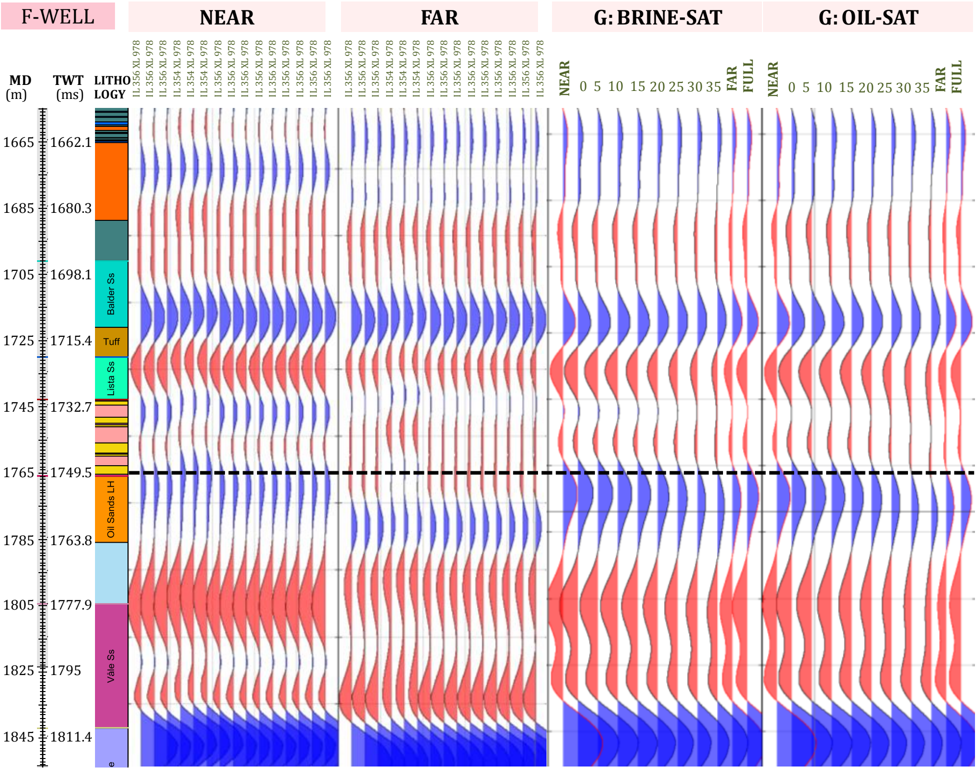

Figure 5.3 From left to right: Closest near and far seismic traces with respect to the F-Well, AVO model for brine-saturated case, AVO model for oil-saturated case.

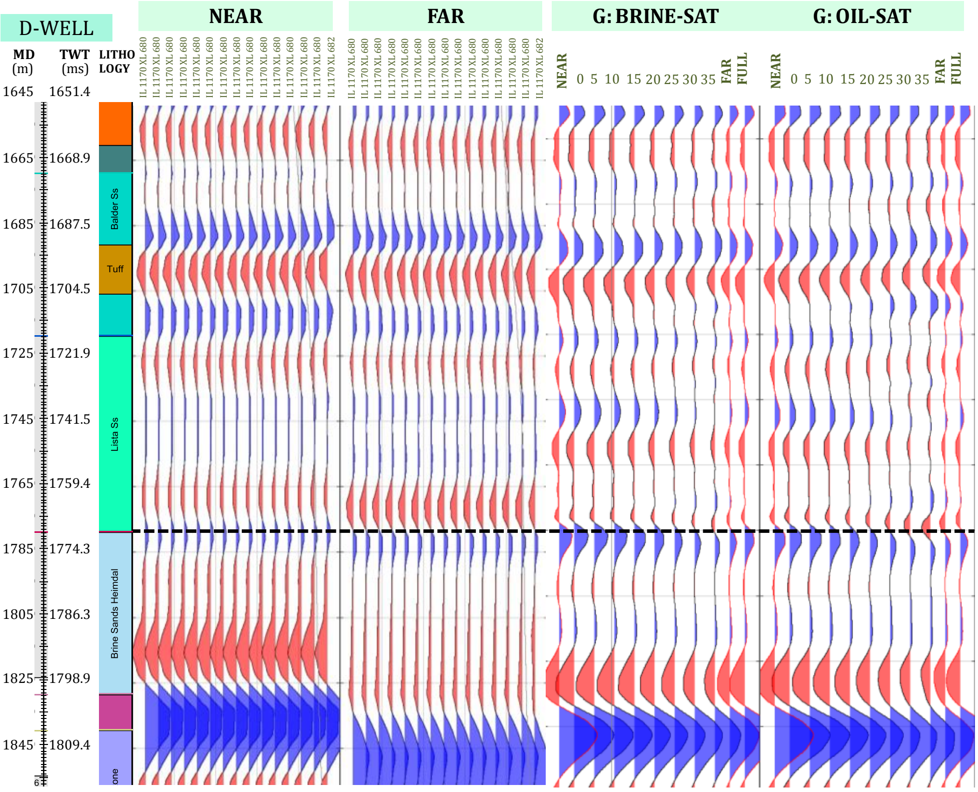

Figure 5.4 From left to right: Closest near and far seismic traces with respect to the D-Well, AVO model for brine-saturated case, AVO model for oil-saturated case.

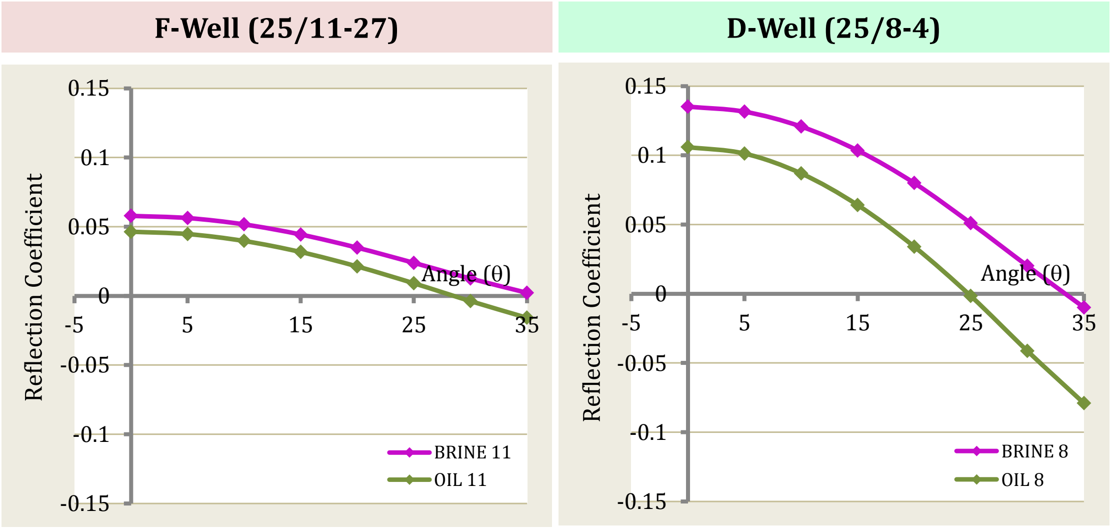

Figure 5.5 AVO crossplot across top Lower Heimdal formation given by Gassmann substitution for each well (black-dashed line at Figure 5.4)

In the near angle seismic and synthetic data, the amplitude of the top Lower Heimdal is shown as a peak of positive amplitude (Figure 5.3 and Figure 5.4). Compare to the D-well where the Lower Heimdal sandstones are mainly water-wet, with 17 meters of oil-wet formation within Lower Heimdal formation in F-well allows the amplitudes appear at higher value in near angle stack. At far stack, the amplitude of top Lower Heimdal in the real seismic is apparently different with the synthetics. In synthetics, the top of Lower Heimdal corresponds to zero-crossing (-/+) for both wells. Contrary, in the real seismic, the top of Lower Heimdal is characterized as negative amplitude at F-Well and zero–crossing (-/+) at D-Well. The overlying formation, Upper Heimdal formation is shown as poor seismic character. Such character is explained by the limited elastic parameters contrast between the sandstones and claystones, and the condition where the thickness of sandstones unit is below the seismic resolution. Moreover, it has been analyzed in previous chapter of how rock microstructure affects the elastic parameters. As elastic parameters provide a tight relationship with seismic signature, it is plausible to relate the low seismic amplitude character of Upper Heimdal as a signature of friable type sands.

Compare to the near seimic data, the far seismic data is more sensitive towards the pore-fluid changes. This presumption is taken as the amplitude of top Lower Heimdal in the F-Well and the D-Well appear more unlikely in far stack, rather than in near stack (Figure 5.3 and Figure 5.4). Gassmann substitution also confirms this observation. The reflection coefficient value gaps between oil-saturated and brine-saturated are greater in angle of 30^0 to 35^0 (Figure 5.5).

Using Gassmann substitution, it is interesting for one to understand the amplitude changes for different pore-fluid with function of angle. The reflectivity across the top of Lower Heimdal formation shows greater changes from near to far angle when oil predominantly fills the formation (Figure 5.5). When the Lower Heimdal sandstones are filled with oil, the decreasing amplitude is followed with changing the polarity of reflection coefficient at its maximum angle of 35^0. In terms of AVO, it is classified as Class IIp. The AVO Class IIp is a condition where the P-impedance of reservoir is higher than the overlying shale. Similarly, the P-impedance of reservoir for brine saturated is also higher than the overlying shale. However the value of P-impedance is lower when it is saturated with oil, producing a weaker contrast or reflection coefficient across the interface at zero offset.

The polarity reversal at the F-Well for brine case is absence at the maximum angle (Figure 5.5). In contrary, at the D-Well, polarity reversal is observed at the maximum angle. In terms of AVO, the brine saturated sandstones is classified with range from Class I to Class IIp.

What is interesting, using Gasmann substitution, the value of reflection coefficient at zero offset for brine and oil case is found to be higher at the D-Well (Figure 5.5). Contrary, in the near angle seismic data, the top of Lower Heimdal formation in the F-well is indicated with higher amplitude than in the D-Well (Figure 5.3 and Figure 5.4). One possible explanation is because the amplitude of top Lower Heimdal formation is not solely affected by the contrast of the interface itself. The oil-saturated Upper Heimdal formation that overlies the Lower Heimdal formation may produce such amplitude, which later interferes with reflection produced at top of Lower Heimdal sandstones. The superposition of amplitudes produces a peak reflection with wider time interval at near seismic data in the F-well. More extensive explanation regarding this assumption will be given in next chapter.

5.2 MULTIVARIATE STATISTICAL CLASSIFICATION

Implementation of Fuzzy Logic

Reservoir features such as lithofacies determination may establish by an explicit relation between log behavior and log data of those wells (Rezai and Mohaved, 2009). Like human do, a technique called fuzzy logic is built based on this need. Many random events fell into a pattern with a degree of regularity in the variation of an observation about its mean or average value (Rezai and Mohaved, 2009; Cuddy, 2000). These pattern usually represented by normal or Gaussian curves. Normal distribution is characterized by its mean and variance. The variance depends on the hidden factor and measurement errors, and equivalent to fuzziness or spread around the most probable value of occurrence or its mean (Rezai and Mohaved, 2009; Cuddy, 2000). Each lithofacies occurrence probability describes with fuzzy possibility of the most likely observation (Rezai and Mohaved, 2009). Fuzzy possibilities then compared between lithofacies, and therefore a relative occurrence of each lithology type can be controlled (Rezai and Mohaved, 2009). After the well log data inputted to the fuzzy logic system, the resulting model suggests that lithofacies as most probable lithofacies.

Lithology prediction based on fuzzy logic is established as an assertion that a particular lithofacies is characterized by certain value of log reading, and where some value will more likely than others (Cuddy, 2000). On this context, the main prediction system is aimed to identify formation lithology with varying depth, particularly to define intervals with hydrocarbon-wet. The training or the main input set is based on the F-well, given by the fact that the dataset of oil-saturated sands represented by more samples than the D-well. This action is needed to avoid any coherent statistical error, and the more excessive the sample the more equivalent the data distribution towards reality (Rezai and Mohaved, 2009). In predicting the lithofacies, the result is based on the if-then rules, with specific rule of weighting that is formulated by unique normal distribution features for each training data. There is no limitation in the number of input for each simulation, but for this study the number of input are constrained to be maximum 3 inputs. The training datasets, or the F-Well datasets, were used to construct the rule, while the test data, the D-well datasets, were used to validate the ability of the F-well performing lithofacies prediction. As the lithology of the test well was already known, this simulation will help to summarize the degree of similarity between the F-Well and the D-well and investigate the effectiveness of fuzzy system.

Cross-Validation of Training Dataset

Prior of lithofacies prediction of the D-well, it is important to perform cross-validation of various logs in the F-well. This operation is used to estimate the performance of a classifier by detecting bias tendencies in classification problem (Bosch et al, 2013). It is achieved by training the system by applying the prediction function that built from the training data into the same subset. Sets of input to predict the D-well lithofacies are then selected by the accuracy of cross-validation of various logs combination, ie. P-wave velocity, with S-wave velocity, density with gamma-ray, etc. The most optimal parameter combinations are then assigned for the D-well lithofacies prediction. Five major lithologies have been recognized from core studies, oil-saturated sands, brine-saturated sands, shaly sands, tuff, and limestones. For each lithology class, Gaussian function has been created by assuming a normal distribution of data. Data distribution of P-wave velocity, S-wave velocity and density for respective lithologies are given as examples (Figure 5.8 and Figure 5.9).

Twelve logs-combinations are proposed (Figure 5.6), where each combination of log data will correspond to a fitted model. Based on the twelve cross-validation performances, only five log-variations, Vs-RHOB, Vp-RHOB, Vp-Vs-RHOB, RHOB-SI, show good results in most cases. These five log-variations provide the highest match with the prior lithologies. The oil-saturated sand is very well estimated within the main reservoir interval (1730-1820 m MD). Meanwhile, at the depth less than 1730 m MD, the results are less conformable with the prior lithologies. This event is possible to occur when the density probability of oil-saturated sands is overlapping with shaly-sand lithology (Figure 5.8 and Figure 5.9). Here, the degree of separation between oil-saturated sands and shaly-sands is higher in S-wave velocity compare to the other variable.

The degree of sensitivity for each parameter towards lithology variation can be evaluated as combination of fuzzy logic results (Figure 5.6) with log-data distributions (Figure 5.8 and Figure 5.9). Using this approach, the density and the P-wave velocity value are observed to be predominantly affected by the pore-fluid composition and the corresponding lithologies, while the S-wave value is predominantly affected by lithologies, ie. sand or shale. Therefore shaly sands and sands will be easier to be distinguished by using S-wave velocity. In addition, the pore-fluid saturation prediction is best defined by assigning density to the training data. A lesser overlapping value between oil-saturated sands and brine-saturated sands in density data compared to velocity and gamma-ray, will provide a good condition in discriminating oil or brine case.

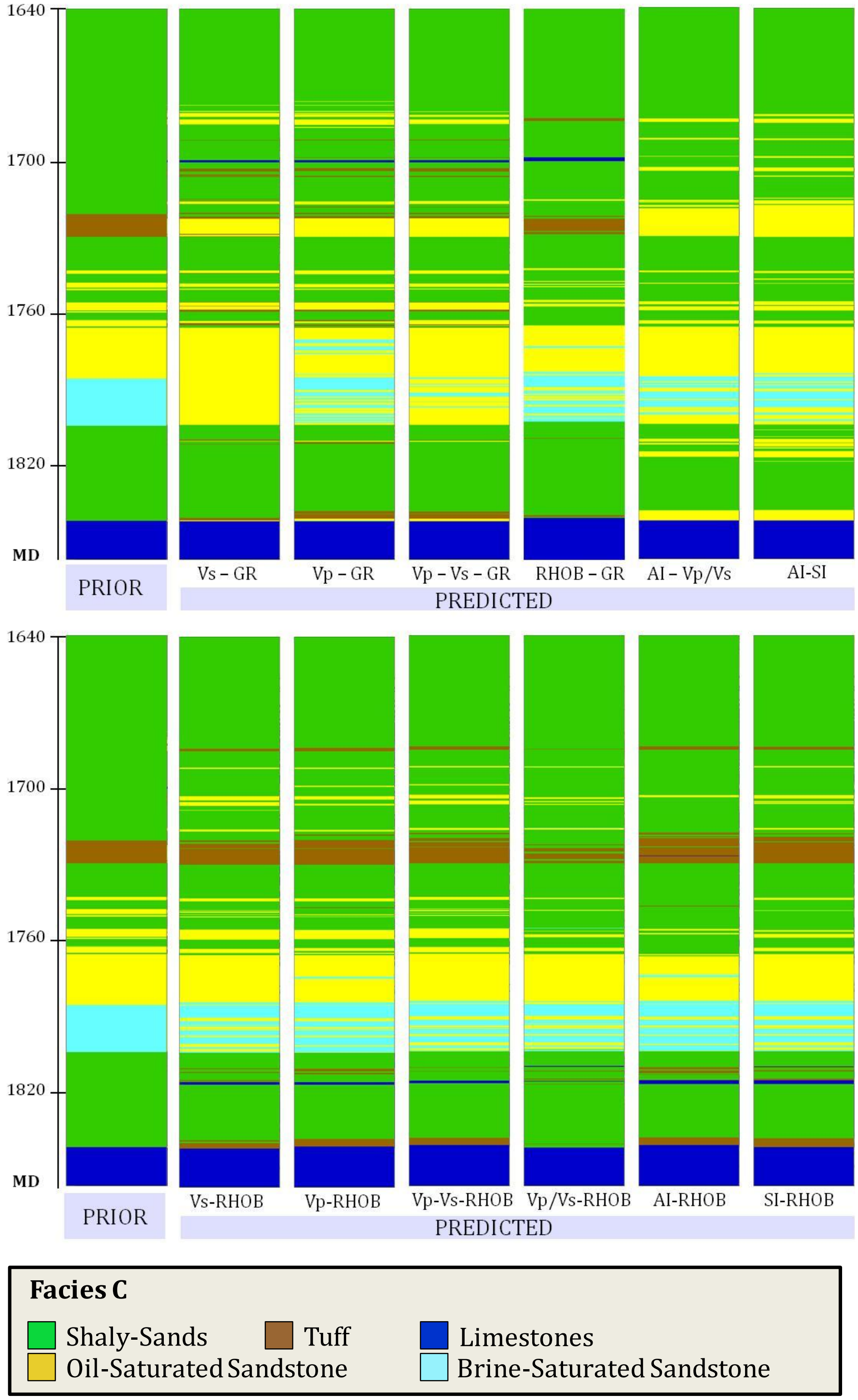

Figure 5.6 Cross validation result given by using the real or prior lithologies given by F-Well as training dataset. Twelve log-combinations are proposed.

Lithology Prediction

Five log-variations that have been proven to deliver good performances in cross-validation are then used to predict the lithofacies in the D-Well. In terms of predicting oil-sandstone lithofacies, all five set variations show high success rate (Figure 5.7). However, the rate for overall lithofacies prediction is low. The main reason is because the great degree of overlapping at velocity and density probability distribution (Figure 5.8 and Figure 5.9). In this case, overlapping is illustrated with limestones training data (F-Well) and brine-saturated sandstone test data (D-Well). Similar quality results are also shown when derivative variable of velocity and density are assigned as training data, ie. velocity-ratio, P-impedance and S-impedance.

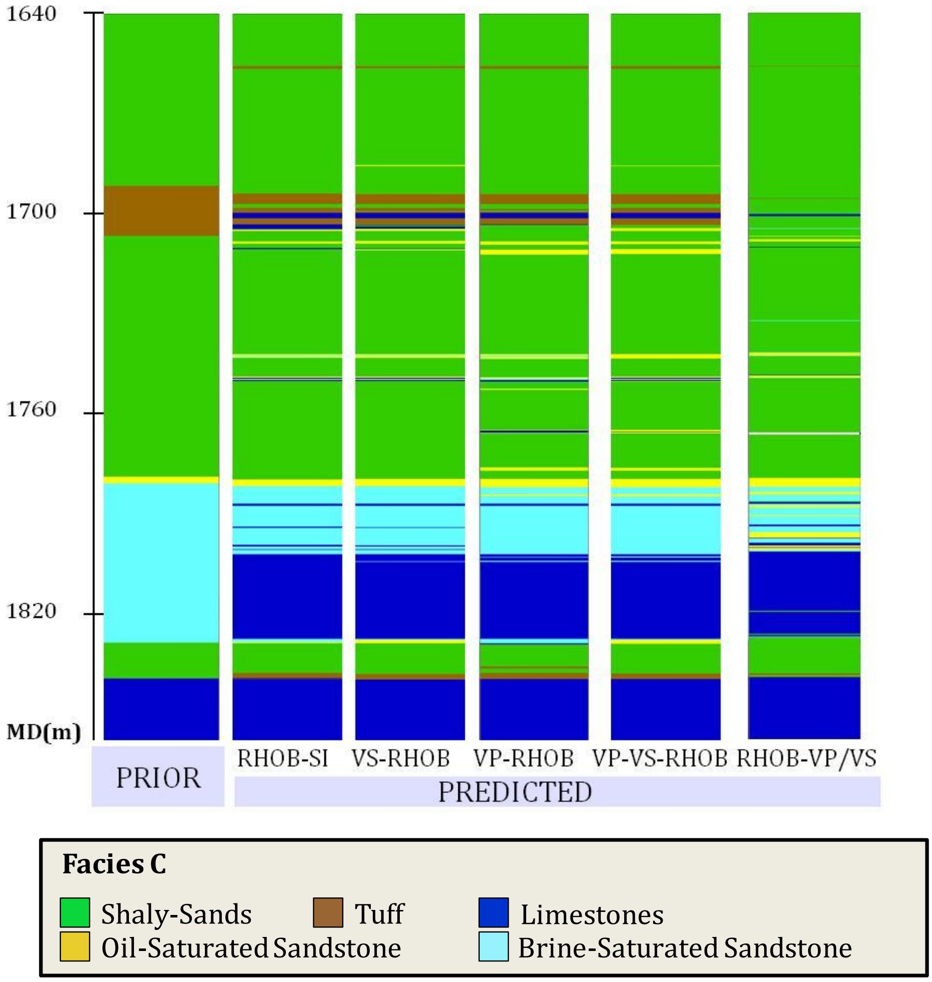

Figure 5.7 Lithology predicition on the D-Well by using the training set data of F-Well. Log-combinations are chosen by considering the cross-validation results in Figure 5.6. Five log-combinations are proposed.

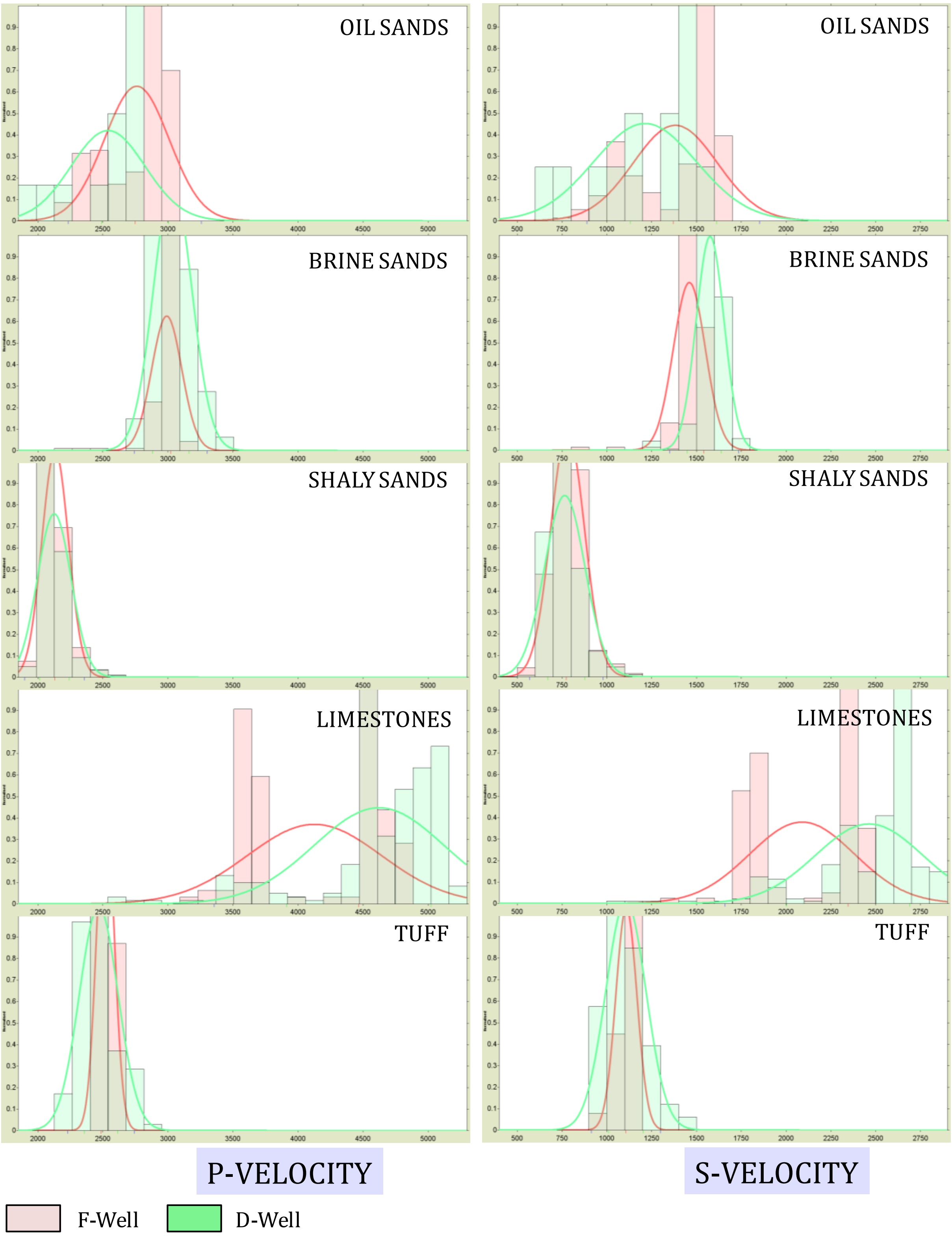

Figure 5.8 Normal distribution curve presents log-value distribution of P-wave velocity (left) and S-wave velocity (right) for different lithologies.

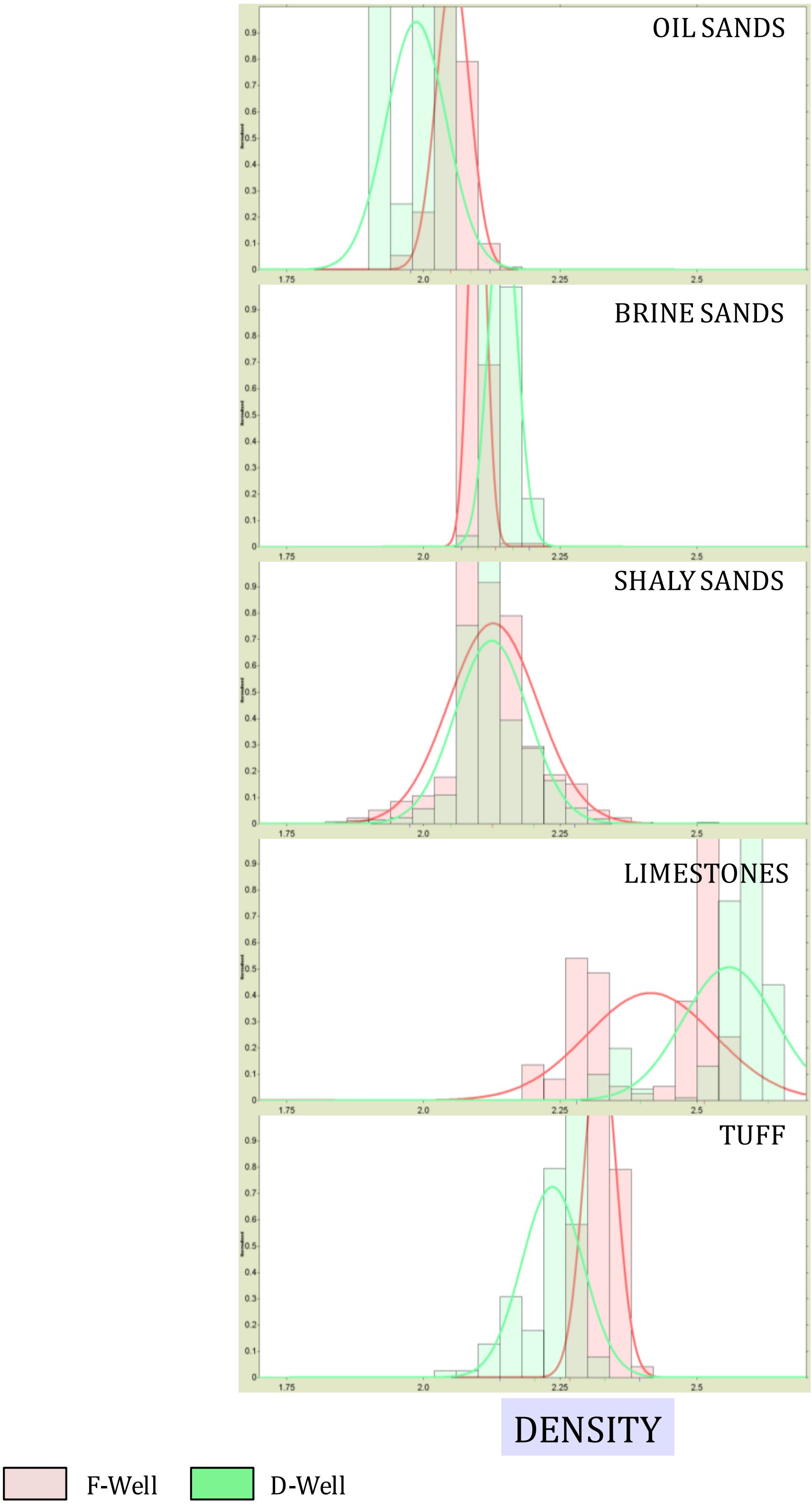

Figure 5.9 Normal distribution curve presents log-value distribution of density for different lithologies.

5.3 WELL – AVO MODELING

It is plausible to create such AVO response for different lithofacies combination by accessing uncertainties related to natural variation within each lithology (Avseth et al., 2001). The forward AVO analysis acts as guideline to predict the most likely lithology to occur at certain value of gradient and intercept derived from seismic data. The uncertainties are given by the probability density function (pdfs) of velocity and density (Figure 5.8 and Figure 5.9). Three main lithologies that play as important role in reservoir are chosen to be shaly-sands, brine-saturated sands, and oil-saturated sands. AVO response are then generated based on these combinations: (1) Shaly Sand – Shaly Sands, (2) Oil Sands – Shaly Sands, (3) Shaly Sands – Oil Sands, (4) Brine Sands – Shaly Sands, (5) Shaly Sands – Brine Sands, and (6) Oil Sands – Brine Sands.

The plot of AVO response is generated based on the mean value of velocity and density for each lithofacies respectively (Table 4 and Figure 5.10). For each interface category, the expected AVO response at target depth is calculated using Zoeppritz equation. The intercept or zero offset reflectivity, R(0), is controlled by contrast of acoustic impedance across the interface, while the gradient is controlled by contrast of velocity ratio or equivalently the Poisson's ratio (Rutherford and Williams, 1989; Ostrander, 1984; Avseth et al, 2001a, Avseth et al., 2001b; Avseth, 2010; Avseth et al., 2005). Using the mean value of velocity and density of brine sands and oil sands, the OWC or interface between oil and brine sands is also producing a seismic response. The response is represented as positive reflection coefficient for all given angles (Figure 5.10).

Bivariate pdfs of intercept and gradient are also generated (Figure 5.11). The distribution of intercept and gradient is calculated by using MonteCarlo simulation where the system will assign input of density and velocity value randomly for given two lithologies at each simulation (upper lithology and lower lithology). The simulation is built by honoring the correlation between three parameters, ie. P-wave velocity, S-wave velocity and density. The structure of covariance matrix determines the dependences between these three parameters (Avseth et al., 2003). The correlation of P- and S-wave velocity is higher than correlation between P-wave velocity and density, also correlation between S-wave velocity and density (Table 4).

The pdfs plots show intercept and gradient can vary for a given lithology combination (Figure 5.11). The top sands or shaly-sands and sands interface are distributed within fourth quadrant, while the bottom sands are within second quadrant. Considering the signature given by top sands, there is a probability of 100% chances of finding brine sands as Class 1 AVO in F-well and 98% chances at the same class in D-well. Meanwhile, there are only 80% chances to find oil sands as Class 1 AVO in F-well and 50% chances at the same class in D-well. The second most likely to find oil sand at the F-Well and the D-well is at Class IIp. The AVO model in Figure 5.11 shows a great degree of overlapping between oil-saturated and brine-saturated sands. The result suggests that analyzing the degree of deviation of brine and oil sands from zero-value is effective to discriminate these two lithologies, ie. AVO strength. From Figure 5.11, it is also interesting to observe that the interface for the same lithology, shaly-sands, may cause a seismic response by changing the properties of intercept and gradient.

F-WELL (25/11-27)									
LITHOLOGY	MEAN			STANDARD DEVIATION			CORRELATION		
	Vp	Vs	Rho	Vp Std Dev	Vs StdDev	RhoStdDev	Vp-Vs	Vp-Rho	Vs-Rho
BRINE SANDS	2991.0119	1460.0840	2.0985	115.7750	89.1813	0.0161	0.8756	-0.3278	-0.2518
SHALY SANDS	2133.2347	781.1510	2.1275	102.2574	93.4573	0.0814	0.7950	0.5060	0.1880
OIL SAND	2760.9143	1381.8197	2.0539	248.9101	234.5807	0.0306	0.9132	0.3484	0.3009
D-WELL (25/8-4)									
LITHOLOGY	MEAN			STANDARD DEVIATION			CORRELATION		
	Vp	Vs	Rho	Vp Std Dev	Vs StdDev	RhoStdDev	Vp-Vs	Vp-Rho	Vs-Rho
BRINE SANDS	2125.71	765.55	2.12	129.68	112.72	0.07	0.81	0.34	0.26
SHALY SANDS	3036.10	1575.70	2.15	147.03	77.84	0.03	0.63	0.88	0.74
OIL SAND	2539.62	1213.15	1.99	284.33	287.18	0.06	0.90	0.88	0.96

Table 4. Mean, standard deviation, and correlation as properties of normal distribution of P- and S-wave velocity, and density are given for each well.

In Figure 5.11, the AVO response of oil-saturated sands that is overlied by shaly-sand is shown as different characters for each well respectively. The gradient and the intercept of this lithofacies interface appear closer towards zero-value in the D-well. Such event of lacking data point set for building Gaussian curves on the D-well may cause statistically error during computation, and therefore it does not provide a right AVO response at shaly sands and oil-saturated sands interface case. Due to this reason, simulation given by the F-Well is thought to be most relevant to provide general information regarding the distribution of AVO response. In summary, observation given by AVO response of F-Well (Figure 5.11) shows that with almost the same intercept value, the degree of absolute gradient for interface of shaly-sand and oil-saturated sand case is higher compared to the shaly-sand and brine-saturated sand case. This observation is thought to be valid as it is found to be coherent with the previous Gassmann observation. Moreover, as the previous Gassmann sub-chapter observation, plot given by F-Well (Figure 5.11) shows that the gradient provides greater sensitivity than intercept to distinguish the most likely pore-fluid.

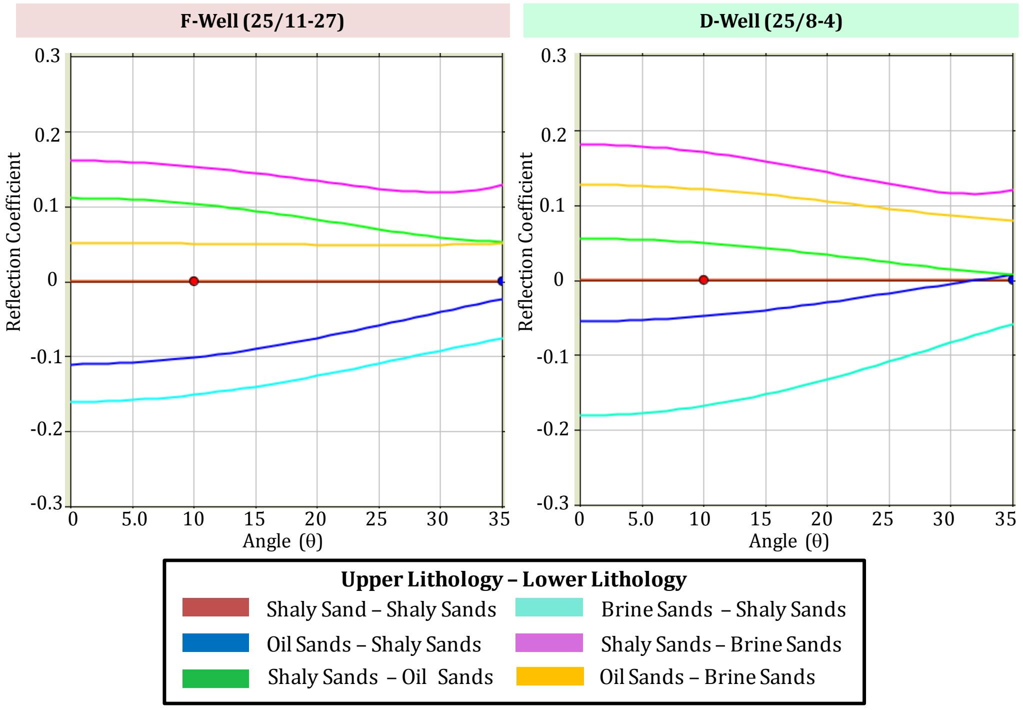

Figure 5.10 AVO model based on mean value of velocity and density for each lithology.

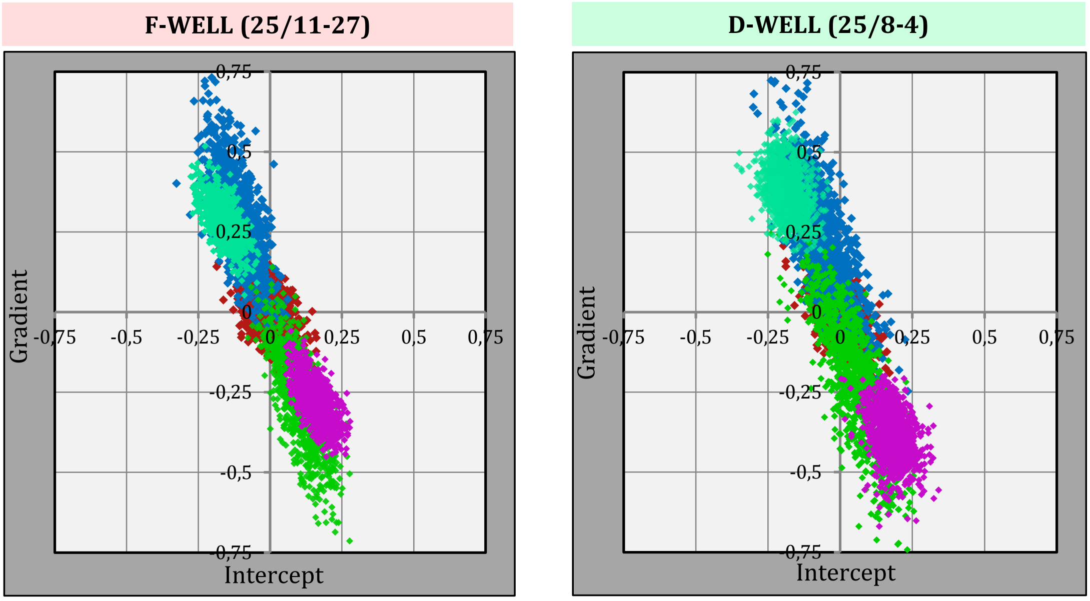

Figure 5.11 AVO model based on Monte Carlo simulation using normal distribution model for each lithology.

CHAPTER 6.

POST-STACK SEISMIC ANALYSIS

6.1 COMPREHENSIVE SEISMIC DATA DESCRIPTION

Two sets of seismic data and two main well, F-Well and D-Well, are used for providing main information within this study (Figure 6.1). One well called Nanna-Well is also used. The purpose of using the Nanna-Well is for blind-test or to validate interpretations. The seismic data consists of partial angle-stacks, near and far, with angle of stacks 5-15 degrees for the near angle stack and 25-35 degrees for the far offset stack (Figure 6.2 and Figure 6.3). The seismic data include the F- and D- structures in the Grane area.

From investigation on the seismic data, the Lower Heimdal sands are not easy to recognize. The top Balder is also hard to identify since no clear indications of elastic change. It is easier for interpreter to identify the base of Balder Formation, as the transition of tuffaceous unit to shaly unit yield strong impedance contrast. Therefore it is suggested to use this feature for characterizing the top of seal unit for the Lower Heimdal reservoir. The top of Lower Heimdal sandstones is shown as low-positive amplitude in near stacks and experiences amplitude decrement at far stack. In far stack, the top of Lower Heimdal sandstones appears as low-negative amplitude in the F-well, while in the D-well it appears as zero crossing -/+.

From Rock Physics to Seismic Character

Based on RPT model, it had been investigated in Chapter 4 that unconsolidated sands model fits the Upper Heimdal, while the Lower Heimdal is fitted with cemented sands model (Figure 4.9 and Figure 4.10). Observation shows that the Lower Heimdal formation in the D-well has higher amount of cement than the F-well. Suitable RPT models suggest that the F-Well is properly modelled with 4% calcite cement F-well, while D-well with 5% siliclastic cement (Figure 4.11). Moreover in Chapter 5, feasibility analysis also suggests that the pore-fluid type in sandstones will also influence the impedance (Figure 5.5 and Figure 5.10). The impedance of brine saturated sands is higher than the oil saturated sands. Ideally, with higher degree of cementation and higher brine saturation at the D-well, the contrast of acoustic impedance at the top of Lower Heimdal sandstones will be stronger in the D-Well rather than in the F-Well. With stronger impedance contrast it is expected that at the near stack, the amplitude across the top of Lower Heimdal sandstones at the D-Well is stronger than the F-well.

However, it is interesting to denote that the real seismic confirms the contrary. The plausible reasons will be explained after, but in terms of rock physics, it can be summarized that a 1% difference of cementation between the D-Well and the F-Well seems not provide a great effect in giving a notable difference in seismic signatures of top Lower Heimdal. In this study, relationship between rock physics and seismic signature is only valid to identify the sandstones microstructure, ie. to distinguish cemented sands from unconsolidated sands. Such example is demonstrated by observing the difference of the Lower Heimdal and the Upper Heimdal sandstones microstructures. Compare to the Lower Heimdal sandstones, the injectite Upper Heimdal sandstones has lower P-impedance and higher velocity-ratio (Vp/Vs) in the F-well due to the absence of cementation (Figure 6.2). With nearly same porosity value given by the Upper Heimdal and the Lower Heimdal sandstones, each formation presents as a different seismic character. The Upper Heimdal sands appear relatively dimmer than Lower Heimdal sands.

Pore-fluids, Seismic Resolutions and their Seismic Characters

The Lower Heimdal sands show that increasing oil saturation will increase S-velocity and slightly lowering P-velocity (Figure 4.13, Figure 6.2 and Figure 6.3). Since the density also decreases with increasing oil saturation, the acoustic impedance of oil saturated sandstone is lower than brine sandstones. Previous models in Chapter 5 show that the common response within shaly sands and brine-sandstones interface gives higher reflection contrast rather than the shaly-sands and oil-sandstones interface (Figure 5.5 and Figure 5.10). Moreover, for a shaly-sands and brine/oil sandstone interface, the decrement of amplitude relative to the increasing angle is more obvious at the top of oil-sandstones rather than the top of brine-sandstones. This is due to the Vp/Vs of oil sandstones is relatively lower than brine sandstones (Figure 4.11).

In the near seismic stack, the top of Lower Heimdal sandstones at the F-well with 17 meters oil bearing is denoted with higher amplitude than the top of Lower Heimdal sandstones at the D-well (Figure 6.2 and Figure 6.3). Observation in real seismic gives a contrary argument to previous statement as the top oil-saturated sandstones are not indicated by lower amplitude than brine-saturated sandstones. This condition may be due to the interference. Interference or tuning effects happened if there are reflectors in closely spaced are unable to be identified as separate event as product of wave superposition. Here, two different scenarios of interferences are proposed.

In the first scenario, the interference is a product of reflector superposition of (a) and (b), where:

(a) Reflection as function of interface between shaly-sands and oil-sands
(b) Reflection as function of interface between oil-sandstones and brine-sandstones (OWC).

From the result of AVO modeling at Chapter 5, it is known that each reflector of (a) and (b) is characterized by a different seismic character (Figure 5.10). For interface of (a), R(0) is given by low positive amplitude and the amplitude reduces with increasing angle. The (b) interface will produce positive R(0), which value is higher than (a), and the amplitude reduces with increasing angle (Figure 5.10). Superposition of these two reflectors at the F-Well would enhance the amplitude and expand the period of amplitude wavelength at the top oil-sandstones at near angle seismic stack (Figure 6.2).

In the second scenario, the interference is occurred between:

(a) Reflection as function of shaly-sands and Upper Heimdal sands interface
(b) Reflection as function of shaly-sands and Lower Heimdal sands interface

The Upper Heimdal sandstones appear as intercalation of sandstones and shaly-sands, where the thickness for sand unit is less than 10 meters. With a significant change of lithology below seismic resolution, the amplitude will interfere, and affecting the Lower Heimdal seismic signature. The superposition of positive reflection at zero offset for both (a) and (b) creates stronger amplitude value in the top of Lower Heimdal formation at the F-Well. With higher separation of injectite sandstones and Lower Heimdal at the D-Well, reflection for each interface does not interfere.

In general, difficulty in detecting Lower Heimdal formation is particularly due to the low acoustic impedance contrast. This condition is deteriorated with the possibility of frequency-dependent attenuation to occur. The tuff lithology that overlies the Lower Heimdal sandstones around 60-80 meters upward the reservoir may allow the high-frequency seismic energy to be attenuated rapidly as the contrast across the top tuff is notably high. The preferential of high frequencies absorption across this interface may analogue with the quality reduction of the top Lower Heimdal reflector.

The quality of interpretation

Interpretation of Lower Heimdal at a “blind-test” well called the Nanna-Well is now introduced. By using the seismic signature of Lower Heimdal sandstones given by the F-Well and the D-Well (Figure 6.2 and Figure 6.3), the presence of the Lower

Heimdal sandstones is predicted within the Nanna-Well (Figure 6.4). In the Nanna-Well, it is assumed that the base Balder Formation is known at 1764 ms. An interesting reflector at the near seismic stack around the Nanna-Well presents at 1773 ms as low positive amplitude, and is becoming more positive with increasing angle. However, this seismic signature is noted to be different with the seismic signature of the top of Lower Heimdal sandstones in the F-Well and the D-Well, since the amplitude is not decreasing with increasing angle of offset. By adopting this observation, the probability in finding oil-saturated sandstones at Nanna-Well is small. As the real observation confirms that there are no sandstones encountered at this well, it is summarized that a combined interpretation of near and far angle stack is adequate for the top Lower Heimdal prediction.

Interpretation using near or far stack alone is not suggested, as the quality of interpretation is fair. In the Nanna-Well, the reflector on depth of 1773 ms at the near stack may correspond to interpretation of top Lower Heimdal sandstones as its character is similar with the character of top of Lower Heimdal sandstones in the F-Well and the D-Well (Figure 6.2, Figure 6.3, and Figure 6.4). In terms of fluid sensitivity, the far angle seismic stack seems to correspond more than the near stack. The top of oil-saturated sandstones in the F-Well is characterized by lower amplitude than the top of brine-saturated sandstones in the D-Well. This observation will be confirmed in Chapter 6.2.3.

The seismic-to-well calibration is also performed to model the seismic response. The objective is to tie the well information to the seismic data based on time domain. Unique wavelets are extracted within the seismic trace closest to the position of the borehole trajectory (Figure 6.5). The associated synthetic by using respective wavelet provides good correlation with seismic data (Figure 6.2 and Figure 6.3).

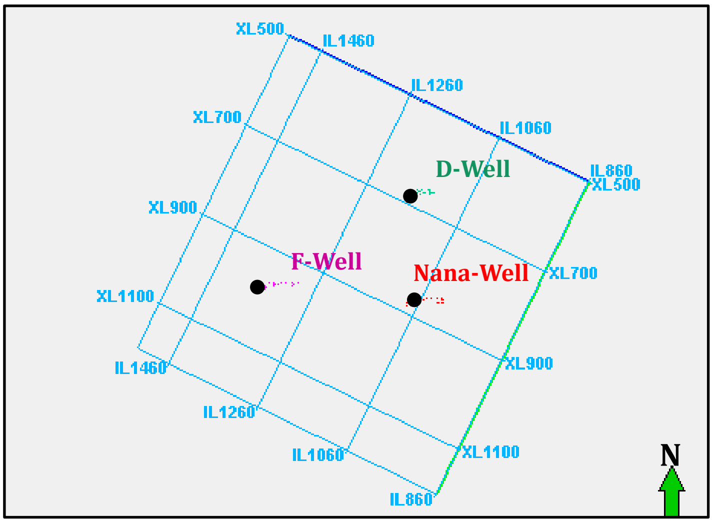

Figure 6.1 The seismic basemap and location of F-Well, D-Well and Nanna-Well.

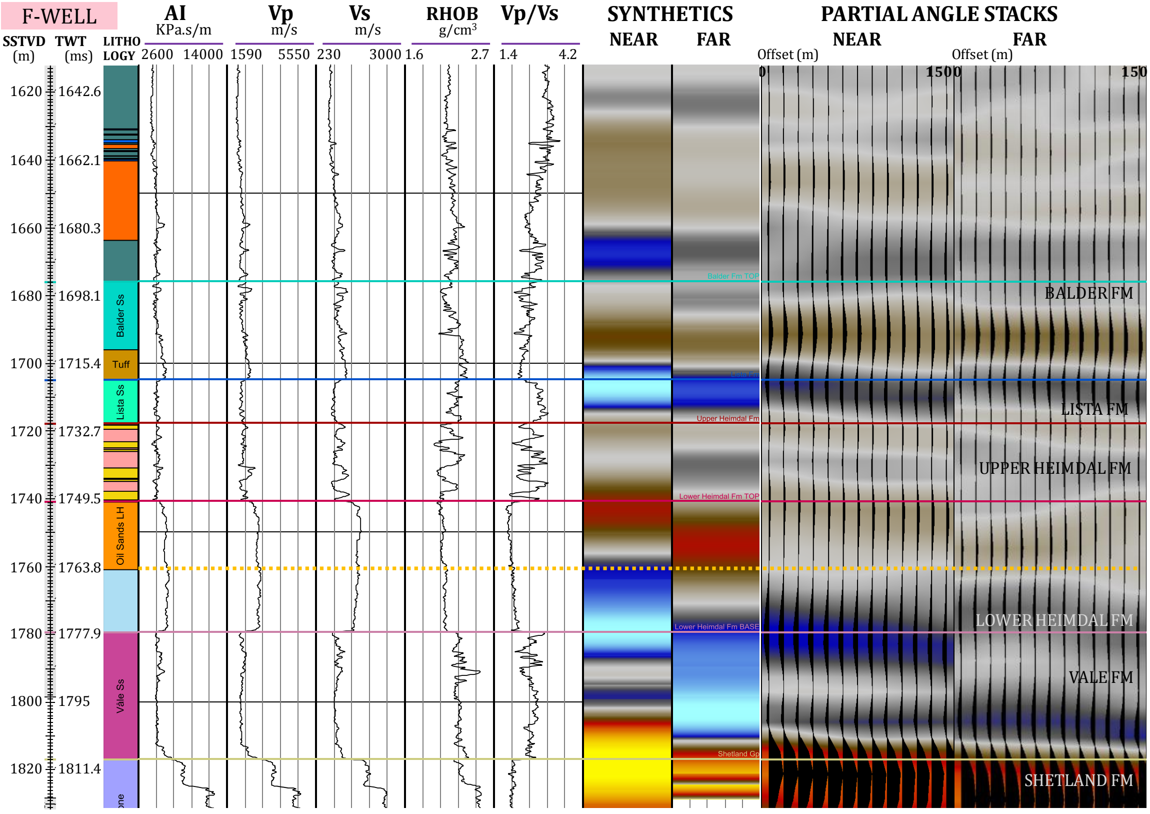

Figure 6.2 Main log information, synthetics and near-far angle seismic stack of F-Well.

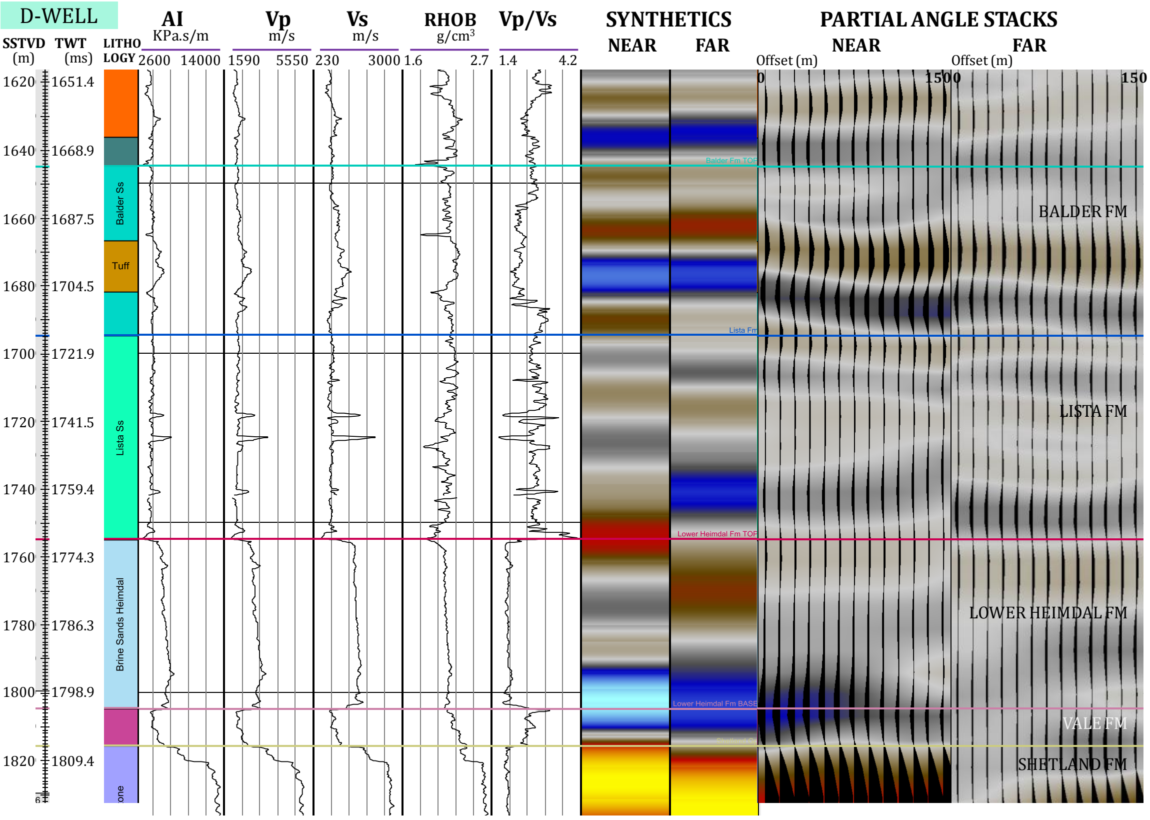

Figure 6.3 Main log information, synthetics and near-far angle seismic stack of D-Well.

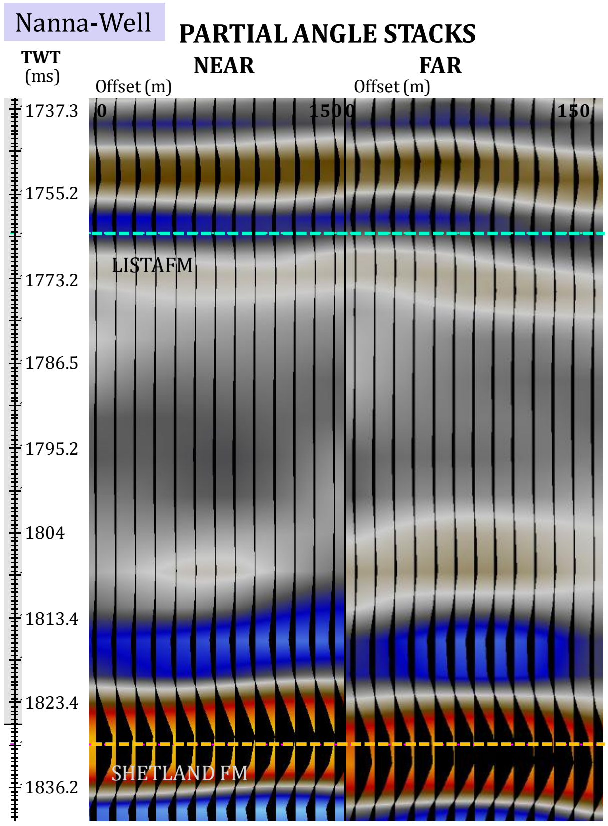

Figure 6.4 Near-far angle seismic stack of Nanna-Well.

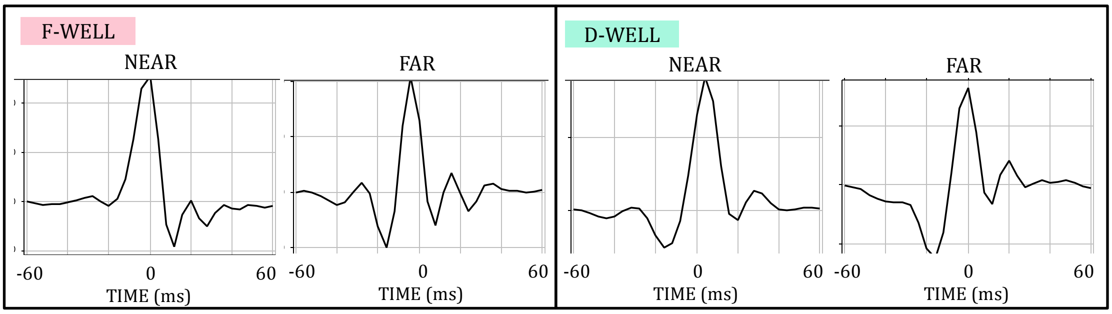

Figure 6.5 Wavelet estimation for synthetic seismic modeling for F-Well and D-Well in Figure 6.2 and Figure 6.3.

6.2 PRE-INVERSION

As acoustic impedance (AI) can be estimated in well log data, impedance that is equivalent to gradient called gradient impedance (GI) can also be produced with formula given by Whitcombe et al., 2002 (Connolly, 2010). By combining AI and GI, coordinate rotation can be applied to produce a new log series. This method, called EEI, is implemented as rotation within impedance function. EEI operations can also be applied in seismic data to construct a new dataset which correlate to certain log response. Since the certain log responses are sensitive towards lithology and pore-fluid change (Chapter 5), application of EEI will then help to optimize the separation of lithology and pore-fluid. In seismic, the EEI can be applied in reflectivity domain, involving intercept and gradient datasets, and also in impedance domain, involving the inversion process. In this chapter, the EEI focus on the reflectivity domain and therefore no inversion process is required.

6.2.1 EEI PETROPHYSICAL ANALYSIS

At a certain angle chi (χ), the derived EEI log series gives maximum correlation with certain log sets, ie. density, gamma-ray, etc. The correlations measure the effectiveness of EEI approximation of certain log curves.

At a different optimum angle χ, density, P-wave and S-wave velocity, and also velocity-ratio (Vp/Vs) are very well estimated (Table 5). Combination of AI and GI produces EEI series that has correlation coefficient of 1 (or almost 1) with the log sets. An example for the P-wave velocity log which can be sufficiently estimated by projection of AI-GI at $\chi=-20^0$, with correlation around 0.985 (Table 5 and Figure 6.6).

Previous observations in Chapter 5.2 show that the density is more effective in predicting pore-fluid than the other log sets. In lithology classification, S-wave velocity (Vs) excels from other parameter, ie. gamma-ray (GR) and velocity-ratio (Vp/Vs). Meanwhile, P-wave velocity (Vp) shows good performance in lithology and pore-fluid classification, where it is mainly sensitive to lithology changes. Insufficient correlations of EEI (less than 0.8) at certain parameters show that the affiliated reservoir parameters are hard to be identified using EEI impedance projection (Table 5). Therefore gamma-ray and porosity-effective will be excluded from ensuing issues of EEI, similarly with

Vp/Vs which had been previously analyzed to be not optimal in lithology/pore-fluid prediction (Chapter 5.2).

Using these information, it is presumed around angle on which density is projected (χ=14^0) within impedance domain, will correspond to pore-fluid separation. Similarly, at which Vp and Vs are projected (χ=-20^0 to -50^0), will be subjected to lithology separation, but also potentially to pore fluid separation as the Vp is proven to be a good pore-fluid discriminator.

According to Whitcombe et al. (2002) and Connolly (2010), the subsurface reflection with incidence angle of 30^0 is equivalent to a chi angle (χ) of 15^0 (which is analogue to given case of χ=14^0 as well), are close to fluid projection angle. Therefore, the far angle stack seismic (25-35 degrees) contains more information regarding pore-fluid separation than the near angle stack seismic (5-15 degrees). Later, this argument is supported by the result of EEI implementation at fluid-projection angle which produce a character that corresponds to far angle stack (Chapter 6.2.3).

As the lithology projection is relatively close to the gradient projection, the gradient stack will represent the lithology projection (Conolly, 2010). However, pore-fluid may also still have some influences, even not as substantial as the lithology change. In Chapter 6.2.3, one may observe that the gradient volumes provides as an effective tools for lithology and pore-fluid prediction.

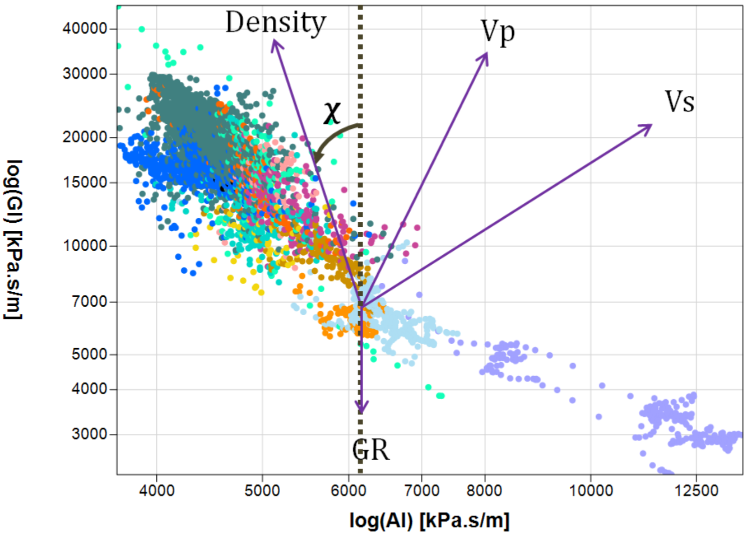

Figure 6.6 The angle χ in log GI-AI crossplot associates with certain log response and projection. Lithology projection is represented by S-wave velocity (Vs) and gamma ray (GR). P-wave velocity (Vp) represents combination of lithology and fluid projection, while density represents the fluid projection.

Eventhough the EEI log series show good similarity with well log curves, the optimum angle of petrophysical analysis does not always precisely similar with the angle given by EEI rotation in seismic data. The petrophysical analysis act as feasibility studies to give an idea of where to look, and what geological observation that is expected to be encountered at associated angle (Connolly, 2010). Systematic errors in seismic data such as noise, anisotropy effect and pre-stack scaling are probably the main reason of the angle difference with the log data.

EEI	χ	CORRELATION		Dominant Sensitivity
		F-Well	D-Well	
GAMMA-RAY (GR)	180	0.63	0.77	Lithology (Shaly-Sand/Sand)
DENSITY	14	0.8	0.9	Pore-Fluid (Brine/Oil Saturated Sand)
P-WAVE VELOCITY	-20	0.98	0.99	Lithology and Pore-Fluid (Shaly-Sand/Brine Saturated Sand/Oil Saturated Sand)
S-WAVE VELOCITY	-50	0.97	0.98	Lithology (Shaly-Sand/Sand)
PHIE	-152	0.55	0.48	Lithology (Shaly-Sand/Sand)
VEL. RATIO (Vp/Vs)	42	1	1	Lithology (Shaly-Sand/Sand)

Table 5. The highlighted red parameters are not considered to the low correlation between the derived EEI logs with the affiliated log data. The blue parameters are also not considered due the unsatisfactory performance of the parameters in lithology and fluid prediction in feasibility studies.

6.2.2 INTERCEPT-GRADIENT ANALYSIS

To deliver a good representative of true AVO effects, near and far seismic stacks are needed to be balanced correctly, and the horizons are appropriately time-aligned (Avseth et al., 2005). The time aligning procedures has been performed within previous Statoil's internal work and confirmed by Figure 6.7 where the near and the far stack are properly balanced. Seismic partial stacks also need to have same phase and polarity (Kemper et al., 2010). This includes zero phasing of near angle stack and spectral balancing the far angle stack. The zero phasing implementation at the near stack has been confirmed within the previous synthetic modeling, on which wavelets are close to the zero phase (Figure 6.5). The frequency of the far angle seismic stack had also been balanced correctly, as the frequency character of the far stack is equivalently similar with the near angle seismic stack (Figure 6.8). Using the near and far stack, intercept and gradient volumes are generated to enhance the confidence in reservoir interpretation. The intercept volumes are equally the same with the near stack, while the gradient volume is produced as subtraction between far and near angle stack data.

The quality of interpretation

In the intercept seismic profiles, it had been investigated that the top of Upper and Lower Heimdal sands are associated with the low positive amplitude. In gradient volumes, the top of Lower Heimdal sands has higher negative value in the F-well which corresponds to the top of oil-sandstones. On that case, lower negative value in D-well will correspond to the top of brine-sandstones. Prior investigation shows that pore-fluid of Heimdal sandstones has strong relation with certain AVO behavior. Since the gradient across the top of oil-bearing sandstones is higher than brine-saturated sandstones (Chapter 5), the top of saturated oil-sandstones of Lower Heimdal will most likely defined as Class IIp. A more extensive explanation is discussed on the next chapter.

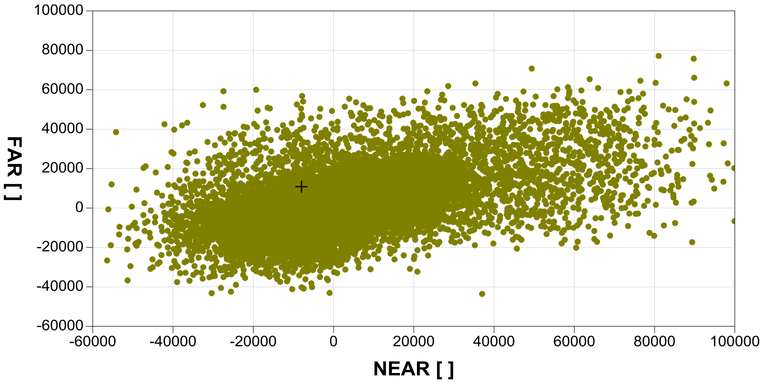

Figure 6.7 Amplitude value given by near and far angle seismic stack in a crossplot.

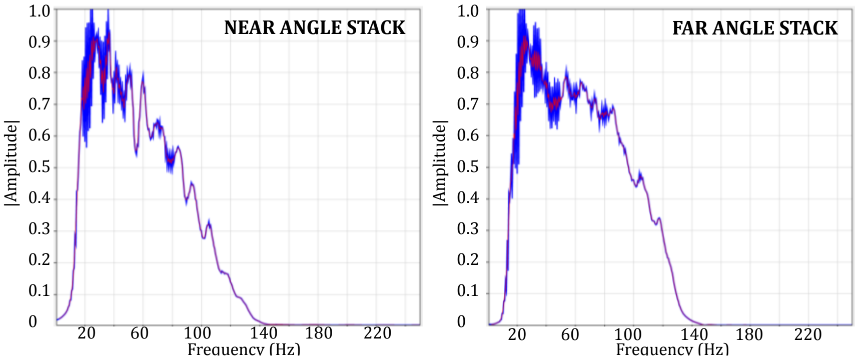

Figure 6.8 The average seismic spectrum from near angle seismic stack (left) and far angle seismic stack (right).

With the good ability of gradient to indicate the pore-fluid, it summarizes that far angle seismic stack plays as an important variable to determine hydrocarbon bearing zones. This statement is supported by the fact that the top of Lower Heimdal formation at intercept volumes are shown with nearly same value within the F-Well and the D-Well (Figure 6.9 and Figure 6.10). The values in the near stack are assumed to be predominantly affected by the lithology than pore-fluid properties.

The top Upper and Lower Heimdal formation that correspond to the top sands are given as low positive amplitude at the intercept and followed with low-to-strong negative amplitude at the gradient (Figure 6.9 and Figure 6.10). Such combination of intercept- gradient interpretation is implemented to predict the top sands in the Nanna-Well (Figure 6.11). Across the depth 1773.2 ms, the low positive amplitude at intercept is not followed with negative amplitude at the gradient. This observation draws a conclusion that there is no sandstones unit discovered within this well.

The quality of combined interpretation using intercept and gradient, or gradient alone is very good. Using the gradient, the bottom of Lower Heimdal sandstones is indicated by strong positive amplitudes. By knowing its top and bottom, it is possible to estimate the thickness of Lower Heimdal sands. However by only using intercept, the quality of top of Lower Heimdal interpretation is fair. An example is by the picking low positive amplitude as top of Upper and Lower Heimdal sandstones at the F-Well and the D-Well (Figure 6.9 and Figure 6.10). In the intercept cube of Nanna-Well, this signature will correspond to interpretation of top sandstones at 1773.2 ms (Figure 6.11). Since there was no sand encountered in Nanna-Well, using intercept alone as interpretation tool is therefore not suggested.

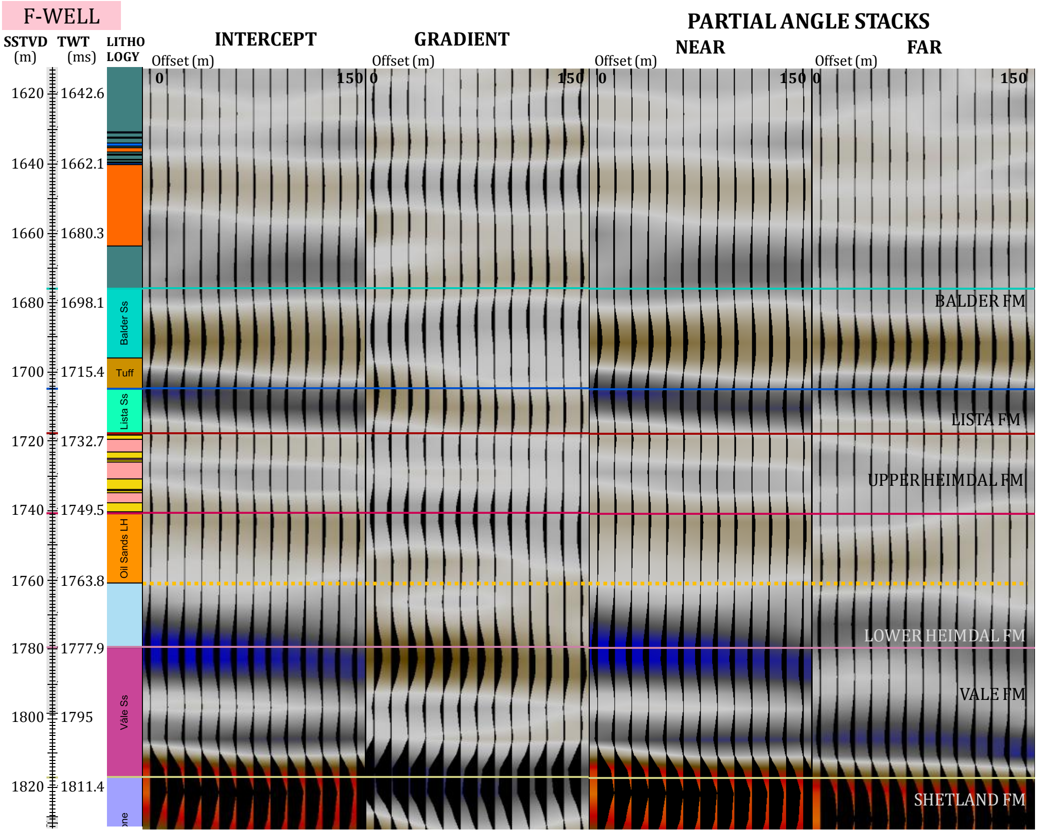

Figure 6.9 Intercept, gradient, and near-far angle seismic stack around the F-Well.

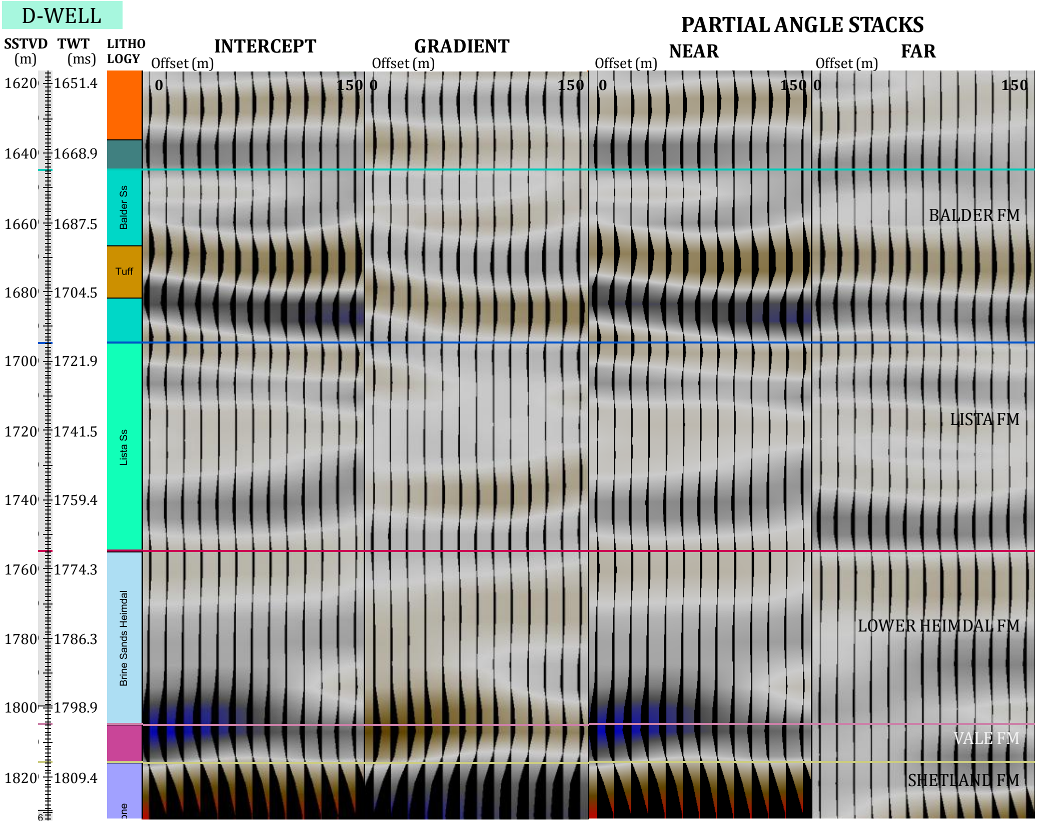

Figure 6.10 Intercept, gradient, and near-far angle seismic stack around the D-Well.

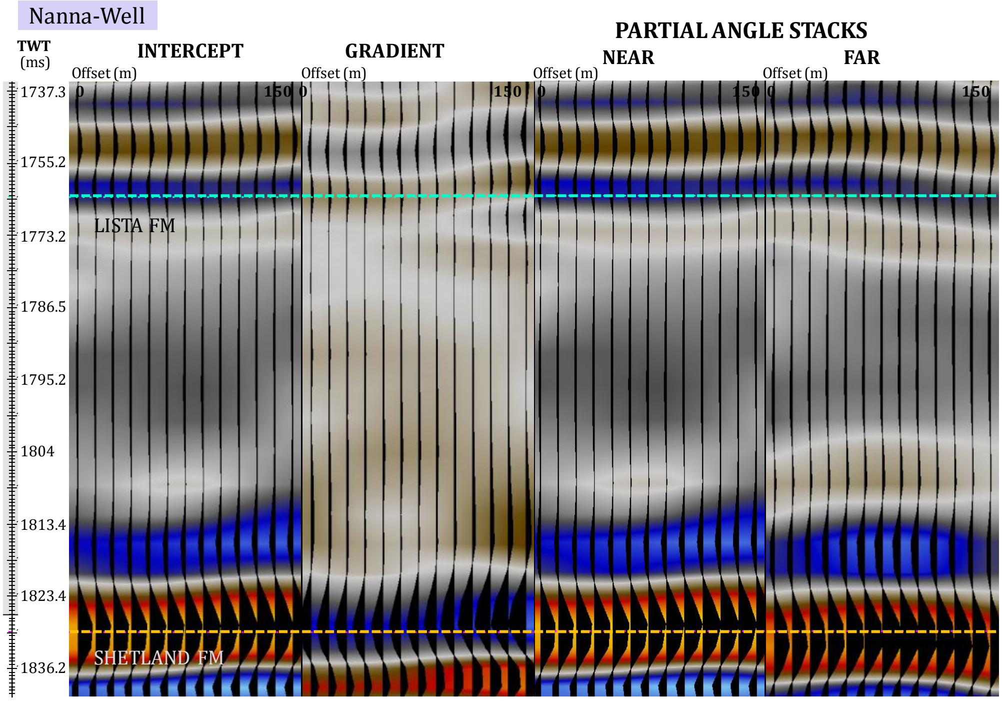

Figure 6.11 Intercept, gradient, and near-far angle seismic stack around the Nanna-Well.

6.2.3 INTERCEPT-GRADIENT ROTATION STACK (EEI REFLECTIVITY)

In some cases, intercept and gradient do not say much about the presence of hydrocarbons, combinations of them do. These combinations may enhance the lithology and fluid separation from the background trend. Stack is produced as combination of intercept and gradient stacks within an angle of rotation in the reflectivity domain without involving inversion process. This implementation process called as EEI reflectivity. The rotation is done locally within the reservoir area from thcaprock to base reservoir, or from the top Balder formation (approximately -20ms from base Balder) to the top Shetland formation. The interval boundary is aimed to enhance the sensitivity of reservoir unit regarding the changes of lithology and clay content, also to suppress the influence of some geologic factor related to increasing burial depth (Avseth et al., 2005).

There are two angles of rotation that are introduced, an angle nearly linear to the background trend, and an angle nearly perpendicular to the background trend (Figure 6.12). The amplitude strength of produced attribute can be envisaged as the distance of each sample point from the chosen angle rotation (Gidlow and Smith, 2003).

The quality of interpretation

Inspection within produced attribute using χ = 10 at the F-Well and the D-Well (Figure 6.13 and Figure 6.14), confirm that the top Lower Heimdal sands are located within -/+ zero crossing. Using this feature to interpret the top of Lower Heimdal at the Nanna-Well will lead to misinterpretation as the reflection feature at 1773.2 ms potentially picked as top sands while in reality there are no sands discovered. In terms of fluid identification, oil-water contact (OWC) is presented as a unique feature in the F-well. OWC appears as +/- zero crossing. However, OWC prediction by using this feature lead to ambiguity as the +/- zero crossing at the D-Well (1782 ms) does not correspond to OWC in reality.

The top of Upper and Lower Heimdal in χ = -23^0 volumes are identified as strong positive amplitude at the F-Well and D-Well (Figure 6.13 and Figure 6.14). Such strong feature is not seen within the Nanna-Well, leading to an assumption that there are no sandstones within this area (Figure 6.15). The intensity of amplitude may also help to identify the presence of hydrocarbons. The top of oil-bearing sandstones of Lower Heimdal appears with stronger positive amplitude than the top of brine-saturated sandstones (Figure 6.13 and Figure 6.14). This EEI reflectivity volume could be addressed for another interpretation purpose, such as estimation of sandstone thickness. Its thickness is equivalent to half-wavelength long, from positive peak amplitude (at top sand-bodies) to negative peak amplitude (at base sand-bodies).

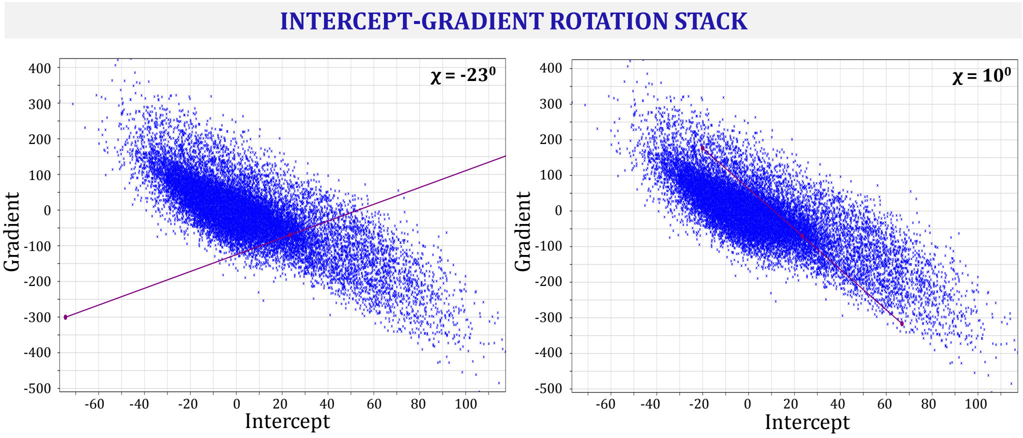

Figure 6.12 The angle of chi (χ) chosen to build the EEI reflectivity, χ = -23⁰ and χ = 10⁰.

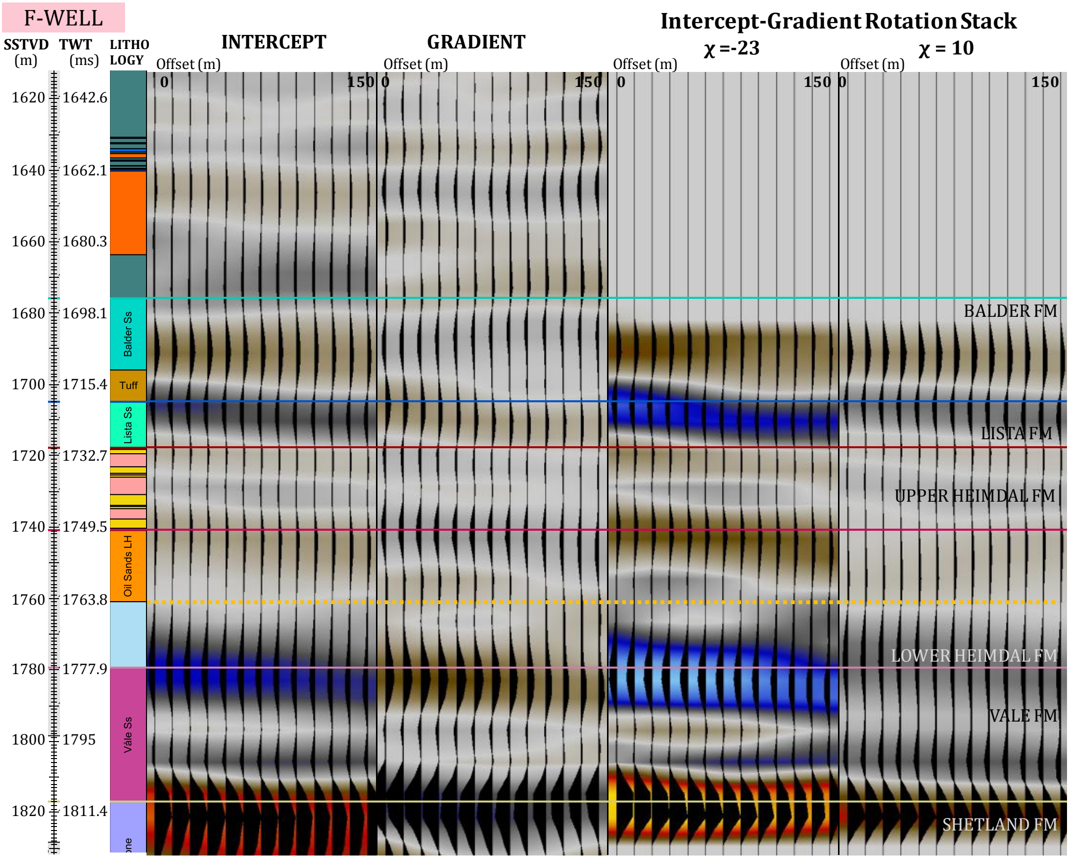

Figure 6.13 Intercept, gradient, EEI reflectivity of χ = -23⁰ and χ =10⁰ around the F-Well.

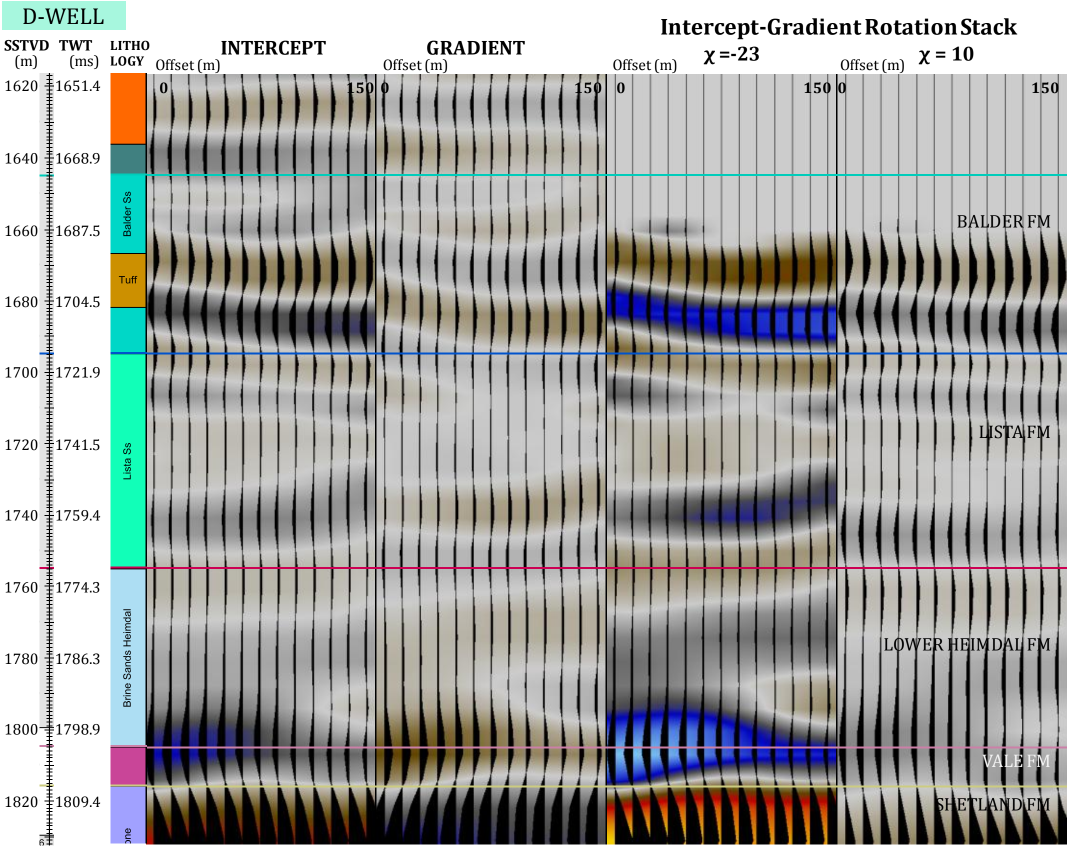

Figure 6.14 Intercept, gradient, EEI reflectivity of $\chi = -23^0$ and $\chi = 10^0$ around the D-Well.

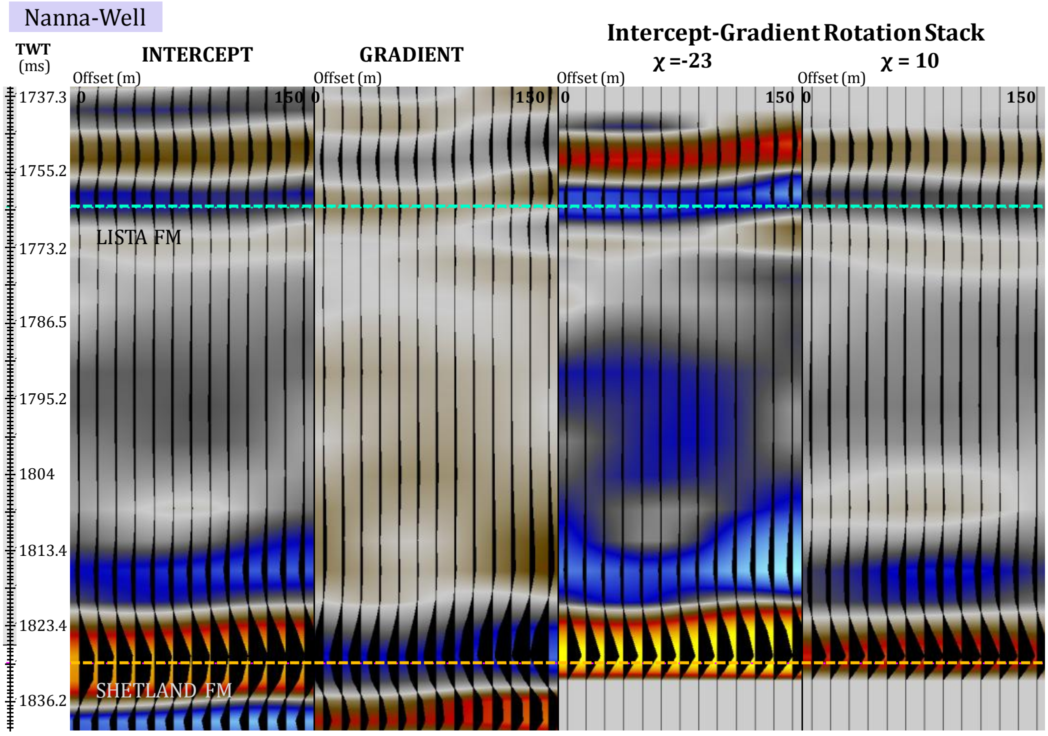

Figure 6.15 Intercept, gradient, EEI reflectivity of $\chi = -23^0$ and $\chi = 10^0$ around the Nanna-Well.

In summary, interpretation using the rotation stack of $\chi = -23^0$ alone is useful to distinguish the top of oil sands, the top of brine sands, and the thickness of Lower Heimdal sands. However, this intercept-gradient attribute is not adequate to provide the information regarding the thickness of oil-bearing sandstones. The most probable reason is these attributes related to reflection response that depends on the material properties as function of interface. The suggested solution is to perform seismic inversion. In Chapter 6.5, EEI is performed by involving inversion process in prior. It is expected that a good understanding of property of layers could be achieved by examining the impedance properties of the inversion result.

The rotation stack angle to the projection of fluid and lithology

The noise level in the intercept-gradient rotation stack depends on the degree of rotation. Whitcombe et al. (2004) observed that gradient contains more noise than the intercept. The lithology stack or $\chi = 10^0$ for this case is the stack direction which aligns with the maximum noise, while the direction that is nearly perpendicular to the background trend $\chi = -23^0$ is the stack direction with minimum noise (Figure 6.12). Even though in many cases the lithology stack is good in highlighting the sand or shale lithology, it seems that the performance of the lithology angle stack in this case is not optimal. An important aspect of AVO study that has to be understood is the AVO sensitivities are constrained to the local geological and environment. Instead of representing the local geology, the intercept-gradient trend of seismic data may indicate a trend with high noise level. Moreover, the overlapping value between reservoir and background within the intercept-gradient crossplot may causes problematic interpretation in rotation stack of $\chi = 10^0$ (Figure 6.12).

Correlation between the derived EEI reflectivity is calculated from the intercept and gradient volumes with respect to the well-log data of P-wave velocity, S-wave velocity and density. For all case, the correlation are maximum at $\chi = 10^0$, respectively (Figure 6.16). In Chapter 5.2 and Chapter 6.2.1, it had been discussed that the level of sensitivity for each parameter towards lithology and pore-fluid are given on different degree. Overlapping influences between lithology and pore-fluid, such as in $\chi = 10^0$, may cause unreliable interpretation in this EEI reflectivity attribute.

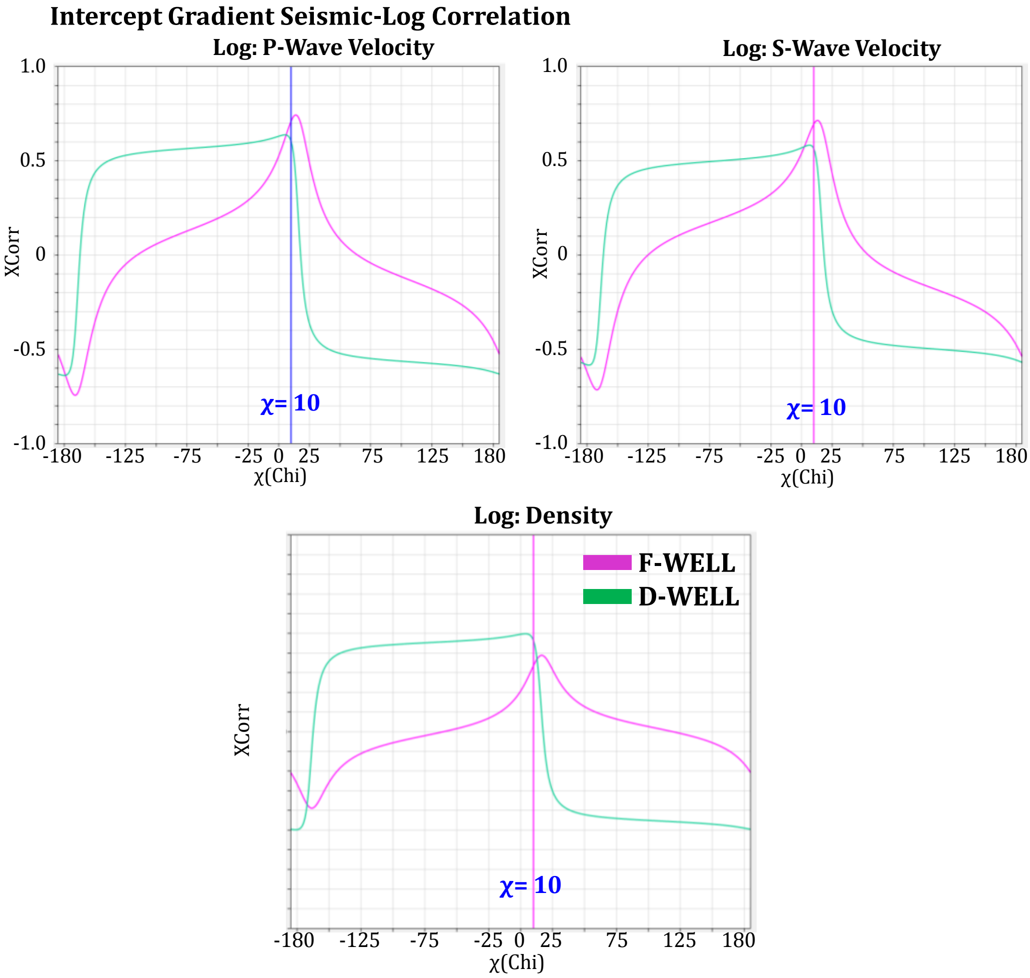

Figure 6.16 The derived EEI reflectivity for different angle of chi (χ) given by intercept-gradient seismic cube corresponds to different degree of correlation with the log data. The log data includes the P-wave velocity, S-wave velocity and density.

6.3 AVO/AVA

The top of Lower Heimdal at the F-well has higher amplitude decrement with function of angle, resulting polarity reversal at the far stack. Meanwhile at the D-well, polarity reversal at far stack is not obvious as it lies on the +/- zero-crossing. According to this observation and previous explanation in Chapter 5, the expected AVO response of shaly-sands and oil-sands interface is most likely defined as Class IIp as its gradient is higher than shaly-sands and brine-sands response, and showing polarity reversal at far angle. For a closely similar intercept response of top brine-saturated sandstones and top of oil-saturated sandstones (Figure 6.17), interpretation using the gradient has more benefits in separation of oil/brine sandstones lithologies.

The concept of AVO may help to simplify the relation of amplitude change with function of angle. For reflection coefficient up to 35^0, one might notice that around angle of 15^0 to 30^0 (Chapter 5.3), the trend provide the sharpest decrement in amplitude with function of angle. This trend is then followed with less amplitude decrement after 30^0. In a data with higher variation of reflectivity, such sharp decrement within angle of $15\text{-}30^0$ may cause the AVO line to cross at the angle less or equal to 30^0. Previous observation in Gassmann substitution (Chapter 5.1), also suggest that the AVO lines are crossing the zero reflection coefficient at degree of 25^0 to 35^0. This correspond to the higher-possibility for the AVO line of oil sandstones to cross the zero reflection coefficient around these angle. Therefore, the angle 30^0 is introduced as the angle of threshold to separate Class I from Class IIp. If the response belongs to Class I, zero crossing appears at angle higher than 30^0. If it belongs to Class IIp, zero crossing will appears at angle lower or equal to 30^0.

Close observation at AVO result suggests that the top of oil sandstones at the F-Well is defined by AVO Class IIp (Figure 6.17). What is interesting, this condition is also observed at the top of brine-saturated sandstones at the D-Well, where a thin mark of Class IIp lies across its top. This proved that at the far stack, the top of Lower Heimdal amplitude at the D-Well is very close to negative value instead of zero. Even though the top brine-saturated sands are most likely regarded as AVO Class I, the high reflection variation at seismic coupled with noise may lead this unit to be interpreted with different AVO class. For the top Lower Heimdal sandstones, the possibility of the top of brine-saturated sandstones to be classified as AVO Class IIp is supported within Chapter 5.1 and Chapter 5.3.

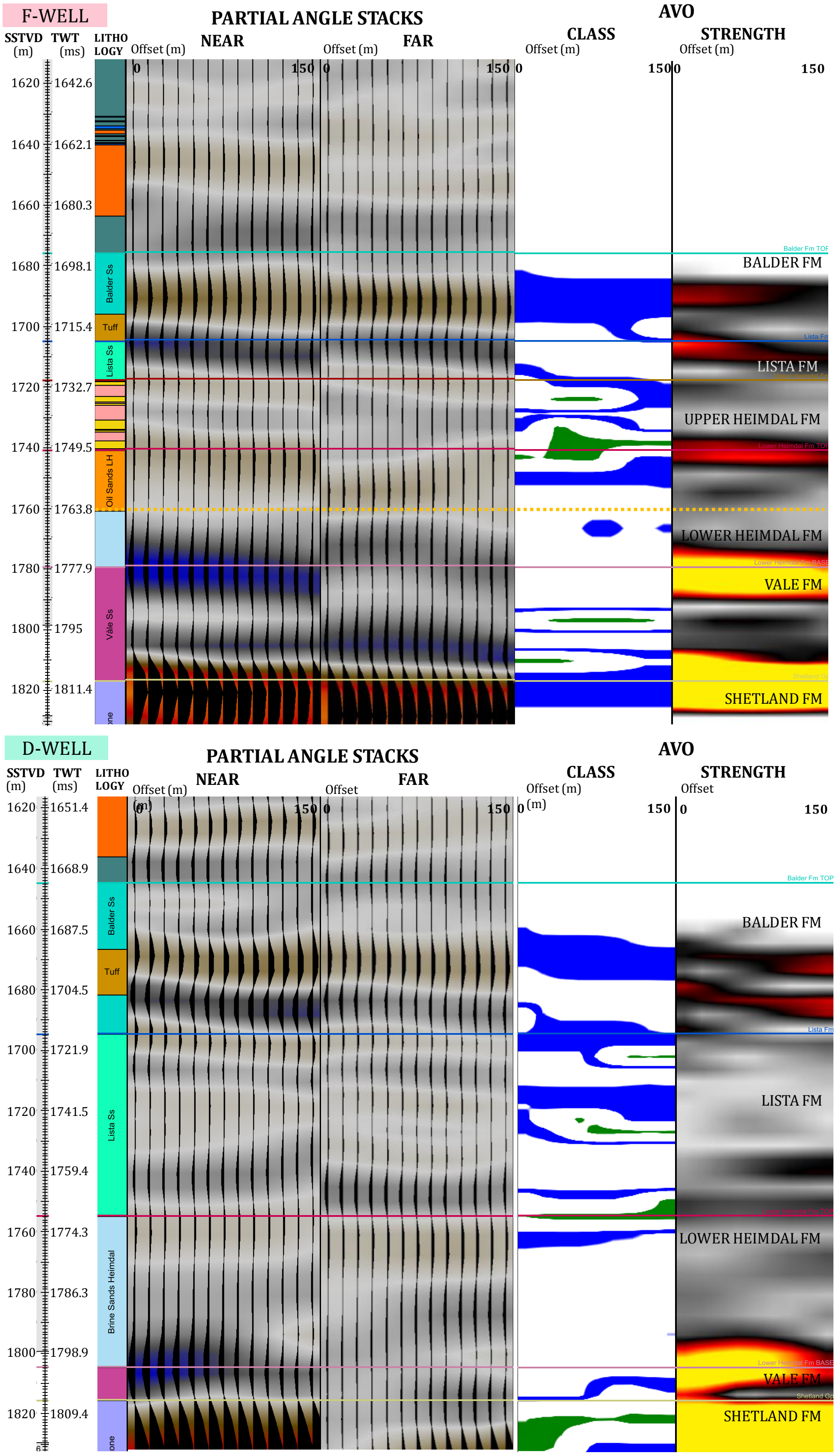

Figure 6.17 Near-far angle seismic stack, AVO Class and AVO Strength around the F-Well and D-Well. At AVO Class, green refers to Class IIp and blue refers to Class I.

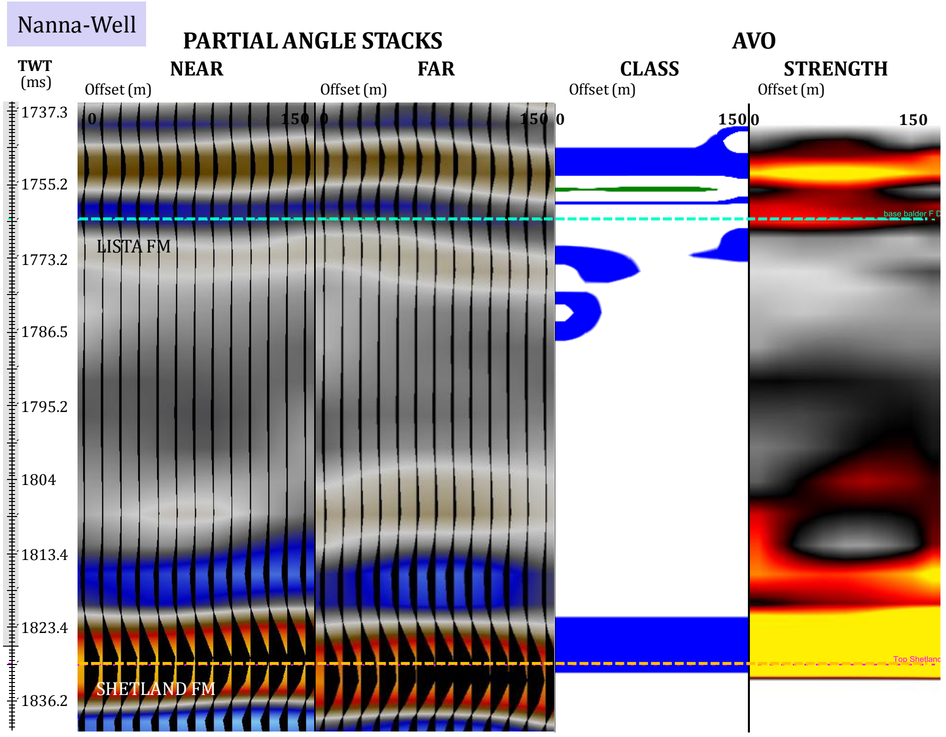

Figure 6.18 Near-far angle seismic stack, AVO Class and AVO Strength around the Nanna-Well. At AVO Class, green refers to Class IIp and blue refers to Class I.

As the sample points of intercept and gradient are spread across the four quadrants in the reflectivity space, the top of sandstones points (Figure 6.19) are embedded in the background trend (Figure 6.20). The top of brine-sandstones zone appears to be overlapping with the oil-saturated sandstones zones at the reflectivity space (Figure 6.19). In the same figure, it is also observed that the oil sandstones area is overlapping with the top Shetland limestones. The top of Shetland limestones is not always represented as AVO Class I but also AVO Class IIp (Figure 6.17). Similar with the top of oil-saturated sandstones, the top of Shetland limestones is distinguished from the brine-saturated sandstones as it has greater distance from the zero point (Figure 6.19).

Rather than the AVO class, the more robust method in pore-fluid identification of Lower Heimdal is by investigating its AVO strength (Figure 6.17). The main idea of AVO strength is to measure length of a certain sample point from the origin (Mahob and Castagna, 2003). Increasing the distance will exhibit larger value of AVO strength (Figure 6.19). This condition will ease the identification of anomalous events such as oil-saturated sands. Comparing to the top of brine-saturated sandstone at the D-Well, the top oil-saturated sands at F-well is indicated with stronger AVO strength (Figure 6.17). The stronger AVO strength is associated with the position of unit samples that lies further from the origin (Figure 6.19). The presumption of relative position of unit samples of top oil-sands and top brine-sands in intercept-gradient plot is coherent with the feasibility analysis (Chapter 5.3). The sensitivity of pore-fluid is higher at its gradient rather than the intercept value as the variation of gradient value is higher (Figure 6.19). Therefore, the AVO strength will closely relevant with the gradient.

Blind test interpretation will be difficult by using the intercept-gradient crossplot, as it has no information about depth and coherency within trace-to-trace system as function of 3D offset. As function of seismic trace (Figure 6.18), Nanna-Well is not showing any bodies with AVO Class IIp that followed with strong AVO strength. This observation will refer to the absence of oil-bearing sandstones at this well.

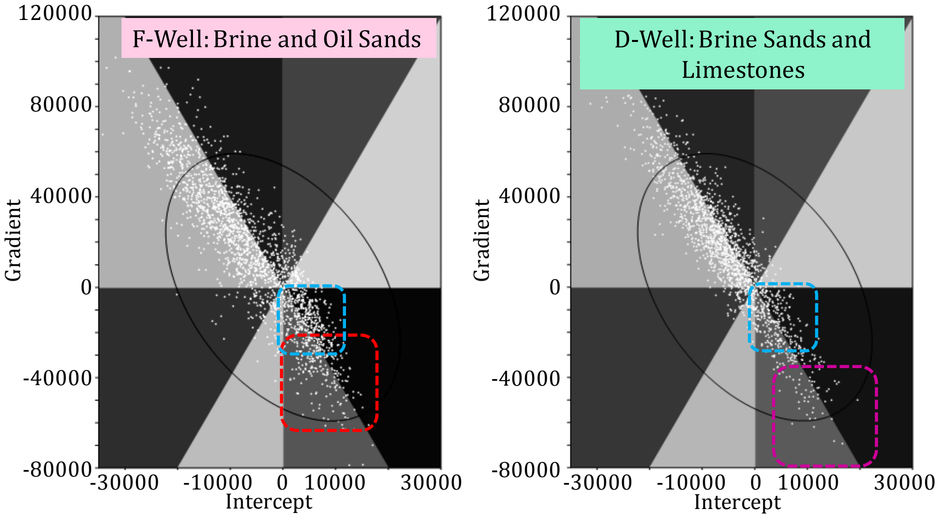

Figure 6.19 The red zone represents top of oil sandstones distribution, while blue represents top of brine sandstones distribution, and pink represents top of Shetland limestones distribution. Each zone is indicated across seismic profile in Figure 6.21 and Figure 6.22.

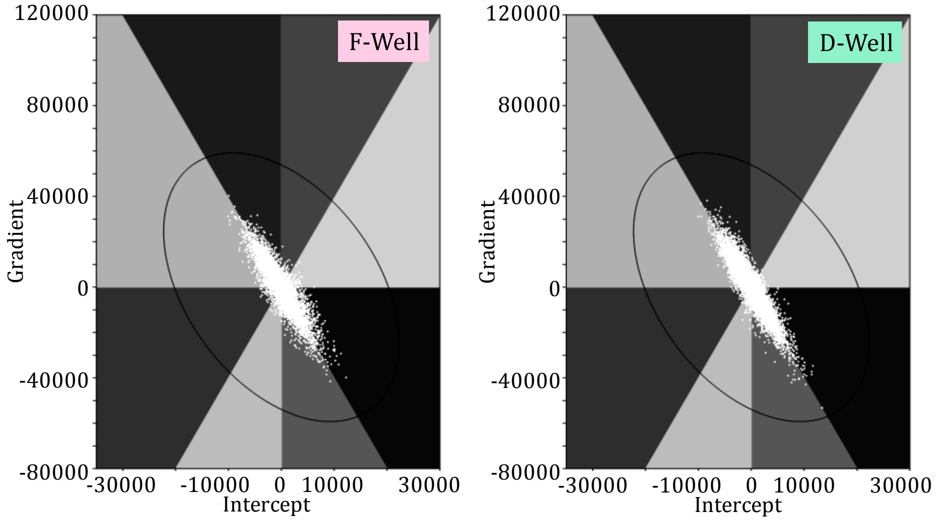

Figure 6.20 Background trend for both well appear with similar distribution area.

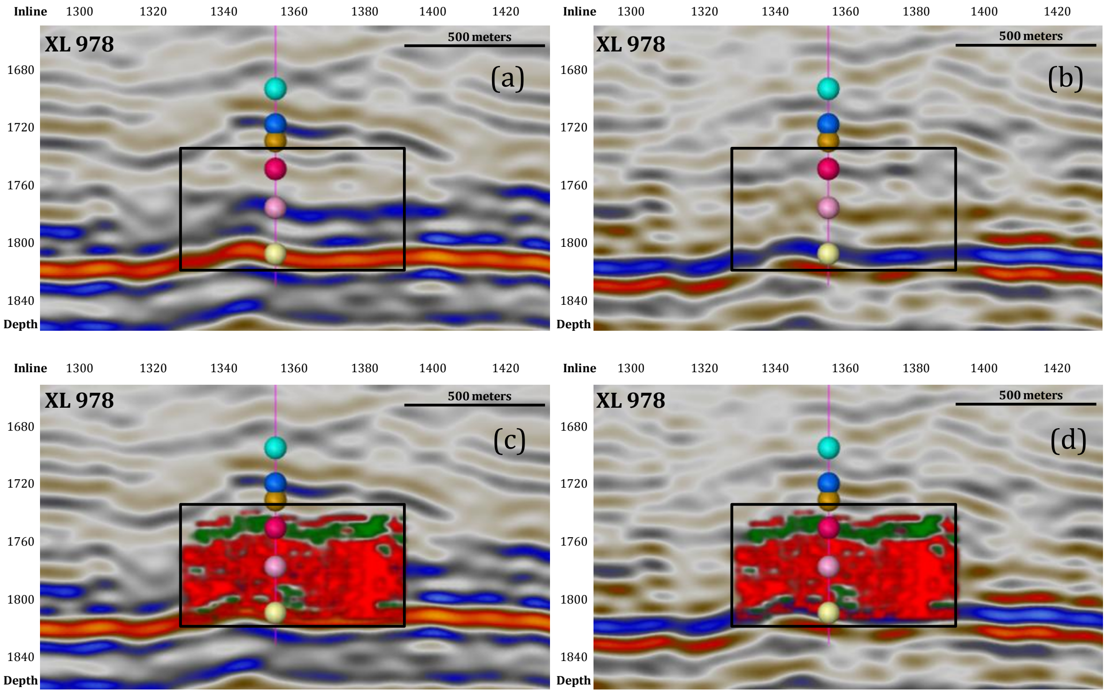

Figure 6.21 Local cross-section at XL 978 around the F-Well. In (c) and (d), within the squared area, the (a) intercept and (b) gradient cube are overlaid with red-green indicator, respectively. The green color shows the red zones (top oil-saturated sandstones) in Figure 6.19, and the red color shows its inverted zones.

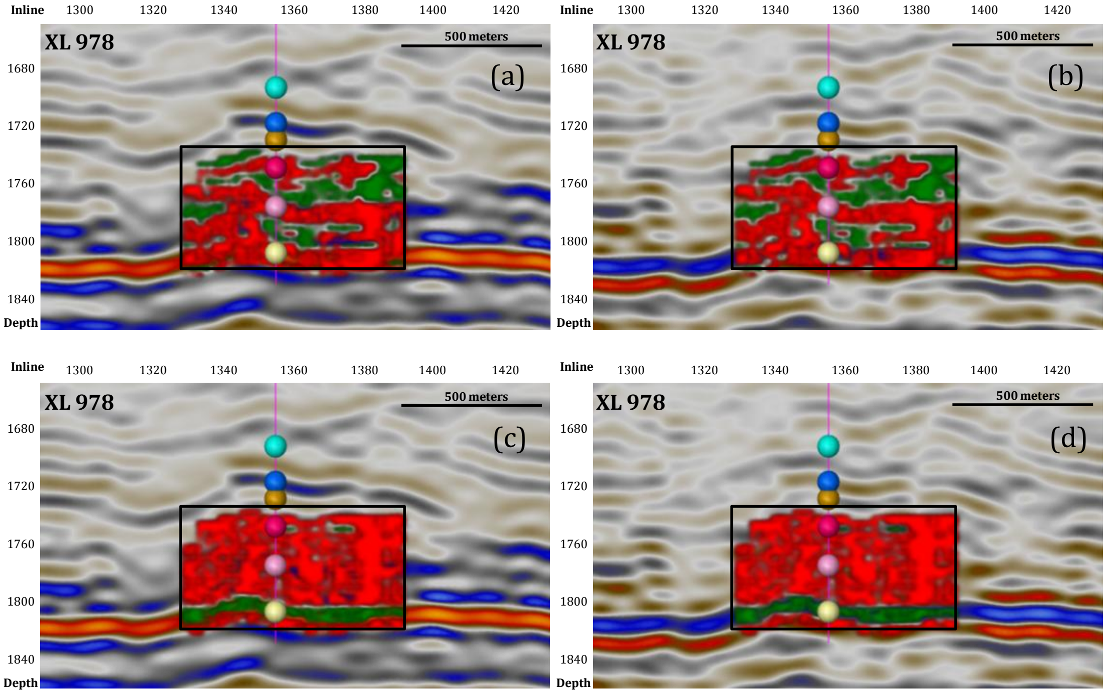

Figure 6.22 Local cross-section at XL 978 around the F-Well. Within the squared area, the intercept at (a) and (c), and the gradient at (b) and (d) are overlaid with red-green indicator. The green color in (a) and (b) are showing the blue zones (top brine-saturated sandstones) in Figure 6.19, while the green color in (c) and (d) are showing the pink zones (top Shetland limestones).

6.4 INTEGRATED ATTRIBUTES INTERPRETATION

Before highlighting the pore-fluid content in Lower Heimdal sandstones, the top of Lower Heimdal should be interpreted. Based on previous observation, Chapter 6.1 to Chapter 6.3, three seismic attribute are found to be useful in interpreting the top Lower Heimdal – gradient, EEI reflectivity χ=-23^0, and AVO Class (Table 6). Since the continuity of Class IIp in AVO Class cube is fair, less than 100 meters, the AVO Class is excluded from the top of Lower Heimdal interpretation strategies. To examine the interpretation performance of top Lower Heimdal formation across the gradient and EEI reflectivity χ=-23^0, interpretation is also performed across the near (or equivalently intercept) and far-angle seismic stack. In order to prevent misinterpretation of the top Lower Heimdal around the Nanna-Well, polygon is constructed. The polygon is also representing the area of interest for the top Lower Heimdal interpretation (Figure 6.26).

The strategy of the top Heimdal interpretation in the near angle seismic stack is done by picking the low-positive amplitude with value range of 1000 to 117464, while in far stack, the top of Lower Heimdal is picked across zero-crossing -/+ (Figure 6.23, Figure 6.24, and Figure 6.25). Using the gradient, the top of Lower Heimdal is picked across the low-negative amplitude with value range of -100 to -100000, while in the EEI reflectivity χ=-23^0, it is picked across the positive amplitude with value range of 5000 to 134478. All interpretations are accomplished based on auto-tracking interpretation, which also involve manual interpretation within only 10 inlines (IL 1356, IL 1170, IL 1230, IL 1310, IL 1430, IL 1470, IL 1130, IL 1389, IL 1150, and IL 1070). The manual interpretation acts as a guideline to extent the interpretation automatically in 3D setting.

CASE	SEISMIC ATTRIBUTES	TOP LOWER HEIMDAL PREDICITION	FLUID PREDICTION	ESTIMATION OF LOWER HEIMDAL THICKNESS
Case 1 (Chapter 6.1)	(1) Near angle stack	X	X	X
	(2) Far angle stack	X	V	X
	Combination of (1) and (2)	V	V	X
Case 2 (Chapter 6.2.2)	(1) Intercept*	X	X	X
	(2) Gradient	V	V	V
	Combination of (1) and (2)	V	V	V
Case 3 (Chapter 6.2.3)	(1) EEI reflectivity χ=10	X	X	X
	(2) EEI reflectivity χ=-23	V	V	V
Case 4 (Chapter 6.3)	(1) AVO Class	V	X	X
	(2) AVO Strength	X	V	X
	Combination of (1) and (2)	V	V	X

Table 6. Assesment summary for the quality of each seismic attribute based on three different component – the effectiveness top of Lower Heimdal prediction, fluid prediction, and estimation of Lower Heimdal thickness.

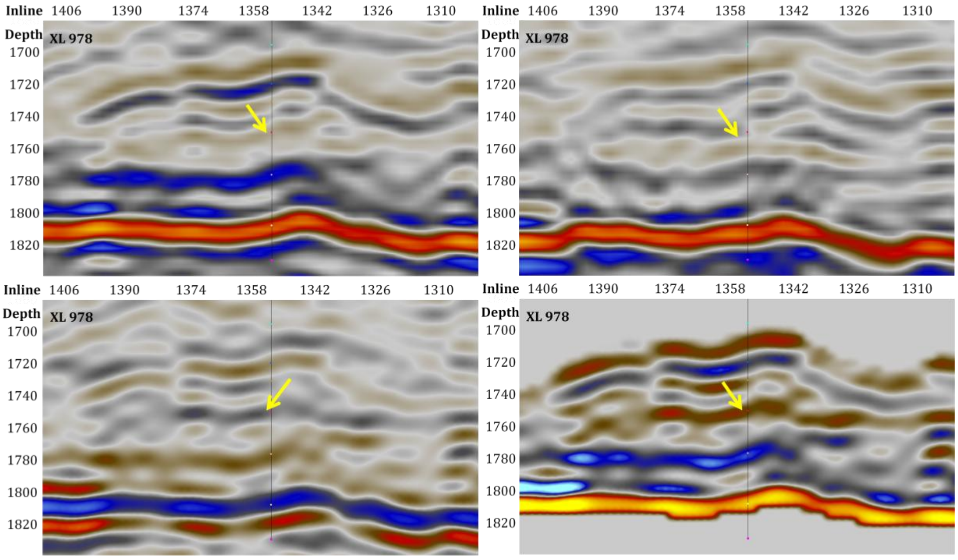

Figure 6.23 Top of Lower Heimdal is interpreted across the value shown by yellow point at (a) Near-angle stack (b) Far-angle stack (c) Gradient (d) EEI reflectivity χ=-23⁰.

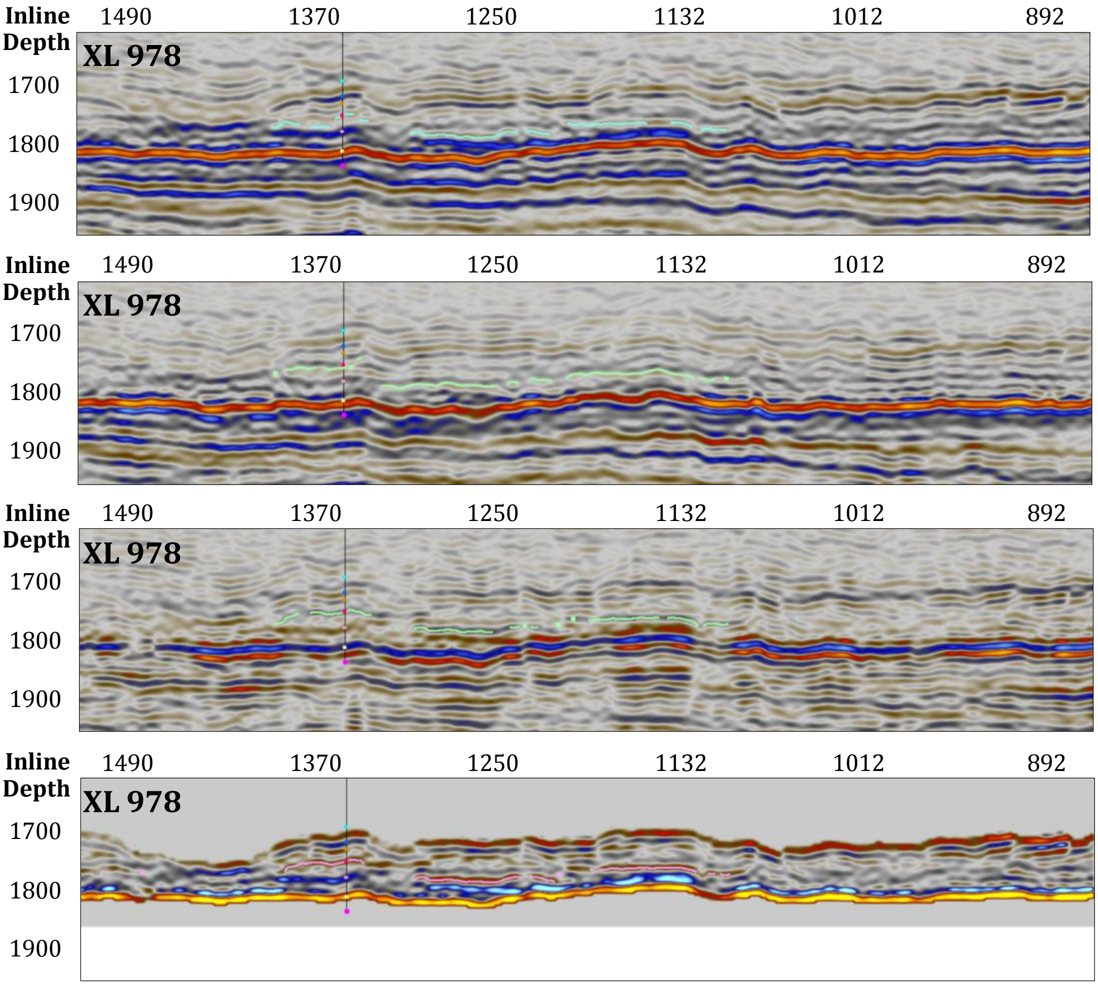

Figure 6.24 Interpretation profile of XL 978 given by a) Near-angle stack (b) Far-angle stack (c) Gradient (d) EEI reflectivity χ=-23⁰ seismic profile.

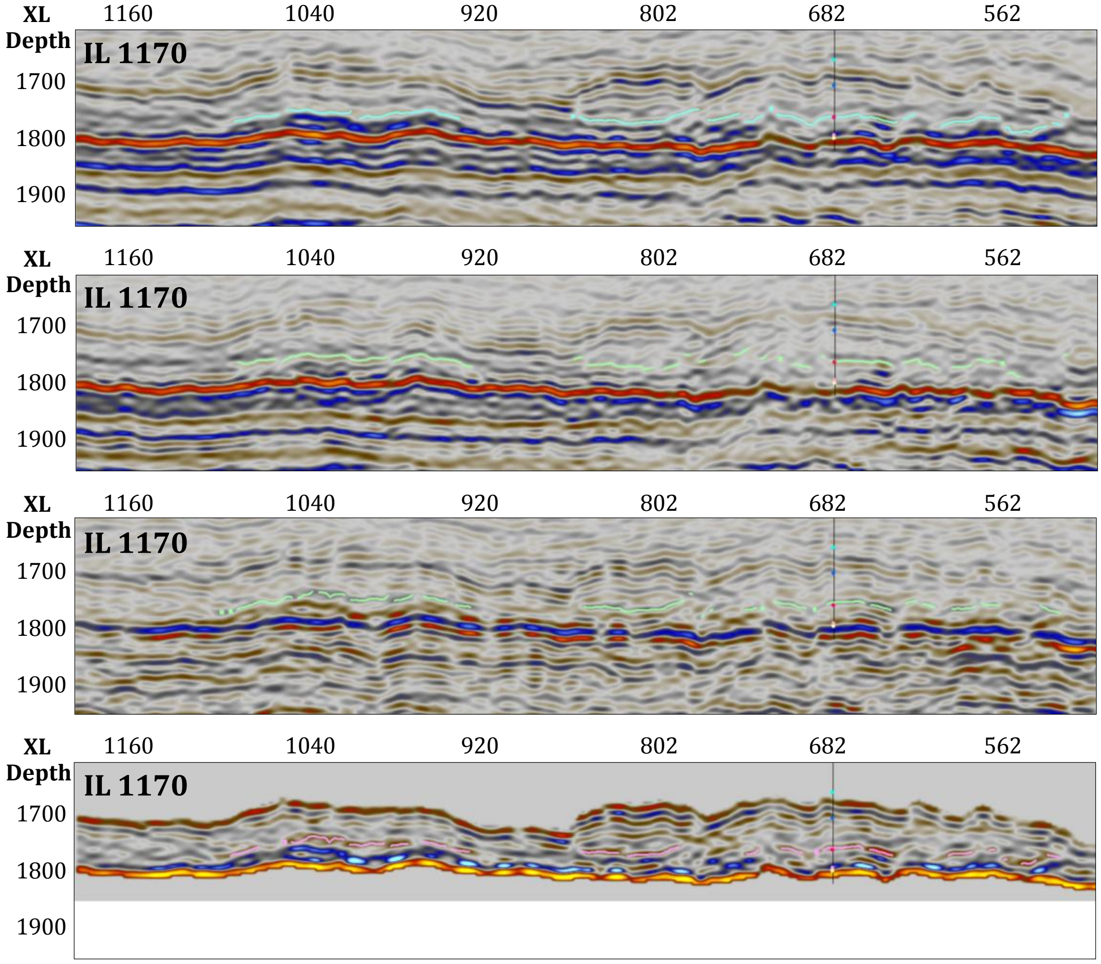

Figure 6.25 Interpretation profile of IL 1170 given by a) Near-angle stack (b) Far-angle stack (c) Gradient (d) EEI reflectivity χ=-23^0 seismic profile.

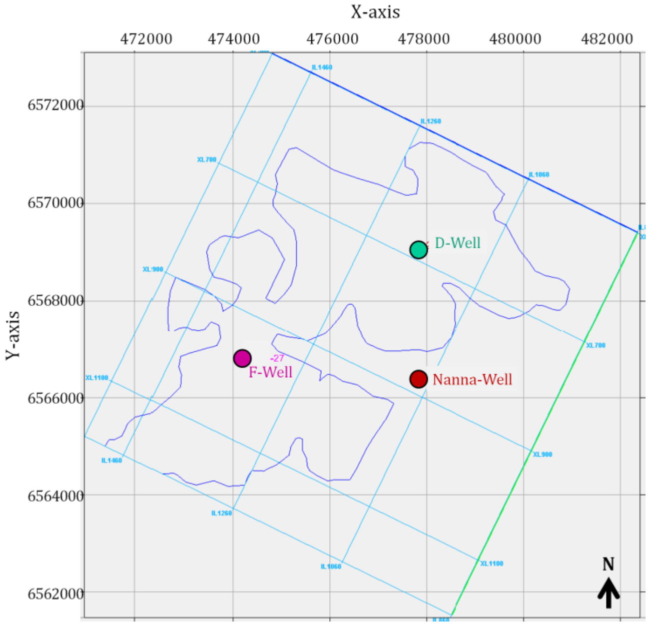

Figure 6.26 Polygon (blue colour) representing the area of interest for top Lower Heimdal interpretation in 3D setting.

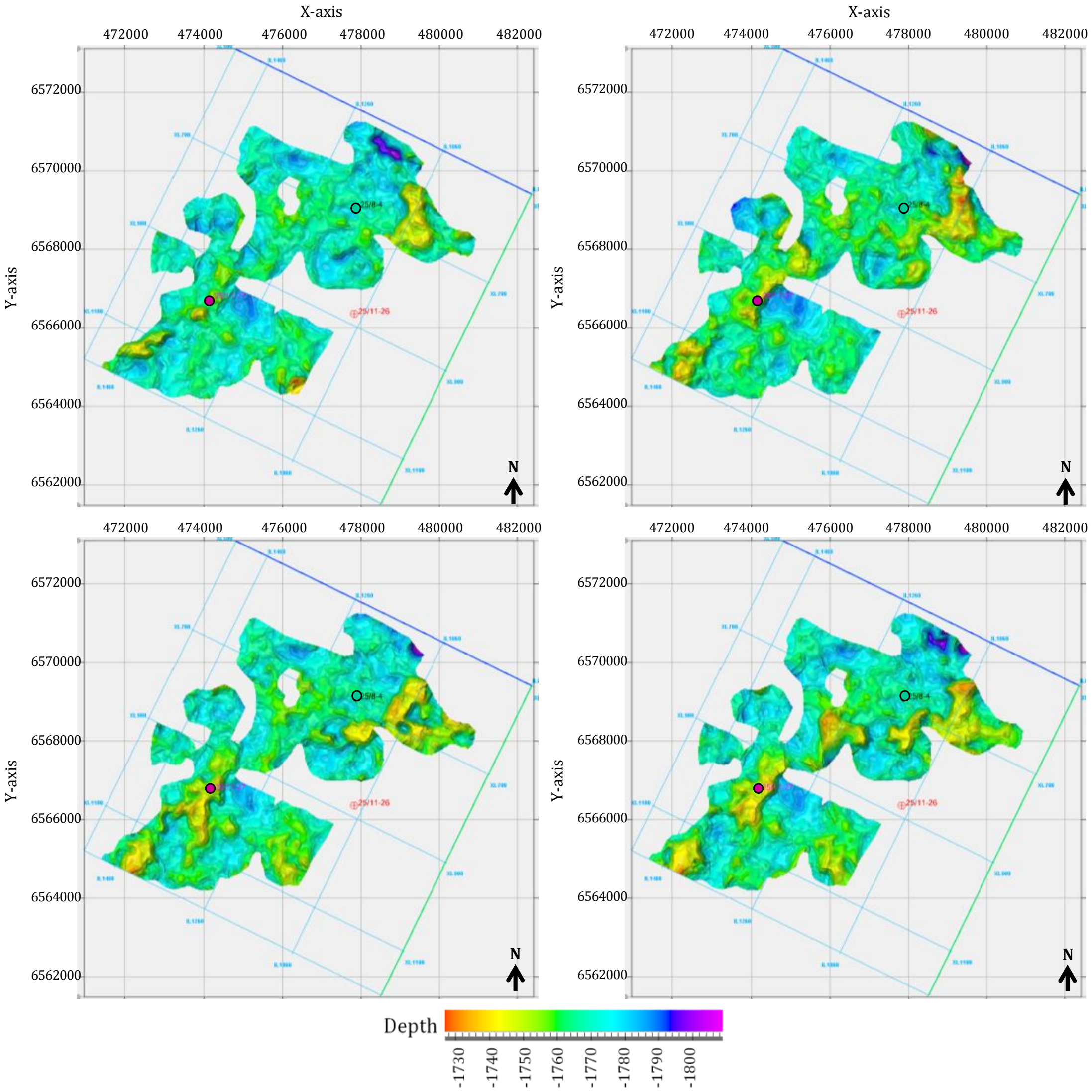

Figure 6.27 Time-depth map of top Lower Heimdal given by seismic profile of (a) Near-angle stack (b)Far-angle stack (c)Gradient (d) EEI reflectivity $\chi=-23^0$.

Top Lower Heimdal Prediction

Interpretation across the 2D seismic profiles showing that around the F-Well and the D-Well, the target unit or the Lower Heimdal formation, appears as mounded seismic character (Figure 6.23). Because of its character, the lateral continuity of Top Lower Heimdal is very fair in every seismic profile (Figure 6.24 and Figure 6.25).

The time structural maps of Lower Heimdal given by four different seismic profiles are mainly showing three distinct structural highs (Figure 6.27). The first high is located in the south-west of the F-Well with a parallel local extent in the north-east direction. The second high is located around F-Well, with relief direction trend similar to the first high. The second structural relief is wider at gradient and EEI reflectivity $\chi=-23^0$

structural maps. The third high is located along the eastern to the southern side of D-Well. Each identified highs, is later called SH 1, SH 2, and SH 3.

From four different interpretation profile, the structural map given by gradient and EEI reflectivity χ=-23^0 provide good coherency in interpretation of top Lower Heimdal (Figure 6.27). Guided by interpretation profile given by these two seismic attributes, a joint interpretation is executed to promote the quality of interpretation (Figure 6.28). This interpretation is performed by manually pick the suspected amplitude of top Lower Heimdal in every 10 crossline/inline interval. Similar to previous investigation, the resulting time structural maps of integrated top Lower Heimdal interpretation is also showing the structural highs, SH 1, SH 2, and SH 3.

Top of Lower Heimdal formation is located structurally lower in the D-Well than in the F-Well (Figure 6.28). At a deeper basin, the chance for the well to be dry is high since the hydrocarbon tends to migrate upward to higher flank. Assuming that OWC lies closely at 1763 ms, the structural highs, SH 1, SH 2, and SH 3, thought to be interesting blocks as they sit approximately 15-25 ms shallower than OWC. Supported with this condition, the probability to find oil-bearing sandstones is higher within these structural highs.

Fluid Prediction

There are four attributes that found to be useful to highlight pore fluid content – AVO Strength, Gradient, and EEI reflectivity χ=-23^0 (Table 6). Using the integrated interpretation of top Lower Heimdal (Figure 6.28), each seismic attribute values are extracted across the top Lower Heimdal time surface map. The top of Lower Heimdal sandstones around the F-Well area is mainly represented by zones of high AVO strength, low amplitude gradient, high amplitude of EEI χ=-23^0 attribute, and (Figure 6.29, Figure 6.30, and Figure 6.31). Each corresponding attributes value of F-Well is named as value of interest (VOI). The VOI is representing the value of where the probability to find oil-bearing sandstones is high. By adapting these features, an interesting point is picked in the southern highs of D-Well (arrow at Figure 6.29, Figure 6.30, and Figure 6.31).

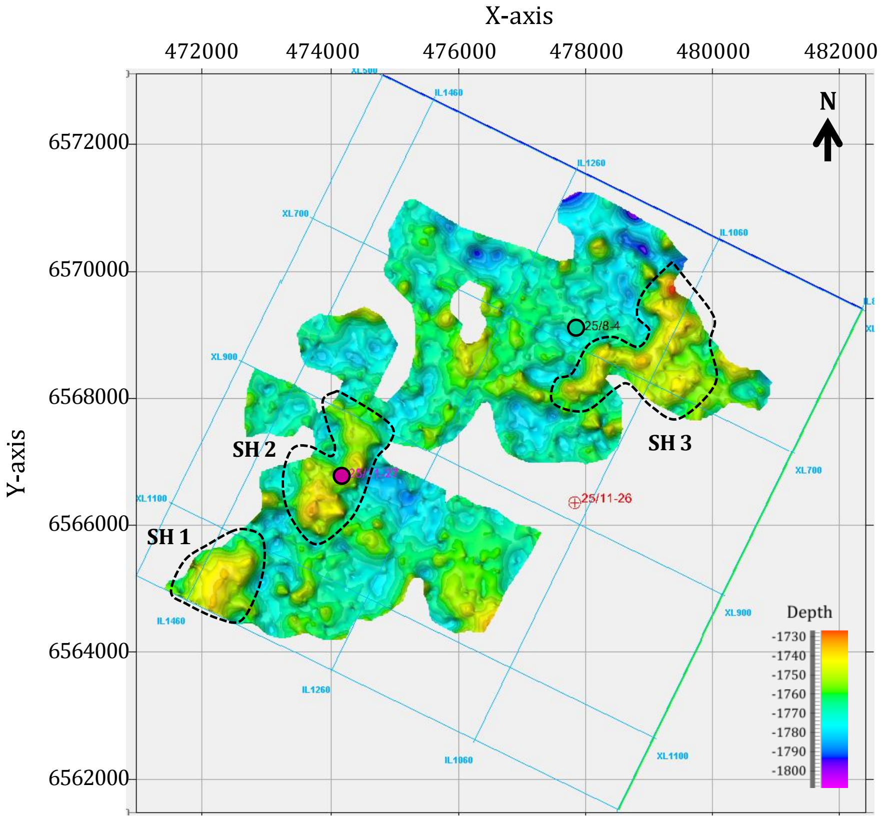

Figure 6.28 An integrated time-depth map of top Lower Heimdal.

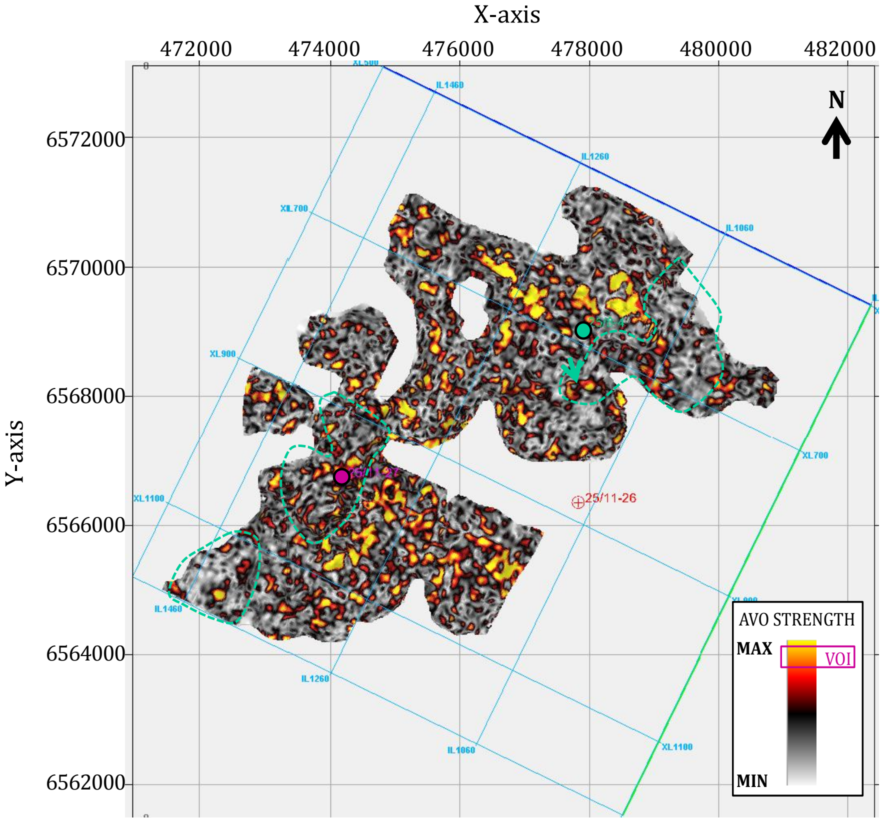

Figure 6.29 An AVO Strength distribution map across the top Lower Heimdal.

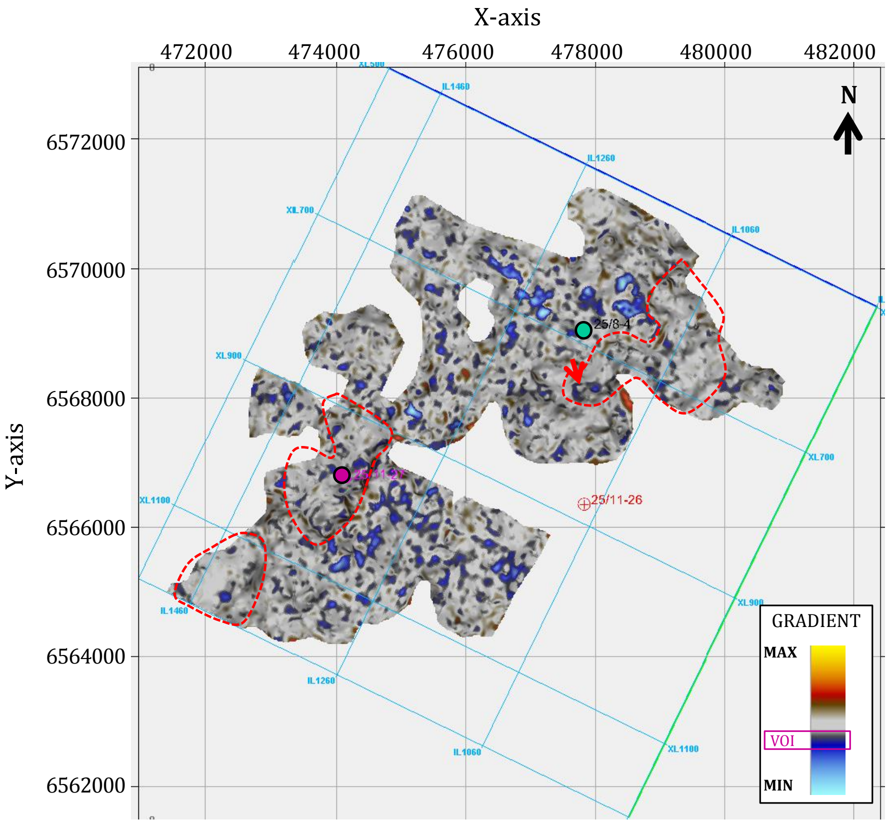

Figure 6.30 A gradient distribution map across the top Lower Heimdal.

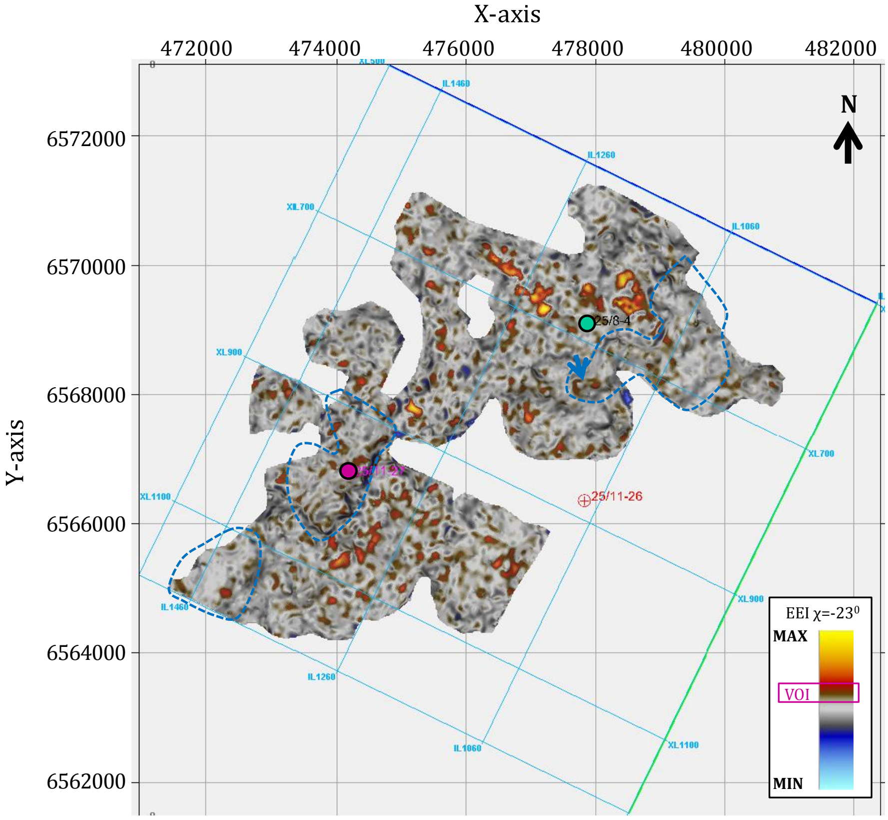

Figure 6.31 A EEI reflectivity χ=-23^0 distribution map across the top Lower Heimdal.

6.5 INVERSION

Seismic inversion techniques transform the response of layer contrast across the layer's boundary into corresponding layered response as an impedance model. Impedance is closely related to lithology, porosity, pore-fluid and other geological factor. The impedance model therefore facilitates more meaningful explanation in terms of geological and petrophysical, and a link between seismic and well-data. In this study, three different deterministic inversions are implemented to estimate the impedances, the band-limited trace integration, coloured inversion, and combination of coloured inversion with EEI. All inversion processes do not incorporate any low frequency model.

6.5.1 BAND-LIMITED TRACE INTEGRATION

The simplest form of inversion, known as trace integration, directly estimates the relative impedance with no model inputs and does not incorporate the low frequency information from the well. The trace integration is usually performed in the earlier stage of exploration to identify the favorable strata, by running sum of regularly sampled amplitude values. The integrated seismic trace is then filtered by using a high-cuts Butterworth filter at 6dB/octave. After the estimated impedance has been generated, the quality of the final inversion has to be quality checked. A single trace of the band-limited impedance computed by trace integration (AI TI), are correlated with the impedance log (Figure 6.32 and Figure 6.33). The resulting correlation coefficients act as an index to evaluate the impedance estimation. Prior to this examination, in order to make a valid comparison between log data and inverted impedance, the impedance log is needed to be adjusted to match the bandwith of seismic by band-pass filtering. The filtered log is then referred as AI-BL. Good correlation is shown for the F-Well, but not in the D-Well (Figure 6.32 and Figure 6.33). The low correlation coefficient in the D-Well is later proven to justify that the impedance result may cause a false interpretation.

In terms of distinguishing the pore-fluid, the inversion result in the F-Well (RAI) provides good correlation with the band-limited impedance log (AI-BL) within the Lower Heimdal unit. In this unit, the oil-saturated zones are indicated by lower impedance than brine-sands (Figure 6.32). However, implementing the Lower Heimdal seismic feature of the F-Well for prediction in the D-Well will cause misinterpretation. As the RAI of Lower Heimdal sandstone in the D-Well is represented by low impedance, one will presume this unit to be oil-saturated sands rather than brine-saturated sandstones (Figure 6.33). Such misinterpretation in the D-Well is also supported by the low-correlation given by correlation of RAI with AI-BL. From this observation, it is therefore summarized that the seismic character of RAI is not sensitive towards pore-fluid variation. In terms of lithology identification, the Lower Heimdal sandstones in the F-Well and D-Well are characterized by positive impedances. However, taking this assumption for the Nanna-Well interpretation will cause misinterpretation, as the low positive impedance feature leads to assumption of 35ms thick sandstones (Figure 6.34).

As the trace integration inversion does not involve many parameters within the process, there are only two possibility of the unsuccessful inversion result, the lack of low-frequency data and the problem in the wavelet of seismic data. Lack of low-frequency data will cause the inversion result to be not optimal in providing the true impedances. Similarly, with having non-zero wavelet within seismic data will cause the inversion process to be not valid. The extracted wavelet in the near data confirms that it does not precisely zero-phase in the D-Well (Figure 6.5). A suggested procedure is to perform wavelet processing to replace the asymmetrical pulse in the seismic data with zero-phase wavelet.

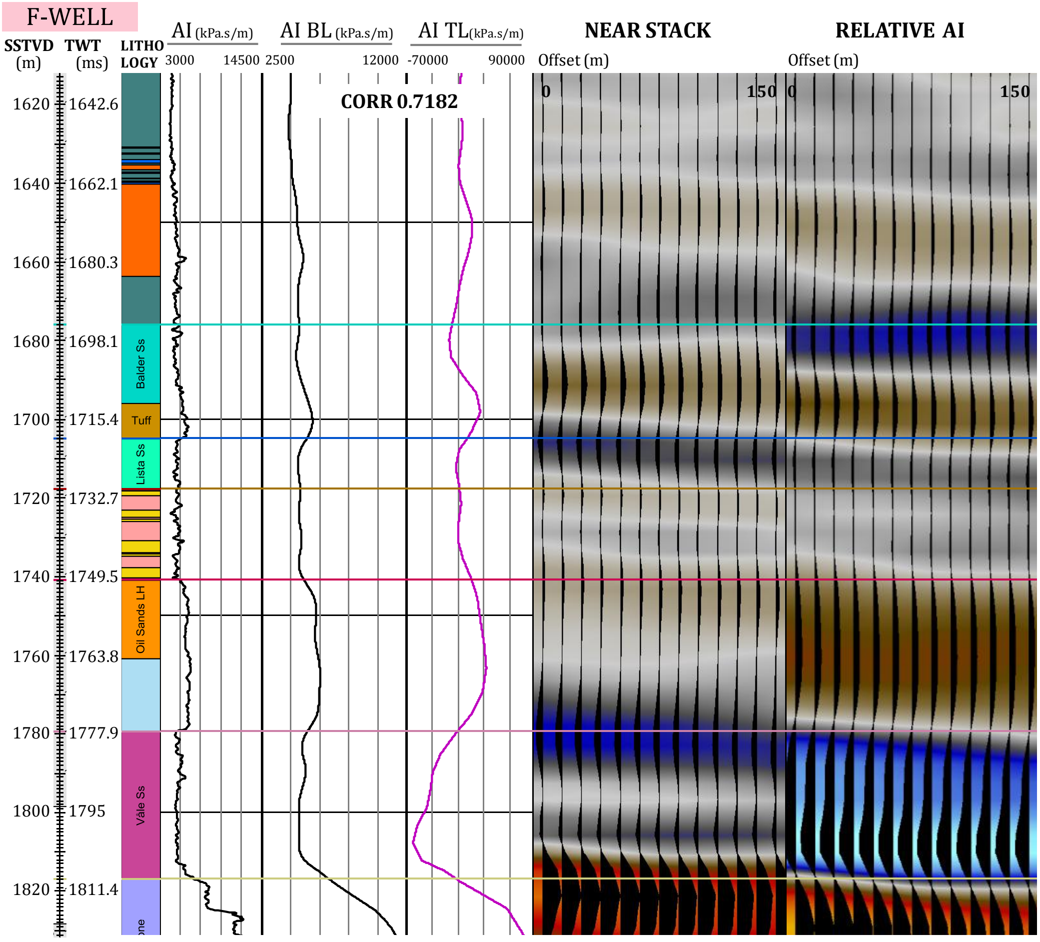

Figure 6.32 AI log, AI log after band-pass filtered, AI extracted from derived seismic impedance, near angle stack, and derived impedances around the F-Well.

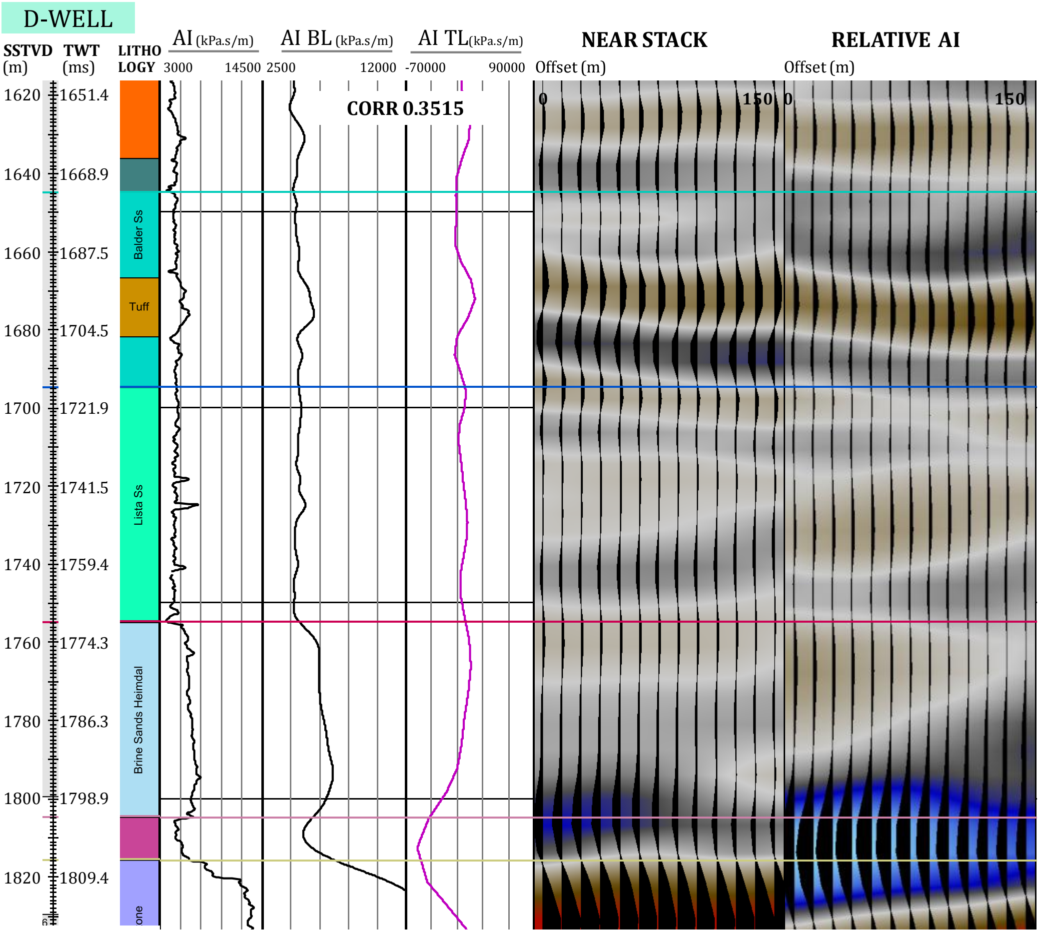

Figure 6.33 AI log, AI log after band-pass filtered, AI extracted from derived seismic impedance, near angle stack, and derived impedances around the D-Well.

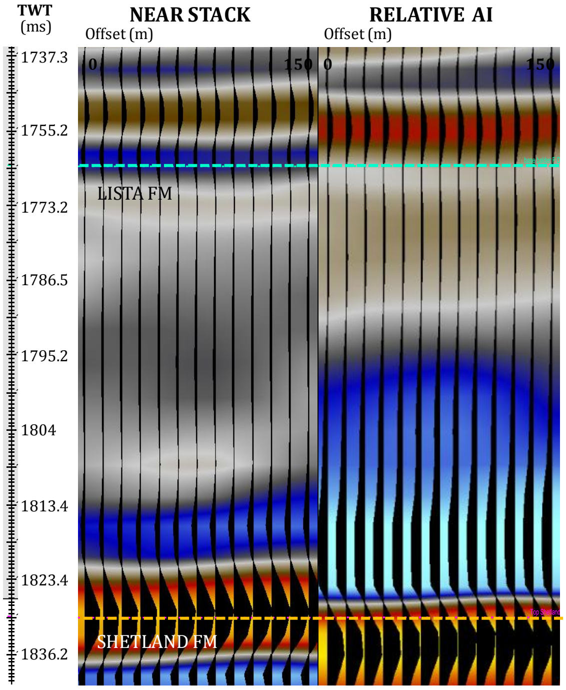

Figure 6.34 The near angle stack, and derived impedances around the Nanna-Well.

6.5.2 COLOURED AND EEI INVERSION

Another form of deterministic inversion, called Coloured Inversion is an inversion process that creates a volume by rotating -90^0 with respect to the reflection data, and which amplitude spectrum matches the well log impedance (Lancaster and Whitcombe, 2000; Maynard et al., 2003). Using coloured seismic inversion, intercept and gradients volumes can be inverted to relative acoustic impedances (RAI) and gradient impedances (GI) volumes, respectively. As in the reflectivity domain (Chapter 6.2.3), combination of RAI and GI can be used to generate a new attribute. This attribute called EEI, is an attributed derived from function of angle rotation of RAI and GI in the impedance domain.

Coloured Inversion

In coloured inversion method, seismic spectrum is adjusted to roughly match the average spectrum observed in impedance logs by using a proper wavelet called coloured inversion operator (CI operator). Two operators are introduced to understand the impact of frequency bandwith in resulting band-limited impedance volumes (Figure 6.35 and Figure 6.36). The first CI operator (CI operator 1), has a wider low frequency range than the second CI operator (CI operator 2).

The coloured inversion technique is proven to boost the low frequency part of the seismic spectrum as the frequency range 10-20 Hz in Figure 6.37 dominates after the inversion process. By taking the RAI and GI frequency spectrum for each operator (Figure 6.37b and Figure 6.37c), frequency range of 10 Hz escalates more within RAI/GI given by CI operator 1 than CI operator 2. Since the operator is acting as band-pass filter of the real impedance to the seismic band-width, with greater low frequency range in CI operator 1, the low frequency range within the derived RAI/GI volume will also enhance.

In the beginning of inversion, the resulting RAIs from the inversion need to be quality checked. This is done by examining the RAI seismic values taken across the borehole trajectory and the band-limited impedances log values (AI-BL). Comparison of a single trace from the inversion result (AI CI-1 and AI CI-2) with the AI-BL show relatively small correlation coefficients (Figure 6.38). The extracted RAI from seismic (AI CI-1 and AI CI-2) are lacking sense of trend, due to the lack of low frequency components (frequency less than 10 Hz). The absence of trend in RAI is particularly shown in the Lower Heimdal sandstones interval. The increasing impedance trend in log data across the top of Lower Heimdal is absence in the RAIs. An example of the importance of low frequency is particularly shown by taking a comparison of AI-CI 1 and AI-CI 2, where the RAI given by AI-CI 1 provides better correlation with impedance log rather than the AI-CI 2. As the RAI frequency spectrum of AI-CI 1 has greater low-frequency range, the correlation with impedance log also escalates.

Figure 6.35 Normalized amplitdue of coloured inversion operator 1 and 2.

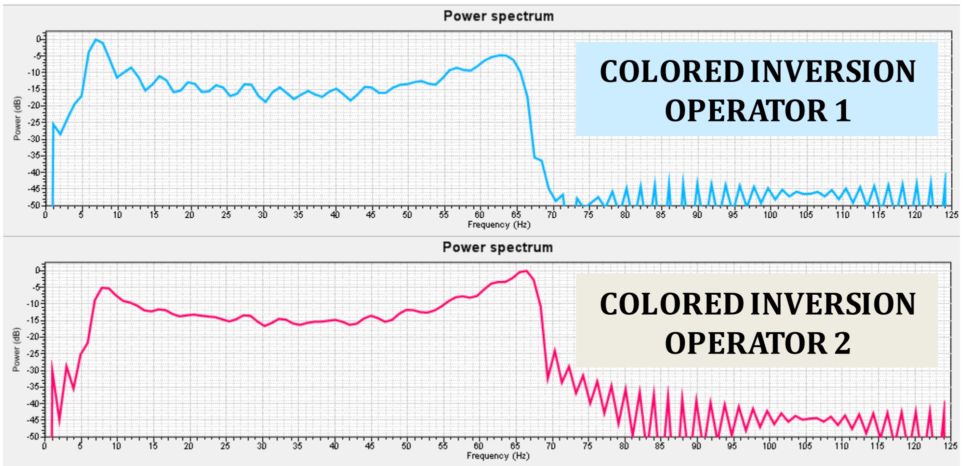

Figure 6.36 Amplitude spectra (dB) of coloured inversion operator 1 and 2.

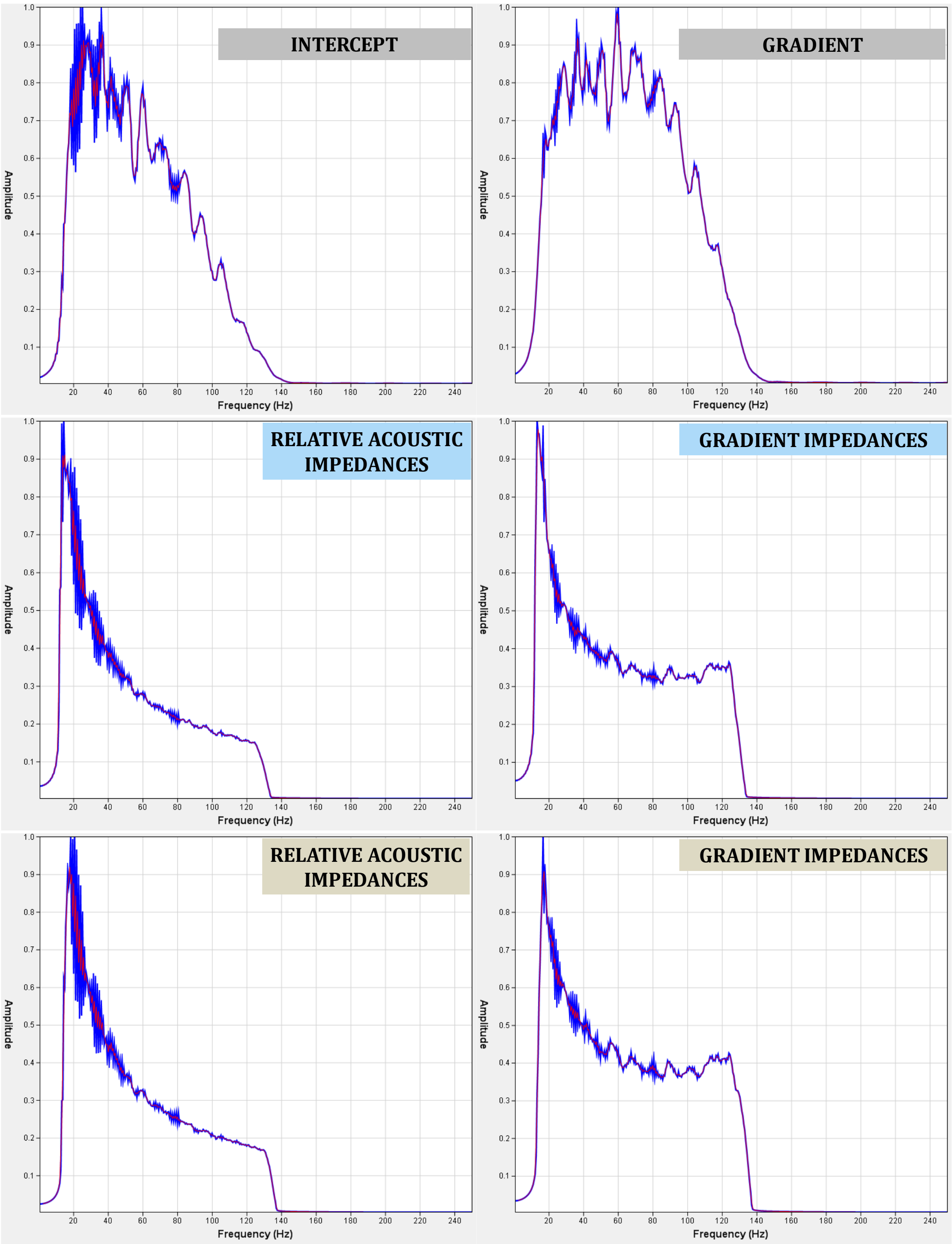

Figure 6.37 (a) Intercept and gradient amplitude spectra. Relative acoustic impedance (left) and gradient impedances (right) as the inversion product by using CI operator 1 (b), CI operator 2 (c).

The quality of the inversion output can also be measured by its ability to predict away from the wells, including by using a blind well test (Figure 6.39 and Figure 6.40). The RAI feature of Lower Heimdal sandstones given by the F-Well is shown as low positive value. On the contrary, the Lower Heimdal sandstones in the D-well are not characterized by the same feature (Figure 6.39). Adopting the seismic features of the F-Well to interpret the location of Lower Heimdal sandstones on the D-Well, will cause misinterpretation. On the D-Well, the seismic character of the Lower Heimdal sandstone is most likely reflecting shaly-sand lithology of the F-Well. As the seismic signature in the F-Well failed to guide the interpretation in the D-Well, the quality of interpretation using impedance is also low for the entire area.

Gradient impedance however, is also not sensitive towards lithology change but the oil-bearing sandstones are able to be highlighted. The oil-bearing sandtones of the F-Well is shown as strong negative amplitude, while the background lithology characterizes as low negative to strong positive amplitude (Figure 6.39).

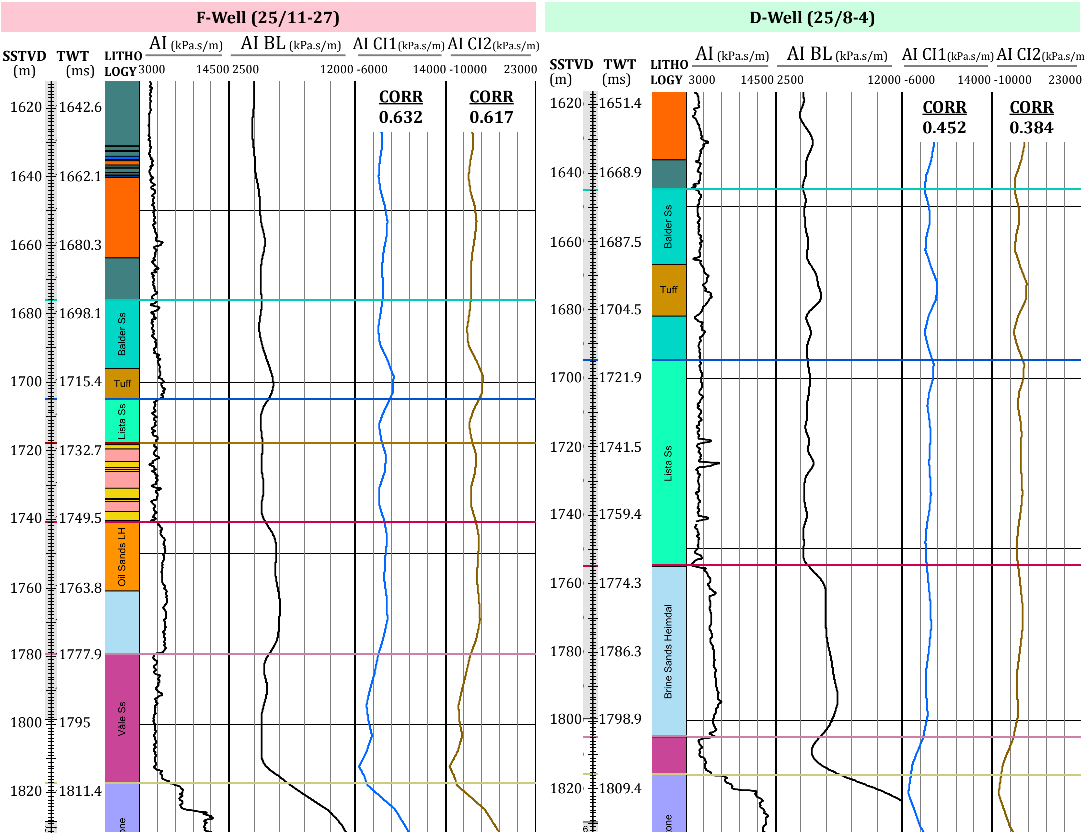

Figure 6.38 P-Impedance or acoustic impedance log (AI), band-limited acoustic impedance log (AI BL), relative impedance as inversion solutions from respective CI operator (AI CI 1 and AIC CI 2). Notice that the correlation of AI BL and AI CI at D-well is nearly half value less than F-Well

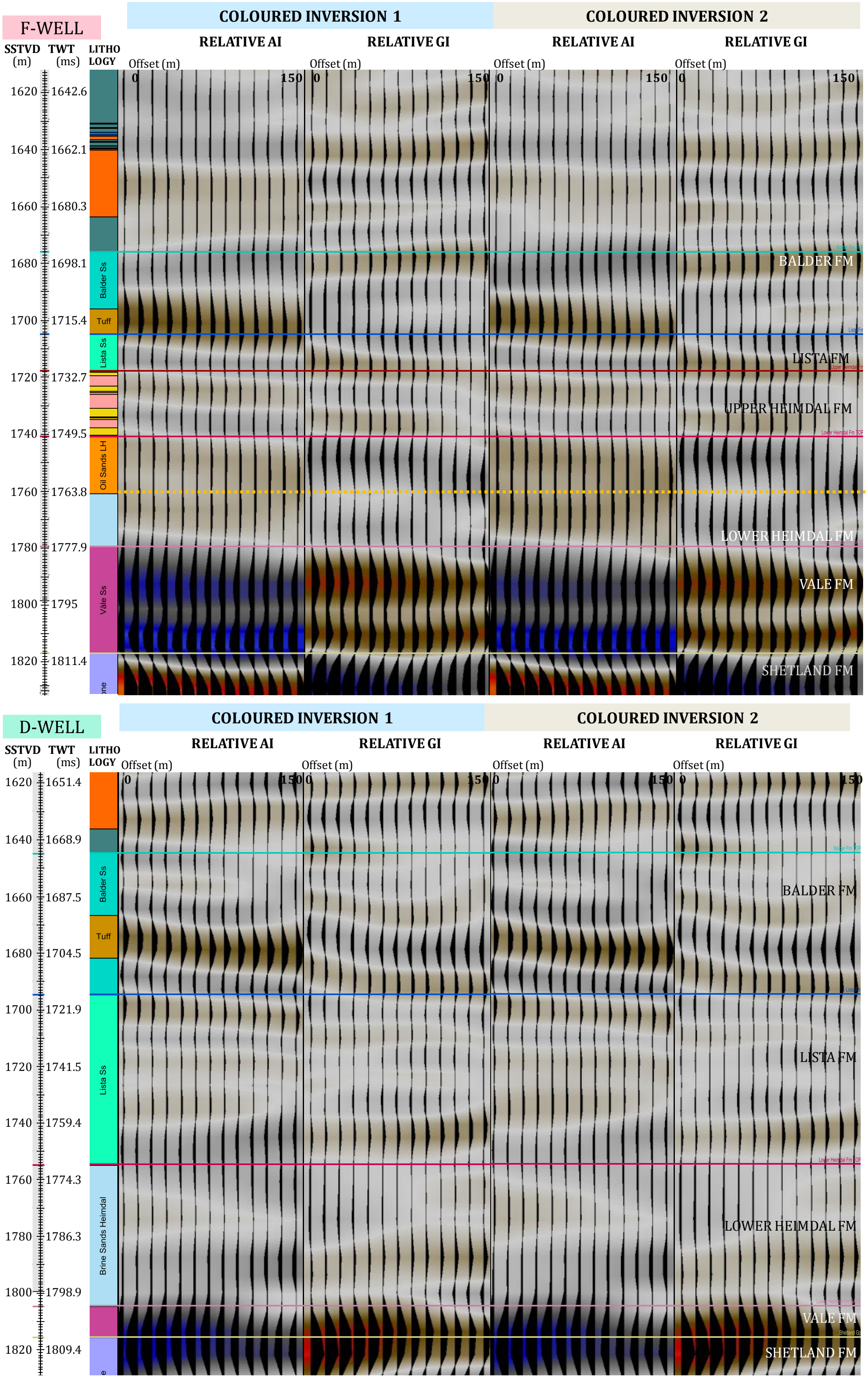

Figure 6.39 The derived acoustic and gradient impedances for each CI operator around the F-Well (top) and the D-Well (bottom).

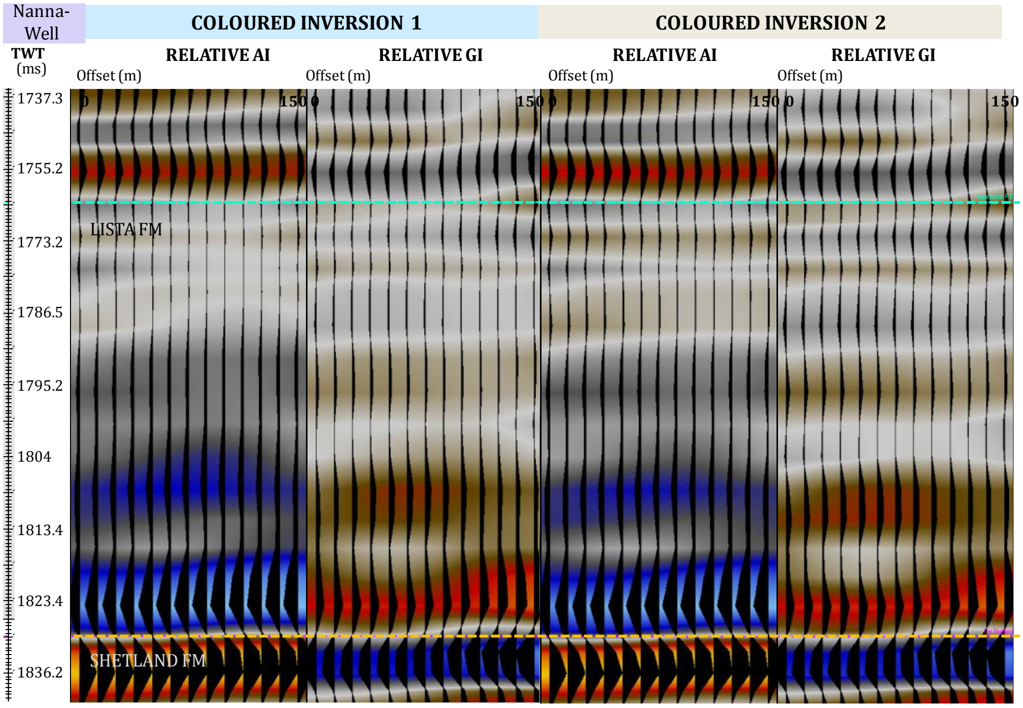

Figure 6.40 The derived acoustic and gradient impedances for each CI operator around the Nanna-Well.

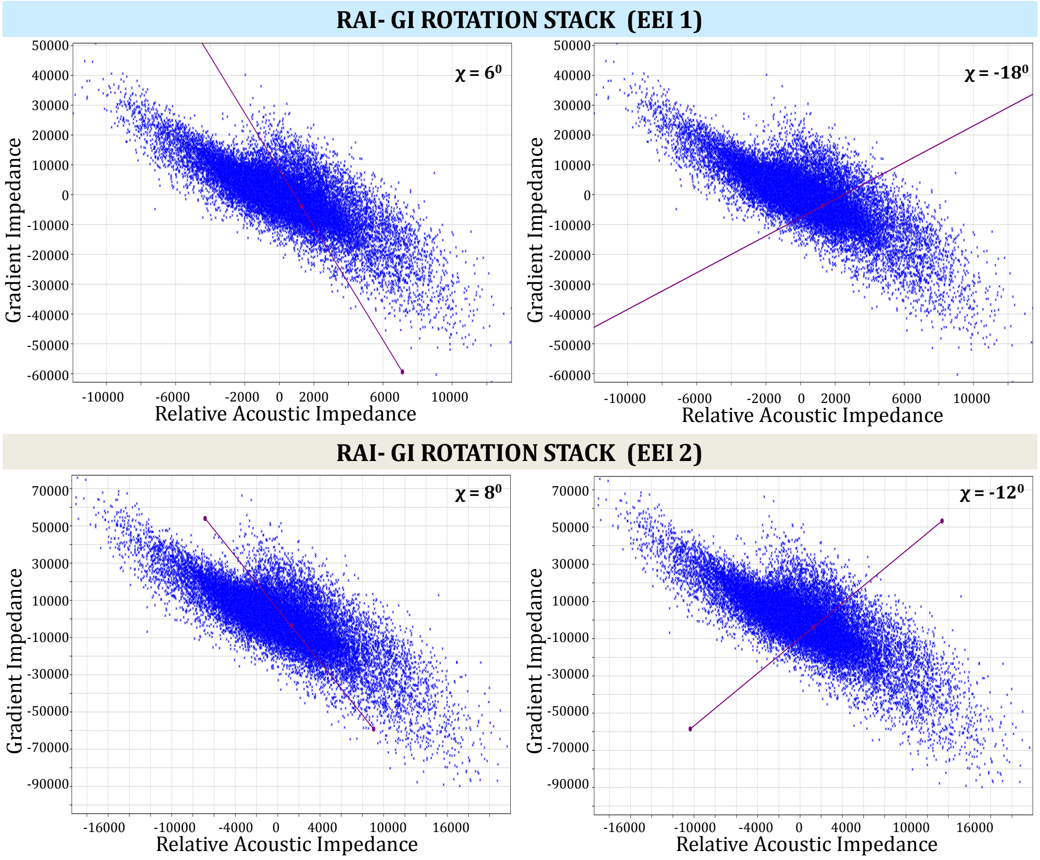

Figure 6.41 The angle of chi (χ) chosen to build the EEI using the RAI and GI derived from each operator. χ = 6 and χ = -18 for CI operator 1, and χ = 8 and χ = -12 for CI operator 2.

Extended Elastic Impedance (EEI)

With combination of RAI and GI, coordinate rotation or EEI can be applied to produce a new attribute (Figure 6.41). First attribute is produced using angle rotation of $\chi = 6$ (CI operator 1) and $\chi = 8$ (CI operator 2). The first attribute is aimed to enhance the identification of pore-fluid (Figure 6.42 and Figure 6.43). Examining the Lower Heimdal unit in the F-Well, the impedance value of oil-saturated sands is apparently lower than brine sands (Figure 6.42). Due to this reason, these attributes provide higher correlation with impedance log value (AI or AI-BL) compare to the correlation of AI with RAI (Figure 6.38 and Figure 6.39). However, the brine saturated sands of Lower Heimdal in the D-well is not characterized by the same feature (Figure 6.42). Adopting the F-Well features, the Lower Heimdal sandstones unit of the D-Well will be suspected as oil-saturated sands than brine-saturated sands since the Lower Heimdal unit in the D-Well is represented by low impedance profiles.

The second attribute is intended for lithology and pore-fluid identification, $\chi = -18$ for CI operator 1 and $\chi = -12$ for CI operator 2 (Figure 6.42 and Figure 6.43). In the F-Well, the oil sandstones are associated with stronger positive amplitude than the brine sandstones unit. The fluid contact can also be shown as the +/+ zero crossing, supporting that this angle is good in delineating pore-fluid. As a function of lithology, the sandstone is highlighted as positive amplitude. However, applying this feature to delineate the Lower Heimdal sandstones in the D-Well will cause misinterpretation. The low positive amplitude in Lower Heimdal sandstones that are suspected as brine saturated sands features in the D-Well is not constantly indicated for the whole Lower Heimdal unit. Using this attribute, the Lower Heimdal sandstones in the D-Well is presumed to be thinner than the actual.

In summary, interpretation using gradient impedance (GI) or EEI attribute ($\chi = -18$ for CI operator 1, and $\chi = -12$ for CI operator 2) alone is more robust than using relative impedance (RAI). The GIs or the EEIs are useful in interpreting the presence oil-saturated sandstones at the D-Well and the Nanna-Well (Figure 6.39, Figure 6.40, Figure 6.42 and Figure 6.43). The absence of oil-sandstones feature in the D-Well and the Nannna-Well, will lead to a conclusion of the non-existence of oil-sandstones on both wells.

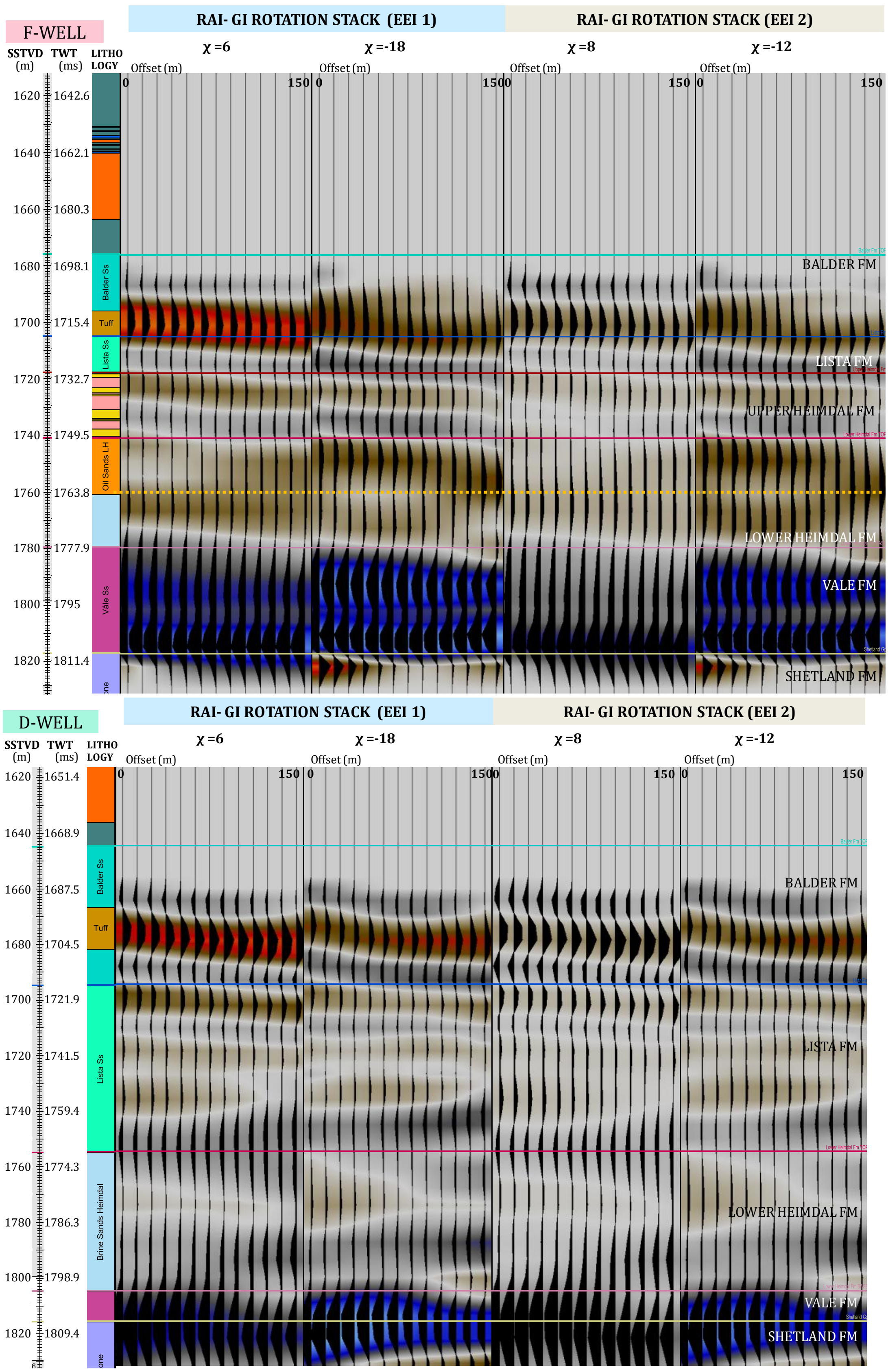

Figure 6.42 The derived EEI impedances for each CI operator for given chi angle (Figure 6.41) around the F-Well (top) and D-Well (bottom).

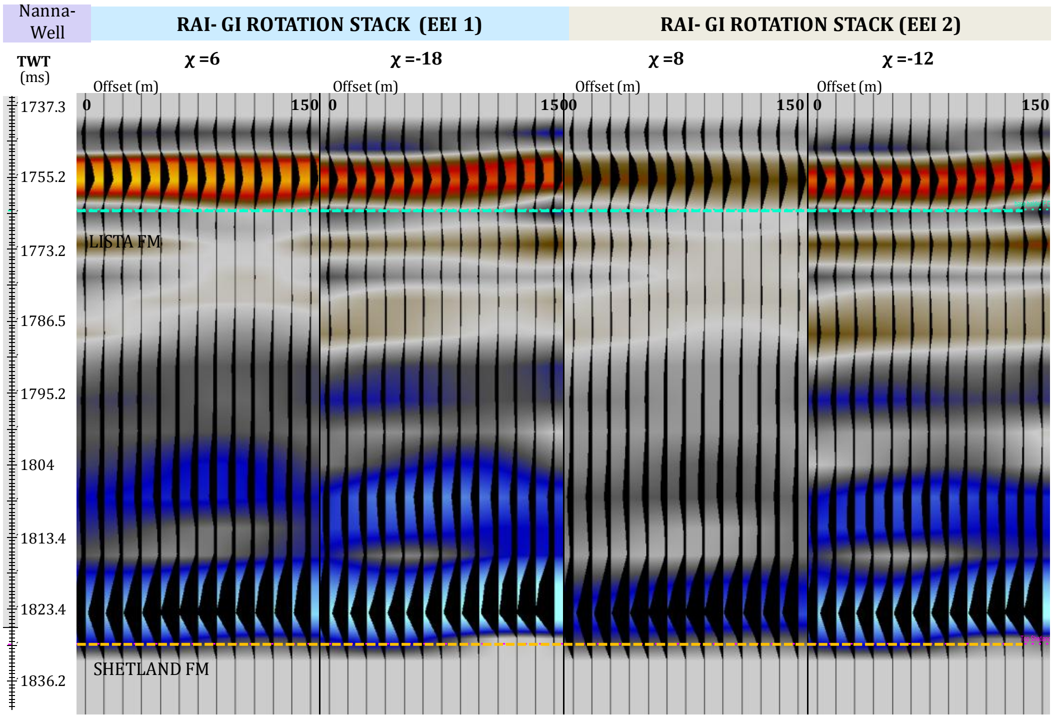

Figure 6.43 The derived EEI impedances for each CI operator for given chi angle (Figure 6.41) around the Nanna-Well.

Prediction of Lower Heimdal Oil-Sandstones

The distribution of Lower Heimdal oil-sandstones are predicted by using the information given by gradient impedance (GI) and EEI attribute of AI-GI at χ = -18 (CI first operator). The prediction of Lower Heimdal oil-sandstones is performed in each seismic profile based on the identified oil-sandstones signature that is observed around the F-Well area. In GI seismic profiles, the oil-sandstones character is given by strong negative signature with amplitude value of -8750000 to -4200000 (Figure 6.39). Meanwhile, in EEI attribute of AI-GI at χ = -18, the character is given by strong positive signature with amplitude value of 2000000 to 4500000 (Figure 6.42).

The resulting geobodies for each attribute may provide a new understanding in making further decision in terms of hydrocarbon exploration and development. The distribution of oil-sand units given by GI (Figure 6.44 and Figure 6.45) and EEI χ = -18 (Figure 6.46 and Figure 6.47) are predominantly identical in most places, except in south-east. In this area, the GI geobodies presents with a lower confidence level in finding oil-sands as there are no bodies observed in this area. It is therefore suggested to overlie the resulting geobodies of GI and EEI to increase the confidence in finding oil-sandstones. Moreover, choosing a target geobodies within the zones of Lower Heimdal highs may also reduce the degree of unsuccessful exploration (Figure 6.44 and Figure 6.46).

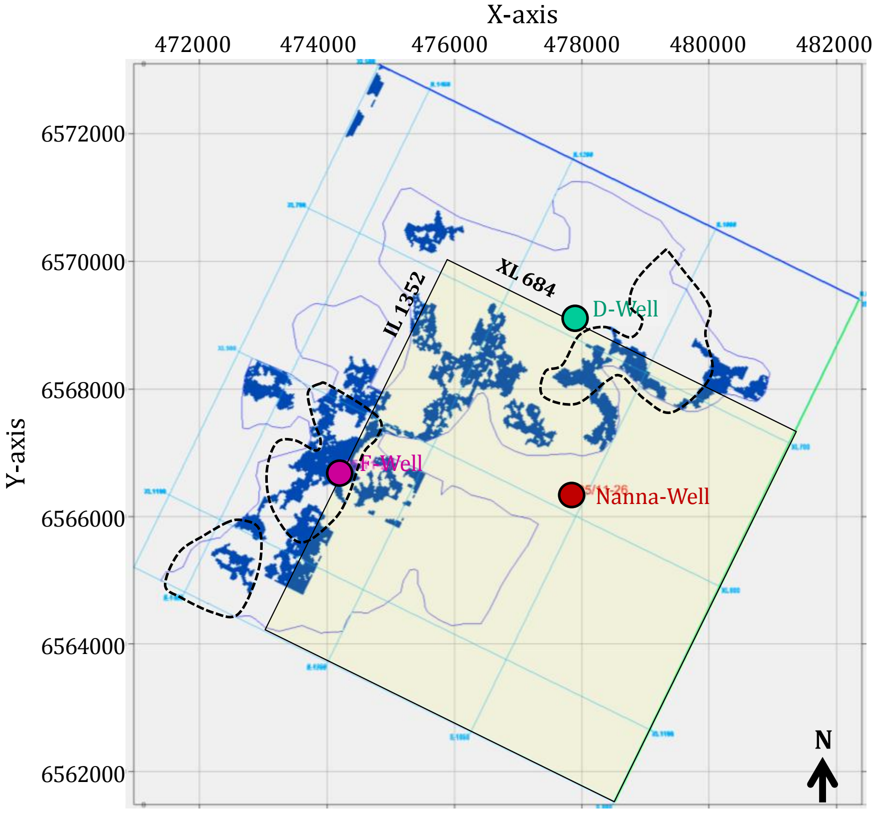

Figure 6.44 Distribution map of geobodies representing oil-sandstones of Lower Heimdal given by greadient impedance (GI). The black-dotted area represents structural highs in Lower Heimdal sands (Figure 6.28).

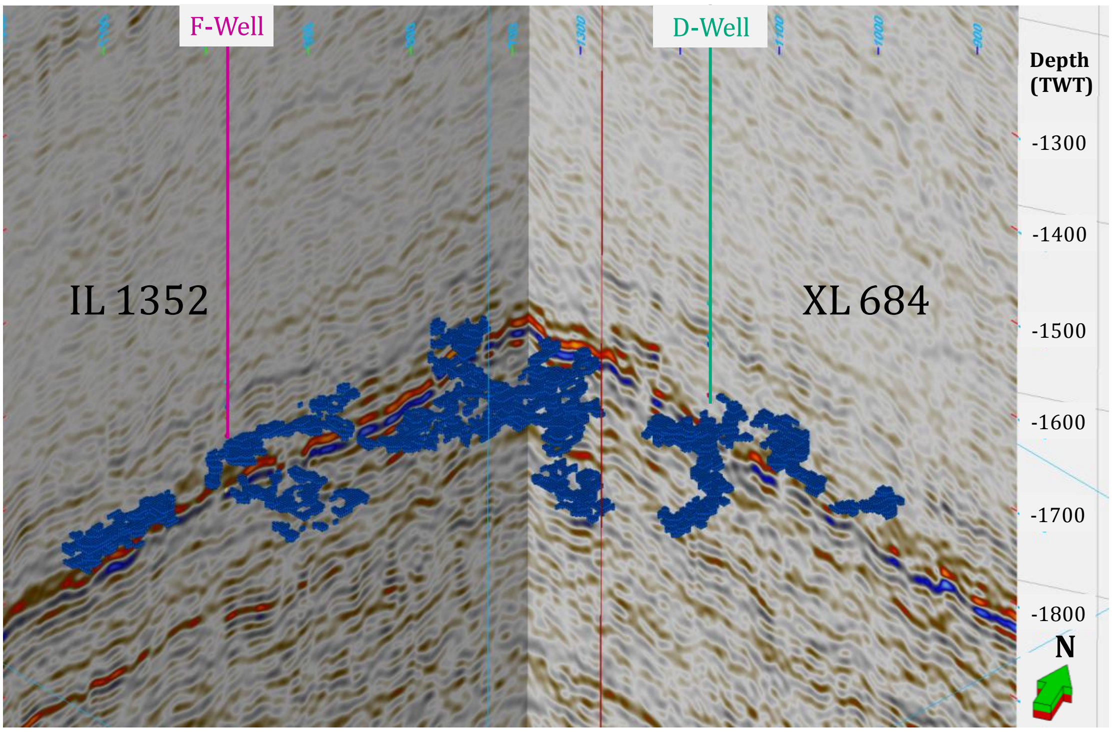

Figure 6.45 Geobodies representing oil-sandstones of Lower Heimdal given by greadient impedance (GI) within yellow area in Figure 6.44.

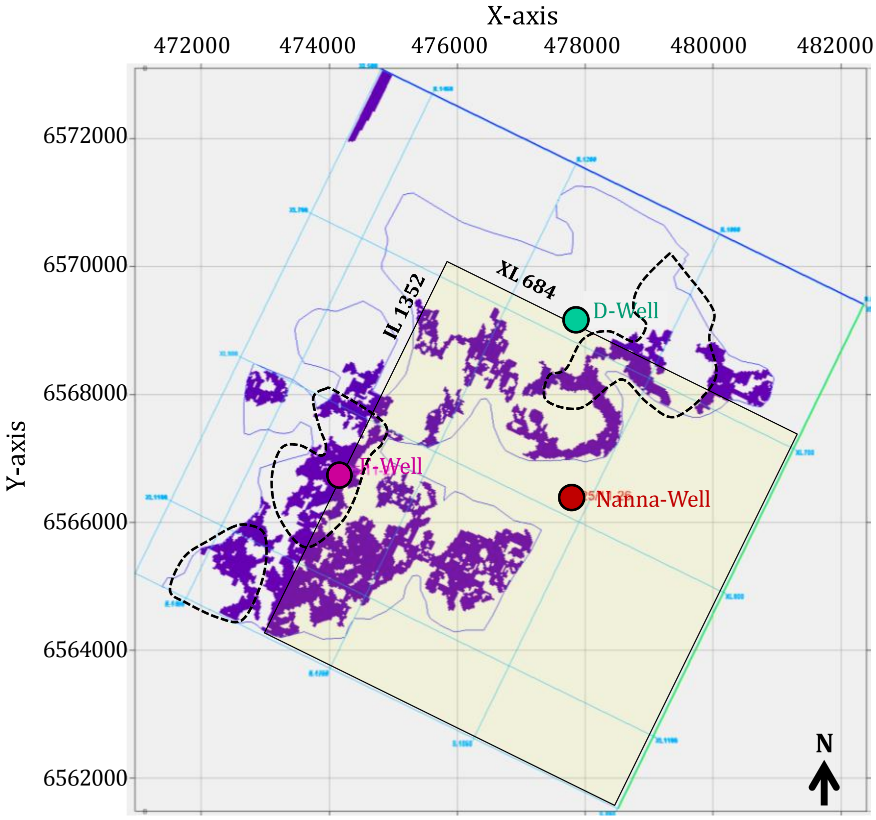

Figure 6.46 Distribution map of geobodies representing oil-sandstones of Lower Heimdal given by EEI attribute of AI-GI at $\chi = -18$. The black-dotted area represents structural highs in Lower Heimdal sands (Figure 6.28).

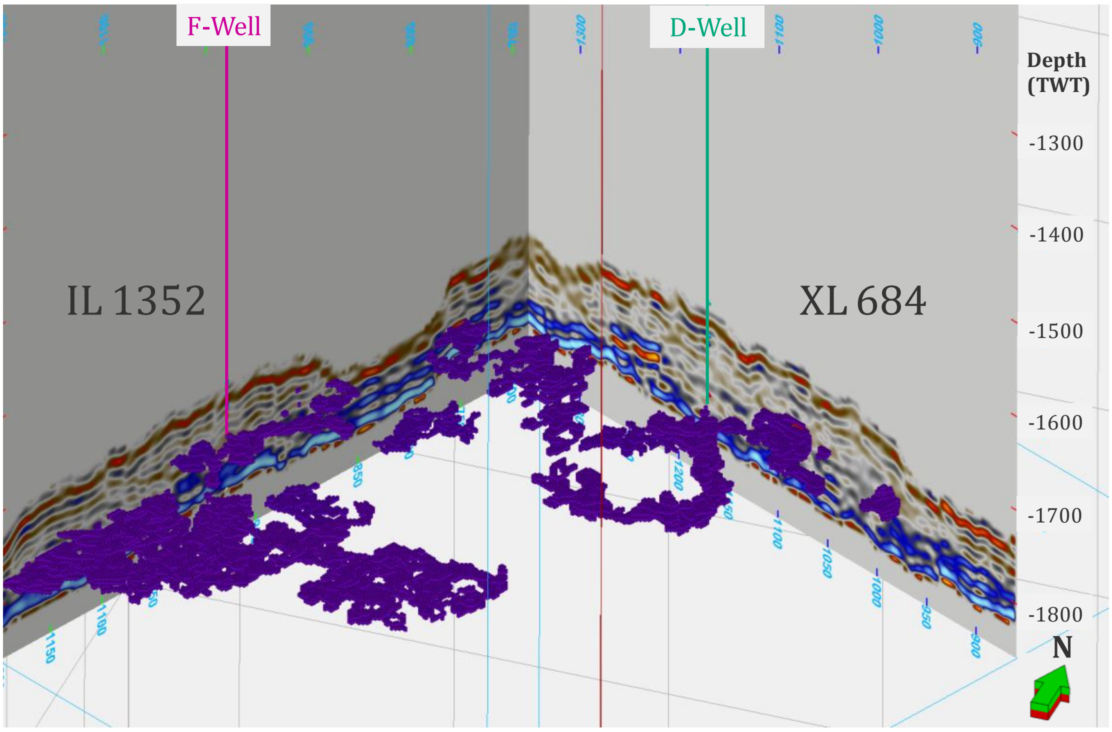

Figure 6.47 Geobodies representing oil-sandstones of Lower Heimdal given by EEI attribute of AI-GI at $\chi = -18$ within yellow area in Figure 6.46.

CHAPTER 7.

DISCUSSION SUMMARY

Chapter 4

Rock physics analysis, correlates the elastic parameter such as velocity, impedance, and velocity ratio, with geological and petrophysical parameters such as density, porosity, gamma-ray, mineralogical composition, depositional environment, post-depositional process, fluid properties, oil-saturation level, and temperature.

Main observations:

1. The onset of chemical compaction starts at depth 1640 mTVDSS for the F-well and 1620 mTVDSS for the D-well. For both wells, the onset lies on the shaly-sands interval of Hordaland formation, above the top seal unit of Lower Heimdal reservoir, or above the tuffaceous unit of base Balder Formation. The elastic parameters above the top seal are predominantly affected by the change of depositional environment rather than to post-depositional process ie., effect of increasing burial stress.
2. By correlation of temperature, velocity-ratio, impedance, and depth, the Lower Heimdal sandstones at the D-Well is known to be subsided deeper than the current position. This suggests the robustness of rock physics analysis as an aid to explain the post-depositional history of the rock during burial.
3. The physical properties of the parent reservoir rock, the Lower Heimdal sandstones, have a distinct character with the injectite sandstones, the Upper Heimdal sandstones. The unconsolidated sands model fits the Upper Heimdal, while cemented sands model fits the Lower Heimdal sandstones. RPT observation also shows that the degree of cementation of the Lower Heimdal sandstones is higher at the D-well than at the F-Well. The Lower Heimdal at the F-Well is properly modelled with 4% calcite cement, while D-well with 5% siliclastic cement. The higher cementation rate at the D-well is supported with the evidence that the Lower Heimdal sandstones at the D-Well had been subsided deeper than its current position.
4. As function of depth, the porosity of the Lower Heimdal sandstones at the F-Well is given as a constant fraction. This evidence suggests that the presence of oil may inhibit quartz cementation, thus preserving the porosity, and “removing” the effect of increasing cementation percentages as function of depth.
5. The absence of cementation in the injectite sands, the Upper Heimdal formation, suggests an assumption that the hydrocarbon was not available yet within the parent’s sands during the formation of injectite sands.

Chapter 5

Main observations from AVO modeling given by Gassmann- subtitution and Monte-Carlo simulation:

1. At near angle, or in the intercept, the reflection coefficient of top oil/brine-saturated sandstones of Lower Heimdal is characterized with positive amplitude, where the reflectivity of top brine-saturated sandstones provides higher value than oil-saturated sands.
2. The reflectivity of the top oil/brine-saturated sandstones decrease with the increasing angle of incidence. At maximum angle of 35 degrees, or within the far-angle, the reflectivity of top oil-saturated sandstones is lower than the brine-saturated sands.
3. The gradient of top oil-saturated sandstones is observed to be higher (in its absolute value) than the brine-saturated sandstones.
4. Feasibility analysis confirms that the far-angle reflection coefficients are more sensitive towards the pore-fluid changes compare to the near-angle reflectivity. Gradient also provides greater sensitivity than intercept in terms of pore-fluid identification.
5. The AVO classification of top oil/brine-saturated sandstones of the top Lower Heimdal formation is characterized as range of AVO Class I to Class IIp. The identification of pore-fluid is more effective by examining the distance of a point from zero point or origin.
6. Oil water contact or OWC interface between the oil and brine-saturated sandstones generates a positive reflectivity response from zero to maximum angle of 35 degree.

Main observations from fuzzy logic or multivariate statistical analysis:

1. The sensitivity level for each parameter towards lithology and pore-fluid variations can be measured by evaluating the fuzzy logic results with log-data distributions.
2. The P-wave velocity value are observed to be predominantly affected by the pore-fluid composition and the corresponding lithologies, while the S-wave value is predominantly affected by lithologies, ie. sand or shale.
3. The pore-fluid saturation prediction is best defined by assigning density to training data due to the lesser overlapping value between oil-saturated sands and brine-saturated sands in density data compare to velocity, gamma-ray, impedances and velocity-ratio.

Chapter 6

A. Pre-Inversion

1. Rock physics provide an important link from well-log information to the seismic signature. The diversify of Lower and Upper Heimdal sandstones microstructures, cause the Upper Heimdal to have a dimmer amplitude compare to Lower Heimdal sands. However other influences such as limited impedance contrast between laminated sands and shaly-sands may also cause the poor seismic character of the Upper Heimdal sandstones.
2. With higher cementation degree and higher brine saturation of Lower Heimdal sandstones at the D-Well, rock-physics and AVO analysis suggest that the reflectivity across the top of Lower Heimdal sandstones at the D-Well produces stronger or more positive seismic amplitude than the F-Well for all angle of incidence.
3. In the near angle seismic stack, the top of Lower Heimdal sandstones at the F-Well is observed with higher amplitude compare to the D-Well. The most possible explanation is due to the interference that occurs at the F-Well. The interference may demonstrate the superposition of the top of Lower Heimdal sandstones with the OWC reflector, or the superposition of the top of Upper Heimdal sandstones with the top of Lower Heimdal sandstones.
4. EEI petrophysical analysis suggests that at a certain angle chi (χ), the derived EEI log series gives maximum correlation with certain log sets. As the log set has different level of sensitivity towards lithology and pore-fluid, the derived EEI can also measure the sensitivity towards lithology and pore-fluid. Density, with dominant sensitivity towards pore-fluid has angle chi (χ) of 14. P-wave velocity, with dominant sensitivity of lithology and pore-fluid, has angle chi (χ) of -20. S-wave velocity with dominant sensitivity of lithology, has angle chi (χ) of -50. In this sense, chi (χ) around 14 will be regarded as pore-fluid projection angle, while chi (χ) around -20 to -50 will be regarded as lithology and pore-fluid projection angle.
5. To arrange interpretation strategy, the quality of each seismic cube needs to be well understood. The quality of interpretation for each seismic cube is examined based on the ability of each attribute to delineate the top of Lower Heimdal formation, to predict fluid and to estimate the Lower Heimdal sandstones thickness.
    5.1. Near angle stack, far angle stack, and its combination.

    The quality of near angle stack interpretation is fair, and care must be taken in this regard, ie. the seismic signature of Lower Heimdal sandstones also observed around the Nanna-Well that may cause false interpretation in 3D extent. In the case of far angle stack, the interpretation quality is also fair in estimating the top of Lower Heimdal (or even estimate the thickness) as the seismic signature across the top of Lower Heimdal is inconsistent for the F-Well and the D-Well. The far seismic provides more fluid sensitivity and coherence with the AVO model. In this context, the top of oil-saturated sandstones is represented by lower amplitude than the top of brine-saturated sandstones.

A combined interpretation of near and far angle stack gives improvement in the quality of interpretation, as it able to predict the top of Lower Heimdal sandstones and the pore-fluid.

5.2. Intercept, gradient, and its combination.

As the intercept is equal to the near stack, the interpretation of intercept is therefore considered to be fair. The gradient cube provides an excellent tool for interpretation of top and base Lower Heimdal sandstones. In the seismic profile, the top of Lower Heimdal is characterized by negative peak amplitude, while the bottom is characterized by strong positive amplitude. The value of reflectivity of top Lower Heimdal may also justify the pore-fluid content of sandstones. The higher negative value across the top sands corresponds to oil-saturated sands, while the lower negative corresponds to brine-saturated sands. Similar to the gradient interpretation, a combined interpretation of intercept and gradient is also excellent.

5.3. EEI reflectivity of χ = 10 and EEI reflectivity of χ =-23

The quality of EEI reflectivity of χ = 10 interpretation is very fair, due to the high noise level, and overlapping amplitude value between reservoir and the background. On contrary, the quality of EEI reflectivity of χ = -23 is excellent. The top of Lower Heimdal is identified as strong positive amplitude, while the base is identified as strong negative amplitude. The reflection intensity of the top Lower Heimdal may also help to identify the presence of hydrocarbons. The stronger amplitude value corresponds to the higher chance in finding oil-saturated sands than the brine-saturated sands.

5.4. AVO Class and AVO Strength

The quality of AVO Class interpretation is fair. The top of Heimdal sandstones are characterized as Class IIp. Even though it is valid to determine the top of Lower Heimdal for area around the well, the continuity in the sense of lateral extent is very limited, approximately 100 meters. The quality of AVO Strength is excellent to discriminate the pore-fluid. The oil-saturated sands are characterized with stronger amplitude than the brine-saturated sands. However, this attribute are not able to identify the top of Lower Heimdal.

6. Four seismic attributes are chosen to provide the structural map of top of Lower Heimdal sandstones – the near angle stack, far angle stacks, gradient, and EEI reflectivity of χ = -23. All interpretation profiles are showing three distinct structural highs – highs located in the south-west of the F-Well, highs around F-Well, and highs along the eastern to the southern side of D-Well. From all four interpretation profile, good coherency of structural relief is given by the interpretation of gradient and EEI reflectivity of χ = -23.
7. By assigning the value of seismic attributes that had been justified as good pore-fluid indicator, AVO strength, gradient, and EEI reflectivity of χ = -23 to the surface of top Lower Heimdal, may provide a robust tool to identify the hydrocarbon presences.

B. Inversion

From two inversion processes, the approximate thickness of the Lower Heimdal sandstones given by estimated impedances are only valid for the F-Well, not for the D-Well or the Nanna-Well. This supported by the correlation quality between the relative impedance results with band-limited impedance log that is verified with low value in the D-Well. Due to this reason, it is impossible to perform interpretation of the Lower Heimdal sandstones in 3D extent by using these relative impedance volumes. However, the gradient impedance and the EEI attribute at angle of lithology and pore-fluid projection, EEI of χ = -18, are able to establish the relationship to discriminate the oil-saturated sandstones from the background trend. The thickness of the oil-saturated sands of Lower Heimdal is successfully represented as geobodies.

CHAPTER 8.

CONCLUSIONS AND SUGGESTIONS

CONCLUSIONS

By selecting right strategies, interpretations performed on the datasets have been successfully established an improved structural mapping and an improved knowledge of distributions of Lower Heimdal oil-sandstones in the Grane area. The strategy involves the generation of varied seismic attributes, on which the level of sensitivity towards pore-fluid and lithology for each attributes are measured qualitatively. A cross-disciplinary analysis is developed to justify the impact of lithology, pore-fluid saturation level and petrophysical properties of the target interest in interpretation of seismic amplitudes.

In terms of rock physics, the diversify of Lower and Upper Heimdal sandstones microstructures is observed to cause the Upper Heimdal to have dimmer amplitude compare to Lower Heimdal. The rock physics analysis also provides an aid to explain the post-depositional history of rock during burial, such as the finding of the D-Well area that had been subsided deeper than its current position, and the finding of hydrocarbon migration that commenced after the injectite of the Upper Heimdal sands were established.

The quality of interpretation for the generated reflectivity attribute are examined based on the ability of each attribute to delineate the top of Lower Heimdal formation, to predict the fluid and to estimate the Lower Heimdal sandstone thickness. An approach is by examining the sensitivity of well-log parameters towards lithology and pore-fluid variation. Together with AVO modeling, these evaluations can be extended to evaluate the sensitivity of particular seismic attributes towards lithology and pore-fluid variations; and provide a competent foundation to understand the seismic signatures. After a thorough assessment, the gradient and the EEI reflectivity of χ=-23 are understood to be sensitive towards pore-fluid and lithology variation, while the AVO strength are very sensitive towards the pore-fluid variation. Based on this observation, reliable strategies for Lower Heimdal interpretation are established. The gradient and the EEI reflectivity seismic profiles provide a solid interpretation of top Lower Heimdal sandstones. Both attributes as well as AVO Strength are also effective to delineate the location of top oil-sandstones of Lower Heimdal.

As a unit thickness, the resulting impedance attributes, the gradient impedance and the EEI impedance attribute of of χ=-28, are successfully estimate the distribution of oil-sandstones bodies of Lower Heimdal in 3D-extent. The interpretation using the near angle-stack or also relative acoustic impedance must be taken with care as the evidence of interference that may occur across the top of Lower Heimdal sandstones in the near stack.

SUGGESTION

To create an optimal inversion result, it is suggested to add low frequency information within the inversion process or to perform an advance inversion methodology that incorporates more well control. The relative impedance does not provide information regarding trends – the trends by definition of low-frequency data. Moreover, as both inversion process presumed the seismic data to be zero-phase, the assymetric wavelet pulse may also cause the perturbation in the inversion process, and create false impedance response. Suggested procedures are to perform wavelet processing procedures to optimize the result from these type inversions, or taking another inversion methodology as an option since most of seismic data are known to be hardly zero-phase.

References

[1] Avseth, P. (2000). Combining rock physics and sedimentology for seismic reservoir characterization in North Sea turbidite systems: Ph.D. Thesis. Stanford University.

[2] Avseth, P. (2010). Explorational Rock Physics–The Link Between Geological Processes and Geophysical Observables. In Petroleum Geoscience (pp. 403-426). Springer Berlin Heidelberg.

[3] Avseth, P., Dræge, A., van Wijngaarden, A. J., Johansen, T. A., and Jørstad, A. (2008). Shale rock physics and implications for AVO analysis: A North Sea demonstration. The Leading Edge, 27(6), 788-797.

[4] Avseth, P., Dvorkin, J., Mavko, G., and Rykkje, J. (2000). Rock physics diagnostic of North Sea sands: Link between microstructure and seismic properties. Geophysical Research Letters, 27(17), 2761-2764.

[5] Avseth, P., Flesche, H., and Van Wijngaarden, A. J. (2003). AVO classification of lithology and pore fluids constrained by rock physics depth trends. The Leading Edge, 22(10), 1004-1011.

[6] Avseth, P., Mukerji, T., and Mavko, G. (2005). Quantitative seismic interpretation: Applying rock physics tools to reduce interpretation risk. Cambridge University Press.

[7] Avseth, P., Mukerji, T., Jørstad, A., Mavko, G., and Veggeland, T. (2001b). Seismic reservoir mapping from 3-D AVO in a North Sea turbidite system. Geophysics, 66(4), 1157-1176.

[8] Avseth, P., Mukerji, T., Mavko, G., and Tyssekvam, J. A. (2001a). Rock physics and AVO analysis for lithofacies and pore fluid prediction in a North Sea oil field. The Leading Edge, 20(4), 429-434.

[9] Bacon, M., Simm, R., and Redshaw, T. (2007). 3-D seismic interpretation. Cambridge University Press.

[10] Bjørlykke, K. (2010a). In K. Bjørlykke, eds., Petroleum Geoscience From Sedimentary Environments to Rock Physics: Shales, Silica Deposits and Evaporites. Springer-Verlag Berlin Heidelberg, 201-212.

[11] Bjørlykke, K. (2010b). In K. Bjørlykke, eds., Petroleum Geoscience From Sedimentary Environments to Rock Physics: Compaction of Sedimentary Rocks Including Shales, Sandstones and Carbonates. Springer-Verlag Berlin Heidelberg, 329-337.

[12] Bjørlykke, K., and Jahren, J. (2010). In K. Bjørlykke, eds., Petroleum Geoscience From Sedimentary Environments to Rock Physics: Sandstones and Sandstone Reservoirs. Springer-Verlag Berlin Heidelberg, 113-140.

[13] Bjørlykke, K., Høeg, K., and Mondol, N. H. (2010). In K. Bjørlykke, eds., Petroleum Geoscience From Sedimentary Environments to Rock Physics: Introduction to Geomechanics Stress and Strain in Sedimentary Basins. Springer-Verlag Berlin Heidelberg, 281-298.

[14] Bosch, D., Ledo, J., and Queralt, P. (2013). Fuzzy Logic Determination of Lithologies from Well Log Data: Application to the KTB Project Data set (Germany). Surveys in Geophysics, 34(4), 413-439.

[15] Briedis, N. A., Bergslien, D., Hjellbakk, A., Hill, R. E., and Moir, G. J. (2007). Recognition criteria, significance to field performance, and reservoir modeling of sand injections in the Balder field, North Sea, *in* A. Hurst and J. Cartwright, eds., Sand injectites: Implications for hydrocarborbon exploration and production. AAPG Memoir, 87(7), 91– 102.

[16] Brown, A. R.(2011). Interpretation of three-dimensional seismic data. American Association of Petroleum Geologists and the Society of Exploration Geophysicists.

[17] Buland, A. (2013). Sesimic amplitude analusis and inversion. Compendium GEO610.

[18] Castagna, J. P., and Swan, H. W. (1997). Principles of AVO crossplotting. The leading edge, 16(4), 337-344.

[19] Castagna, J. P., Swan, H. W., and Foster, D. J. (1998). Framework for AVO gradient and intercept interpretation. Geophysics, 63(3), 948-956.

[20] Connolly, P. (1999). Elastic impedance. The Leading Edge, 18(4), 438-452.

[21] Connolly, P., and London, B. P. (2010). Robust Workflows for Seismic Reservoir Characterisation. SEG Distinguished Lecture.

[22] Cuddy, S. J. (2000). Litho-facies and permeability prediction from electrical logs using fuzzy logic. SPE Reservoir Evaluation and Engineering, 3(04), 319-324.

[23] Dowey, P. (2012). Prediction of clay minerals and grain-coatings in sandstone reservoirs utilising ancient examples and modern analogue studies (Doctoral dissertation, University of Liverpool).

[24] Dræge, A. (2011). A diagenetic rock physics approach for siliciclastics. The Leading Edge, 30(12), 1368-1375.

[25] Dvorkin, J., and Nur, A. (1996). Elasticity of high-porosity sandstones: Theory for two North Sea data sets. Geophysics, 61(5), 1363-1370.

[26] Dvorkin, J., and Nur, A. (2002). In A. R. Huffman and G. L. Bowers, eds., Pressure regimes in sedimentary basins and their prediction: Critical-Porosity Models. AAPG Memoir 76, 33–41.

[27] Gassmann, F. (1951). Elasticity of porous media. Vierteljahrsschrder Naturforschenden Gesselschaft, 96, 1-23.

[28] Gidlow, P. M., and Smith, G. C. (2003, June). The fluid factor angle. In 65th EAGE Conference and Exhibition.

[29] Hamberg, L., Jepsen, A. M., Ter Borch, N., Dam, G., Engkilde, M. K., and Svendsen, J. B. (2007). Mounded structures of injected sandstones in deep-marine Paleocene reservoirs, Cecilie field, Denmark, in A. Hurst and J. Cartwright, eds., Sand injectites: Implications for hydrocarbon exploration and production: AAPG Memoir 87(5), 69– 79.

[30] Han, D. H., Nur, A., and Morgan, D. (1986). Effects of porosity and clay content on wave velocities in sandstones. Geophysics, 51(11), 2093-2107.

[31] Heslop, K., and Heslop, A. (2003). Interpretation of Shaly Sands. London Petrophysical Society. http://www.lps.org.uk/docs/heslop_shaly_sands.pdf

[32] Humphreys, B., Smith, S. A., and Strong, G. E. (1989). Authigenic chlorite in Late Triassic sandstones from the central graben, North Sea. Clay mineral, 24, 427-444.

[33] Huuse, M., Duranti, D., Steinsland, N., Guargena, C. G., Prat, P., Holm, K., and Hurst, A. (2004). Seismic characteristics of large-scale sandstone intrusions in the Paleogene of the south Viking Graben, UK and Norwegian North Sea. Geological Society, London, Memoirs, 29(1), 263-278.

[34] Isaksen, G. H., and Ledje, K. H. I. (2001). Source rock quality and hydrocarbon migration pathways within the greater Utsira High area, Viking Graben, Norwegian North Sea. AAPG bulletin, 85(5), 0861-0884.

[35] Iske, A., and Randen, T. (2005). Methods and Modelling in Hydrocarbon Exploration and Production.

[36] Japsen, P., Mukerji, T., and Mavko, G. (2007). Constraints on velocity-depth trends from rock physics models. Geophysical Prospecting, 55(2), 135-154.

[37] Ji , Y. L.(2013). The Research of Controlling factors of Reservoir Petrophysical Property of the First member of Funing Formation of Paleagene in Gaoyou Sag [Abstract]. In 30th IAS Meeting of Sedimentology Scientific Programme.

[38] Jonk, R., Hurst, A., Duranti, D., Parnell, J., Mazzini, A., and Fallick, A. E. (2005). Origin and timing of sand injection, petroleum migration, and diagenesis in Tertiary reservoirs, south Viking Graben, North Sea. AAPG bulletin, 89(3), 329-357.

[39] Justwan, H., and Dahl, B. (2005, January). Quantitative hydrocarbon potential mapping and organofacies study in the Greater Balder Area, Norwegian North Sea. In Geological Society, London, Petroleum Geology Conference series (Vol. 6, pp. 1317-1329). Geological Society of London.

[40] Justwan, H., Meisingset, I., Dahl, B., and Isaksen, G. H. (2006). Geothermal history and petroleum generation in the Norwegian South Viking Graben revealed by pseudo-3D basin modelling. Marine and Petroleum Geology, 23(8), 791-819.

[41] Kemper, M., and Huntbatch, N. (2012). From Inversion Results to Reservoir Properties. Search and Discovery Article.

[42] Kemper, M., Efthymiou, E., Morris, H., and Kerr, J. D. (2010, June). Seismic Data Conditioning of Partial Stacks for AVO–Using Well Offset Amplitude Balancing. In 72nd EAGE Conference and Exhibition.

[43] Kneller, B. C., Martinsen, O. J., and McCaffrey, B. (Eds.). (2009). External controls on deep-water depositional systems (Vol. 92). SEPM Soc for Sed Geology.

[44] Lancaster, S., and Whitcombe, D. (2000). Fast-track ‘coloured’inversion. Paper presented at the SEG Expanded Abstracts.

[45] Latimer, R. B., Davidson, R., and Van Riel, P. (2000). An interpreter's guide to understanding and working with seismic-derived acoustic impedance data. The Leading Edge, 19(3), 242-256.

[46] Mahob, P. N., and Castagna, J. P. (2003). AVO polarization and hodograms: AVO strength and polarization product. Geophysics, 68(3), 849-862.

[47] Mangerud, G., Dreyer, T., Søyseth, L., Martinsen, O., and Ryseth, A. (1999). High-resolution biostratigraphy and sequence development of the Palaeocene succession, Grane Field, Norway. Geological Society, London, Special Publications, 152(1), 167-184.

[48] Marion, D. (1990). Acoustical, Mechanical and Transport Properties of Sediments and Granular Materials: Ph.D. Thesis. Stanford University.

[49] Martinsen, O. J., Lien, T., and Jackson, C. (2005, January). Cretaceous and Palaeogene turbidite systems in the North Sea and Norwegian Sea Basins: source, staging area and basin physiography controls on reservoir development. In Geological Society, London, Petroleum Geology Conference series (Vol. 6, pp. 1147-1164). Geological Society of London.

[50] Maynard, K., Allo, P., and Houghton, P. (2003). Coloured Seismic Inversion, a Simple, Fast and Cost Effective Way of Inverting Seismic Data: Examples from Clastic and Carbonate Reservoirs, Indonesia. In 29th IPA Annual Convention Proceedings.

[51] Moraes, M. A., and De Ros, L. F. (1990). Infiltrated clays in fluvial Jurassic sandstones of Recôncavo Basin, northeastern Brazil. Journal of Sedimentary Research, 60(6).

[52] Mørk, M. B. E., and Moen, K. (2007). Compaction microstructures in quartz grains and quartz cement in deeply buried reservoir sandstones using combined petrography and EBSD analysis. Journal of Structural Geology, 29(11), 1843-1854.

[53] Net, L.I., Ochoa, M., McDougall, N.D., and Pestman, P. (2013). Linking diagenesis to sequence stratigraphy to assess reservoir quality: the example of the Snadd Formation (Triassic), Barents Sea, Norway Sag [Abstract]. In 30th IAS Meeting of Sedimentology Scientific Programme.

[54] Nilsen, T. H., Shew, R. D., Steffens, G. S., and Studlick, J. (Eds.). (2008). Atlas of Deep-Water Outcrops: AAPG Studies in Geology 56 (Vol. 56). AAPG.

[55] Nur, A., Mavko, G., Dvorkin, J., and Galmudi, D. (1998). Critical porosity: A key to relating physical properties to porosity in rocks. The Leading Edge, 17(3), 357-362.

[56] Ødegaard, E. R. I. K., and Avseth, P. (2003, June). Interpretation of elastic inversion results using rock physics templates. In 65th EAGE Conference and Exhibition.

[57] Ostrander, W. (1984). Plane-wave reflection coefficients for gas sands at nonnormal angles of incidence. Geophysics, 49(10), 1637-1648.

[58] Pedersen, J. H., Karlsen, D. A., Backer-Owe, K., Lie, J. E., and Brunstad, H. (2006). The geochemistry of two unusual oils from the Norwegian North Sea:

Implications for new source rock and play scenario. Petroleum Geoscience, 12(1), 85-96.

[59] Rezaei, M., and Movahed, B. (2009). New Approach of Fuzzy Logic Applied to Lithofacies Forecasting and Permeability Values Estimation. Journal of Applied Sciences, 9(12).

[60] Roy, S. S., Bøen, F., Sæbø, A., and Aanonsen, S. I. (2011, May). 4D Seismic Monitoring-A Case Study on the Grane Field, North Sea. In 73rd EAGE Conference and Exhibition.

[61] Rutherford, S. R., and Williams, R. H. (1989). Amplitude-versus-offset variations in gas sands. Geophysics, 54(6), 680-688.

[62] Ruud, B. O., Jakobsen, M., and Johansen, T. A. (2003, January). Seismic properties of shales during compaction. In 2003 SEG Annual Meeting. Society of Exploration Geophysicists.

[63] Schwab, A. M., Jameson, E. W., and Townsley, A. (2014). Volund Field: development of an Eocene sandstone injection complex, offshore Norway. Geological Society, London, Special Publications, 403, SP403-4.

[64] Statoil. (1993, February). Final Well Report: Well 25/8-4.

[65] Statoil. (2013, December). Final Well Report: Grane F-Structure Well 25/11-27.

[66] Van Breemen, N. (1980). Magnesium-ferric iron replacement in smectite during aeration of pyritic sediments. Clay mineral, 15, 101-110.

[67] Velzeboer, C. J. (1981). The theoretical seismic reflection response of sedimentary sequences. Geophysics, 46(6), 843-853.

[68] Walden, A., and Hosken, J. (1985). An investigation of the spectral properties of primary reflection coefficients. Geophysical Prospecting, 33(3), 400-435.

[69] Waters, K.H. (1978). Reflection Seismology. John Wiley, New York.

[70] Whitcombe, D. N., Connolly, P. A., Reagan, R. L., and Redshaw, T. C. (2002). Extended elastic impedance for fluid and lithology prediction. Geophysics, 67(1), 63-67.

[71] Whitcombe, D. N., Dyce, M., McKenzie, C. J. S., and Hoeber, H. (2004, January). Stabilizing the AVO gradient. In 2004 SEG Annual Meeting. Society of Exploration Geophysicists.

[72] Wild, J., and Briedis, N. (2010). Structural and stratigraphic relationships of the Palaeocene mounds of the Utsira High. Basin Research, 22(4), 533-547.

[73] Wittick, T. (1992). An Overview of Reservoir Seismic Stratigraphy. North Texas Geological Society

[74] Yin, H. (1992). Acoustic velocity and attenuation of rocks: Isotropy, intrinsic anisotropy, and stress-induced anisotropy: Ph.D. Thesis. Stanford University.